

Gravitational Collapse in Anti-de Sitter Spacetime

by
Bradley Stuart Cownden

A Thesis submitted to the Faculty of Graduate Studies of
The University of Manitoba
in partial fulfillment of the requirements for the degree of

DOCTOR OF PHILOSOPHY

Department of Physics and Astronomy
University of Manitoba
Winnipeg

© 2019 by Bradley Stuart Cownden

Dedication.

Acknowledgments

Abstract

An abstract.

Contents

Acknowledgments	i
Abstract	ii
Table of Contents	iii
1 Introduction	1
2 Nonlinear Evolution of Massive Scalar Fields in Anti-de Sitter Spacetime	2
2.1 Contributions	2
2.2 Introduction	3
2.3 Review	5
2.3.1 Massive scalars, stability, and time scales	5
2.3.2 Methods	8
2.4 Phase Diagram of Stability	9
2.4.1 Metastable versus unstable initial data	10
2.4.2 Irregular behaviors	13
2.5 Spectral analysis	18
2.5.1 Dependence on mass	19
2.5.2 Spectra of different behaviors	20
2.5.3 Evolution of spectra	21
2.6 Discussion	23
2.A Convergence Testing	25
3 Perturbative Stability of Massless Scalars in AdS₄	30
3.1 Contributions	30
3.2 Introduction	31
3.3 Minimally Coupled Scalar Fields in AdS _{d+1}	33
3.3.1 Linearized Solutions	33
3.3.2 Two-Time Formalism	34
3.4 Quasi-periodic Solutions in AdS ₄	35
3.4.1 Persistence at Large j_{max}	36
3.4.2 High Temperature Perturbations	37
3.4.3 Building High-Temperature Solutions	38
3.4.4 Stability of QP Solutions	39
3.5 Time Evolution of Quasi-Periodic Solutions	40
3.5.1 Quasi-Periodic Solutions	41

3.5.2	High-Temperature Solutions	43
3.6	Discussion	46
3.A	Seeding Methods For Non-Linear Solvers	56
3.B	Auxiliary Integrals For Calculating the T, R, S Coefficients	56
3.C	Frequency of Solution Checking	58
4	Perturbative Descriptions of Driven Instabilities in AdS	61
4.1	Contributions	61
4.2	Introduction	62
4.3	Source Terms and Boundary Conditions	63
4.4	Resonances From Normalizable Solutions	67
4.4.1	Naturally Vanishing Resonances: $(+++)$ and $(+--)$	68
4.4.2	Non-vanishing Resonance: $(++-)$	69
4.5	Resonances From Non-normalizable Modes	70
4.5.1	Two Non-normalizable Modes with Equal Frequencies	71
4.5.2	Special Values of Non-normalizable Frequencies	72
4.5.3	Integer Plus χ	79
4.6	Discussion	82
4.A	Derivation of Source Terms For Massive Scalars	83
4.B	Two Non-normalizable Modes with Equal Frequencies	86
5	Conclusion	88
Bibliography		93

List of Figures

2.1	Horizon formation time vs. amplitude for classes of initial data	6
2.2	Stability phase diagram	9
2.3	Fitting the leading coefficient of $t_H = a\epsilon^{-p} + b$ as a function of initial data width	11
2.4	Horizon formation times for metastable initial data	12
2.5	Horizon formation times for irregular initial data	14
2.6	Evidence for chaotic evolution	16
2.7	Phase space trajectories for irregular and unstable initial data	17
2.8	Mass density profiles for chaotic systems	18
2.9	Energy spectra of best fit gaussians to the $j = 0$ eigenmode for various masses	19
2.10	Initial energy spectra for each type of initial data	20
2.11	Evolution of the energy spectra	22
2.12	Late-time spectra	23
2.A.1	Comparison of order of convergence of ϕ, M, A, δ as a function of time for $\mu = 0.5$ over two base resolutions	25
2.A.2	Order of convergence for ϕ, M, A, δ as a function of time for $\mu = 15$ at nearby amplitudes	26
2.A.3	Order of convergence for ϕ, M, A, δ as a function of time for $\mu = 0$ at nearby amplitudes	26
2.A.4	Order of convergence for ϕ, M, A, δ as a function of time for $\mu = 5$ at nearby amplitudes	27
2.A.5	Order of convergence for ϕ, M, A, δ as a function of time for $\mu = 1$ at nearby amplitudes	27
2.A.6	Order of convergence for ϕ, M, A, δ as a function of time for $\mu = 20$ at nearby amplitudes	28
3.1	Energy spectra for various QP solutions	36
3.2	High temperature solutions resulting from projecting back to the QP solution plane at various frequencies	38
3.3	Energy spectra resulting from perturbing the same QP solution at differing frequencies	40
3.4	Constructing high temperature solutions by hand	41
3.5	Upper envelope of Π^2 at the origin for selected low- and high-temperature QP solutions	42
3.6	Absolute and relative residuals for low- and high-temperature QP solutions	43
3.7	Evolution of QP solutions at low temperature for different truncation values	44
3.8	Residual and spectrum of a low-temperature QP solution during evolution	44

3.9	Taking the spectrum of a QP solution during evolution to use as a seed to find new QP solutions	45
3.10	The evolution of a padded QP solution	47
3.11	Spectra during evolution of a padded QP solution are used as seeds to project back to the QP plane	48
3.12	Examining the energy per mode during the evolution of a threshold temperature solution	49
3.13	Evolution of the energy spectrum for a high-temperature solution created by hand	49
3.14	Evolution of the spectrum, absolute and relative residual, and Ricci scalar for a high-temperature solution that has been padded with 25 extra modes	50
3.15	Evolution of the spectrum of a high-temperature solution padded with 100 modes	50
3.16	Evolution of the spectrum of a high-temperature solution padded with 25 modes .	51
3.17	Evolution of a high-temperature state that does not satisfy the QP equation . . .	52
3.18	Evolution of the spectrum of a threshold temperature solution that has been padded with 100 modes	53
3.19	Padded threshold temperature solutions cannot be projected back to the QP solution plane	54
3.20	Comparison between a threshold temperature solution with $j_{max} = 200$ and the evolution of a $j_{max} = 100$ threshold temperature solution that has been padded by 100 modes	55
3.A.1	Comparison of seed values to known QP solutions and exponential fitting	58
3.A.2	Illustrating the tail fitting procedure	59
3.C.1	Comparison of spectra and temperatures for different projection frequencies between $j_{max} = 50$ and $j_{max} = 150$ solutions	60
4.1	Evaluating non-vanishing resonances for normalizable modes over a range of m^2 values	70
4.2	Source term for two equal frequency, non-normalizable modes when $m^2 = 0$	73
4.3	Source term for two equal frequency, non-normalizable modes when $m^2 = -1$. . .	74
4.4	Source term for two non-normalizable modes whose frequencies add to an integer when $m^2 = -1$ and $\bar{\omega}_1 + \bar{\omega}_2 = 4$	77
4.5	Source term for two non-normalizable modes whose frequencies add to an integer when $m^2 = 0$ for $\bar{\omega}_1 + \bar{\omega}_2 = 4$ and 8	78
4.6	Source term for two non-normalizable modes with frequencies $\omega_\alpha = 2\alpha + \chi$ over various choices of χ	81

List of Tables

2.1	Best fit parameters for metastable data	13
2.2	Best fit Lyapunov coefficients	16
3.1	Threshold temperatures for different series truncations with constant projection frequency	39
3.A.1	Convergence of the real coefficient α_j of the $j = 50$ mode with increasing j_{max} . . .	57

1 Introduction

The introduction.

2 Nonlinear Evolution of Massive Scalar Fields in Anti-de Sitter Spacetime

Published to the arXiv, submitted to Phys Rev Lett B.

2.1 Contributions

What my contributions were.

Phase Diagram of Stability for Massive Scalars in Anti-de Sitter Spacetime

[arXiv:1711.00454](https://arxiv.org/abs/1711.00454)

Brad Cownden¹, Nils Deppe², and Andrew R. Frey^{3,4}

¹*Department of Physics & Astronomy,
University of Manitoba
Winnipeg, Manitoba R3T 2N2, Canada
cowndenb@myumanitoba.ca*

²*Cornell Center for Astrophysics and Planetary Science and Department of Physics,
Cornell University
122 Sciences Drive, Ithaca, New York 14853, USA
nd357@cornell.edu*

³*Department of Physics & Astronomy,
University of Manitoba
Winnipeg, Manitoba R3T 2N2, Canada*

⁴*Department of Physics and Winnipeg Institute for Theoretical Physics,
University of Winnipeg
515 Portage Avenue, Winnipeg, Manitoba R3B 2E9, Canada
a.frey@uwinnipeg*

We diagram the behavior of 5-dimensional anti-de Sitter spacetime against horizon formation in the gravitational collapse of a scalar field, treating the scalar field mass and width of initial data as free parameters, which we call the stability phase diagram. We find that the class of stable initial data becomes larger and shifts to smaller widths as the field mass increases. In addition to classifying initial data as stable or unstable, we identify two other classes based on nonperturbative behavior. The class of metastable initial data forms a horizon over longer time scales than suggested by the lowest order perturbation theory at computationally accessible amplitudes, and irregular initial data can exhibit non-monotonic and possibly chaotic behavior in the horizon formation times. Our results include evidence for chaotic behavior even in the collapse of a massless scalar field.

2.2 Introduction

Through the anti-de Sitter spacetime (AdS)/conformal field theory (CFT) correspondence, string theory on $\text{AdS}_5 \times X^5$ is dual to a large N conformal field theory in four spacetime dimensions ($\mathbb{R} \times S^3$ when considering global AdS_5). The simplest time-dependent system to study in this context is the gravitational dynamics of a real scalar field with spherical symmetry, corresponding to the time dependence of the expectation value of the zero mode of a single trace operator in the gauge theory. Starting with the pioneering work of [1–4], numerical studies have suggested that these dynamics may in fact be generically unstable toward formation of (asymptotically) AdS_{d+1}

black holes even for arbitrarily small amplitudes. While perhaps surprising compared to intuition from gravitational collapse in asymptotically flat spacetimes, the dual picture of thermalization of small energies in a compact space is more expected. In terms of the scalar eigenmodes on a fixed AdS background, the instability is a cascade of energy to higher frequency modes and shorter length scales (weak turbulence), which eventually concentrates energy within its Schwarzschild radius. In a naive perturbation theory, this is evident through secular growth terms.

However, some initial scalar field profiles lead to quasi-periodic evolution (at least on the time scales accessible via numerical studies) at small but finite amplitudes; even early work [1, 5] noted that it is possible to remove the secular growth terms in the evolution of a single perturbative eigenmode. A more sophisticated perturbation theory [6–17] supports a broader class of quasi-periodic solutions that can contain non-negligible contributions from many modes, and other stable solutions orbit the basic quasi-periodic solutions [14]. Stable solutions exhibit inverse cascades of energy from higher frequency to lower frequency modes due to conservation laws following from the high symmetry of AdS (integrability of the dual CFT). Stable behavior also appears in the full non-perturbative dynamics for initial profiles with widths near the AdS length scale [18–20]; however, analyses of the perturbative and full dynamics in the literature have not always been in agreement at fixed small amplitudes. For example, some perturbatively stable evolutions at finite amplitude actually form black holes in numerical evaluation of the full dynamics [6, 21, 22]. Understanding the breakdown of the approximations used in the perturbative theory, as well as its region of validity, is an active and important area of research [23–27].

Ultimately, the main goal of this line of inquiry is to determine whether stability or instability to black hole formation (or both) is generic on the space of initial data, so the extent of the “islands of stability” around single-mode or other quasi-periodic solutions and how it varies with parameters of the physics on AdS are key questions of interest. The biggest changes occur in theories with a mass gap in the black hole spectrum, such as AdS₃ and Einstein-Gauss-Bonnet gravity in AdS₅, which cannot form horizons at small amplitudes. While small-amplitude evolution in AdS₃ appears to be quasi-periodic [28, 29], there is some evidence to point toward late-time formation of a naked singularity in AdS₅ Einstein-Gauss-Bonnet gravity [30, 31] (along with a power law energy spectrum similar to that at horizon formation). Charged scalar and gauge field matter [32] also introduces a qualitative change in that initial data may lead to stable evolution or instability toward either Reissner-Nordström black holes or black holes with scalar hair.

In this paper, we extend the study of massive scalar matter initiated in [33, 34]. Specifically, using numerical evolution of the full gravitational dynamics, we diagram classes of gravitational collapse behavior as a function of scalar field mass and initial scalar profile width, which we call a stability phase diagram in analogy to a phase diagram for phases of matter. This is the first systematic study of behavior for classes of initial data in AdS gravitational collapse using two tuning parameters. By considering the time to horizon formation as a function of the initial profile’s amplitude at finite amplitude, we identify several different classes of behavior and indicate them on the phase diagram. Finally, we analyze and characterize these different behaviors, presenting evidence for chaotic behavior, including the first evidence for chaotic behavior in the horizon formation time of massless scalar collapse, which has no length scale other than the AdS radius. Throughout, we work in AdS₅, due to its relevance to strongly coupled gauge theories in four dimensions and because previous literature has indicated massless scalars lead to greater instability than in AdS₄ (the main other case considered), which makes the effects of the scalar field mass more visible.

We note briefly two caveats for the reader. First, horizon formation always takes an infinite amount of time on the AdS conformal boundary due to the usual time dilation effects associated with horizons; this agrees with the understanding of thermalization in the CFT as an asymptotic process. Horizon formation times discussed in this paper correspond to an approximate notion of horizon formation that we will describe below, but alternate measures of thermalization may be of interest. Second, the black holes we discuss are smeared on the compact X^5 dimensions of the gravitational side of the duality, as in most of the literature concerning stability of AdS, and we are particularly interested in small initial amplitudes that lead to black holes small compared to the AdS scale. As described in [35–37], small black holes in this situation suffer a Gregory-Laflamme-like instability toward localization on X^5 (which may in fact lead to formation of a naked singularity). At the same time, certain light stable solutions for charged scalars (boson stars) are stable against localization on X^5 [38]. We therefore provisionally assume that the onset of the Gregory-Laflamme-like instability occurs only at horizon formation, not at any point of the earlier horizon-free evolution.

The plan of this paper is as follows: in section 2.3, we review the time scales associated with horizon formation with an emphasis on the behavior of massive scalars and briefly discuss our methods. Then, in section 2.4, we present the phase diagram of different stability behaviors, and an attempt at heuristic analytic understanding appears in 2.5. We close with a discussion of our results.

2.3 Review

In this section, we review results on the stability of scalar field initial data as well as our methods (following the discussion of [34]).

2.3.1 Massive scalars, stability, and time scales

As in most of the literature, we work in Schwarzschild-like coordinates, which have the line element (in asymptotic AdS_{d+1})

$$ds^2 = \frac{1}{\cos^2(x)} (-Ae^{-2\delta}dt^2 + A^{-1}dx^2 + \sin^2(x)d\Omega^{d-1}) \quad (2.1)$$

in units of the AdS scale. In these coordinates, a horizon appears at $A(x, t) = 0$, but reaching zero takes an infinite amount of time (measured either in proper time at the origin or in conformal boundary time); following the standard approach, we define a horizon as having formed at the earliest spacetime point (as measured by t) where A drops below a specified threshold defined in §2.3.2 below. Of course, horizon formation represents a coarse-grained description since the pure initial state of the dual CFT cannot actually thermalize; a more precise indicator of approximate thermalization may be the appearance of a power law energy spectrum (exponentially cut off) in the perturbative scalar eigenmodes. This indicator is tightly associated with horizon formation (though see [30, 31] for some counterexamples).

A key feature of any perturbative formulation of the gravitational collapse is that deviations from $A = 1, \delta = 0$ appear at order ϵ^2 , where ϵ is the amplitude of initial data. As a result, horizons can form only after a time $t \sim \epsilon^{-2}$; in the multiscale perturbation theory of [6, 7, 9–11, 13–17], there is

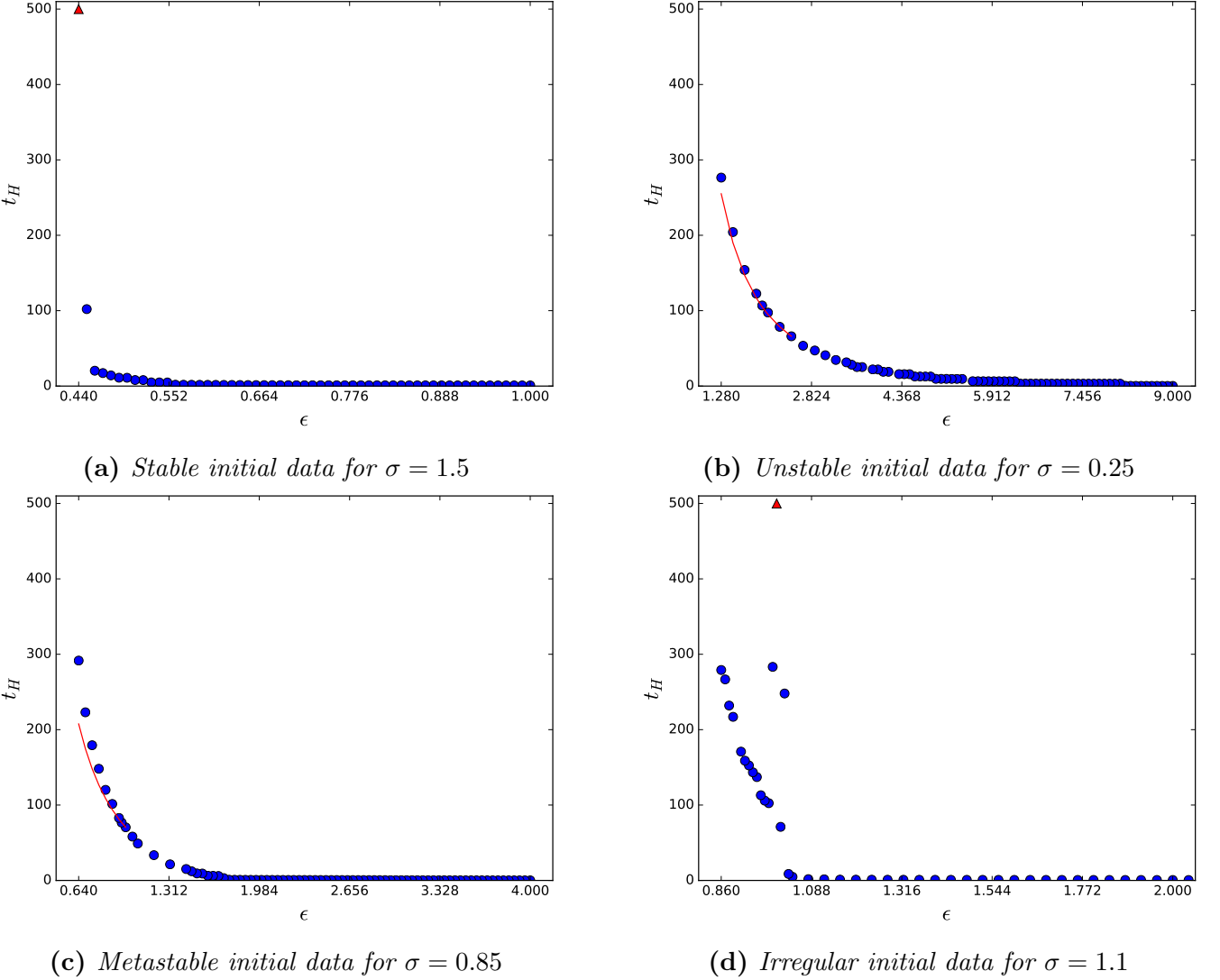


Figure 2.1: Classes of initial data for massless scalars and initial width σ . Blue dots represent horizon formation; red triangles indicate a lower limit for t_H . Red curves in subfigures 2.1b, 2.1c are $t_H = a\epsilon^{-2} + b$ matched to largest two amplitudes in the curve.

in fact a scaling symmetry $\epsilon \rightarrow \epsilon', t \rightarrow t(\epsilon/\epsilon')^2$ that enforces the proportionality $t_H \propto \epsilon^{-2}$, where t_H is the (approximate) horizon formation time for unstable initial data at small amplitude.

At this point, it is worth making a small clarification. If the collapsing matter takes the form of a well-defined pulse, horizon formation occurs when the pulse nears the origin. For massless matter, that means that the t_H is piecewise continuous as a function of ϵ ; each continuous “step” has approximately constant t_H and is separated from the next step by a time of approximately π , the light crossing time for a round trip from the origin to the boundary of AdS. Massive matter does not reach the boundary, so the steps are not always separated by π , and may in fact not be separated at all if the pulse spreads out in radius. In any case, though, the width of the steps decreases drastically as amplitude decreases, so it becomes very difficult to find the transition amplitudes numerically. In fact, adjacent amplitudes in a numerical sample are typically multiple steps apart once the evolution is already long, which justifies using the perturbative scaling $t_H \propto \epsilon^{-2}$.

Based on the perturbative scaling relation, initial data can be divided into several classes with respect to behavior at low amplitudes, as illustrated in figure 2.1 for massless scalars. *Stable* initial data evolves indefinitely without forming a horizon. In practice, we identify this type of behavior in numerical evolutions by noting rapid horizon formation at high amplitude with a vertical asymptote in t_H just above some critical amplitude. In our numerical results, we see a sudden jump at the critical amplitude to evolutions with no horizon formation to a large time t_{lim} , possibly with a small window of amplitudes with large t_H just above the critical amplitude. In a few cases, we have captured a greater portion of the asymptotic region. See figure 2.1a. *Unstable* initial data, in contrast, forms a horizon at all amplitudes following the perturbative scaling relation $t_H \propto \epsilon^{-2}$ as $\epsilon \rightarrow 0$. In our analysis, we will verify this scaling by fitting t_H to a power law as described in section 2.3.2 below; if we limit the fit to smaller values of ϵ , the scaling becomes more accurate. Figure 2.1b shows unstable data. The red curve is of the form $t_H = a\epsilon^{-2} + b$ with a, b determined by matching the curve to the data for the largest two amplitudes with $t_H \geq 60$ (not a best fit); note that the data roughly follows this curve. The categorization of different initial data profiles with similar characteristic widths into stable and unstable is robust for massless and massive scalars [34]; small and large width initial data are unstable, while intermediate widths are stable. One of the major results of this paper is determining how the widths of initial data in these “islands of stability” vary with scalar mass.

A priori, there are other possible types of behavior, at least beyond the first subleading order in perturbation theory, that is, at finite ϵ . *Metastable* initial data collapses with $t_H \propto \epsilon^{-p}$ with $p > 2$ at small but not arbitrarily small amplitudes (or another more rapid growth of t_H with decreasing amplitude). We will find this type of behavior common on the “shoreline” of islands of stability where stable behavior transitions to unstable. As we will discuss further below, metastable behavior may or may not continue as $\epsilon \rightarrow 0$; in principle, as higher order terms in perturbation theory become less important, the behavior may shift to either stable or unstable as described above. In principle, initial data that is stable at third order in perturbation theory but unstable at higher order could have metastable scaling even in the $\epsilon \rightarrow 0$ limit, though our numerical study cannot address this case. We in fact find circumstantial evidence in favor of the different possibilities. In the case that the $\epsilon \rightarrow 0$ behavior is perturbatively unstable, the perturbative scaling $t_H \propto \epsilon^{-2}$ only appears for larger t_H than the typical unstable case; it may therefore be reasonable for the reader to consider metastable initial data as part of a second order transition between unstable and stable classes of initial data. Figure 2.1c shows metastable initial data that continues to collapse to times $t_H \sim 0.6t_{lim}$ but more slowly than ϵ^{-2} ; note that t_H for collapsed evolutions at small amplitudes lies significantly above the curve $t_H = a\epsilon^{-2} + b$ (which is determined as in figure 2.1b). There was one additional type of behavior identified by [34], which was called “quasi-stable” initial data at the time since the low-amplitude behavior was not yet clear. We find here that these initial data are typically stable at small amplitude but exhibit irregular behavior in t_H as a function of ϵ , so we will denote them as *irregular* initial data; irregular behavior may be strongly non-monotonic or even exhibit some evidence of chaos. Figure 2.1d shows an example of irregular initial data. Later, we will see more striking examples of this behavior for massive scalars.

We emphasize that we are not claiming that metastable or irregular behavior persist to arbitrarily small amplitudes (though a priori metastable behavior could). In that sense, the multiscale perturbation theory suggests that the only two classes of stability behavior are stable and unstable with $t_H \propto \epsilon^{-2}$ scaling as $\epsilon \rightarrow 0$. However, it is also important to understand physics outside the perturbative regime, and classifying the behavior of AdS when higher-order or nonperturbative ef-

fects contribute is still of interest. For example, it is clear that metastable initial data (as defined precisely below) does not exhibit perturbatively unstable behavior for t_H values as small as other unstable initial data, even in the cases where it may at all. This may help understanding the breakdown of the multiscale perturbation theory. Similarly, irregular initial data leads to qualitatively different behavior even visually and suggests that nonperturbative dynamics are important. It is in the spirit of looking beyond the multiscale perturbation theory that we call metastable and irregular initial data independent classes of behavior, even if they are not quite on the same standing as perturbatively stable or unstable classes. This paper presents the first systematic mapping of where these distinct behaviors appear.

2.3.2 Methods

For spherically symmetric motion, the Klein-Gordon equation for scalar mass μ can be written in first order form as

$$\phi_{,t} = Ae^{-\delta}\Pi, \quad \Phi_{,t} = (Ae^{-\delta}\Pi)_{,x}, \quad (2.2)$$

$$\Pi_{,t} = \frac{(Ae^{-\delta}\tan^{d-1}(x)\Phi)_{,x}}{\tan^{d-1}(x)} - \frac{e^{-\delta}\mu^2\phi}{\cos^2(x)}, \quad (2.3)$$

where Π is the canonical momentum and $\Phi = \phi_{,x}$ is an auxiliary variable. The Einstein equation reduces to constraints, which can be written as

$$\delta_{,x} = -\sin(x)\cos(x)(\Pi^2 + \Phi^2) \quad (2.4)$$

$$M_{,x} = (\tan(x))^{d-1} \left[A \frac{(\Pi^2 + \Phi^2)}{2} + \frac{\mu^2\phi^2}{2\cos^2(x)} \right], \quad (2.5)$$

$$A = 1 - 2 \frac{\sin^2(x)}{(d-1)} \frac{M}{\tan^d(x)}, \quad (2.6)$$

where the mass function M asymptotes to the conserved ADM mass at the boundary $x = \pi/2$. We will restrict to $d = 4$ spatial dimensions. Since results are robust against changes in the type of initial data [34], we can take the initial data to be a Gaussian of the areal radius in the canonical momentum and trivial in the field. Specifically,

$$\Pi(t=0, x) = \epsilon \exp\left(-\frac{\tan^2(x)}{\sigma^2}\right), \quad \phi(t=0, x) = 0. \quad (2.7)$$

The width σ and field mass μ constitute the parameter space for our stability phase diagram.

We solve the Klein-Gordon evolution equations (2.2,2.3) and Einstein constraint equations (2.4,2.5) numerically using methods similar to those of [20] on a spatial grid of $2^n + 1$ grid points; we discuss the convergence properties of our code in the appendix. We denote the approximate horizon position x_H and formation time t_H by the first point such that $A(x_H, t_H) \leq 2^{7-n}$. In detail, we evolve the system in time using a 4th-order Runge-Kutta stepper and initially use a 4th-order Runge-Kutta spatial integrator at resolution $n = 14$. If necessary, we switch to a 5th-order Dormand-Prince spatial integrator and increase resolution near horizon formation. Due to time constraints, we do not increase the resolution beyond $n = 21$ for any particular calculation; if a higher resolution would be required to track horizon formation for a given amplitude, we exclude that amplitude.

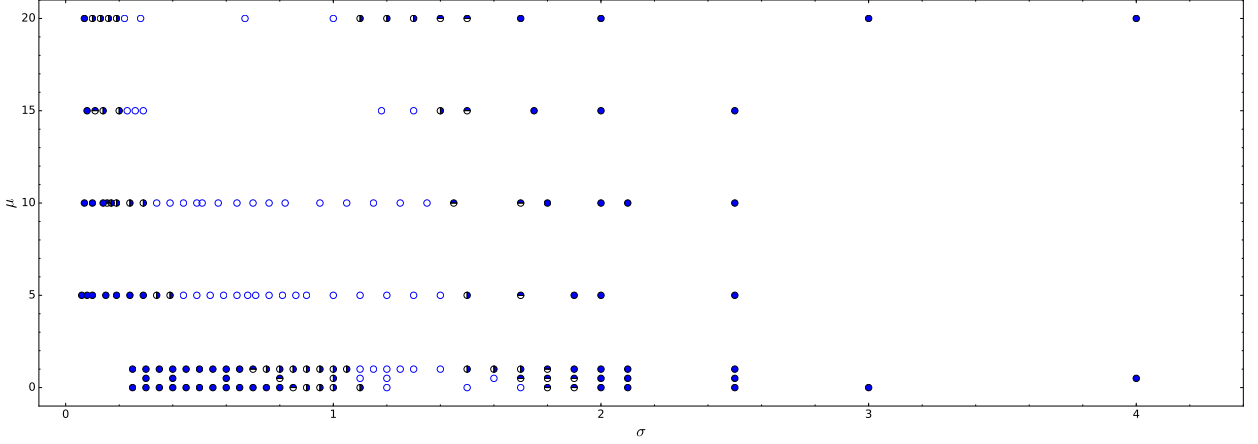


Figure 2.2: Stability phase diagram as a function of initial data width σ and scalar mass μ . Filled circles represent unstable initial data, empty circles stable initial data, top-half-filled circles metastability, and right-half-filled circles irregular behavior.

To determine the stability class of initial data with a given width σ , we allow evolutions to run to a maximum time of $t_{lim} = 500$ in AdS units, so t_{lim} is a lower limit for t_H for amplitudes that do not form a horizon within that time. Normally, however, if the initial data appears unstable, we only evolve amplitudes with $t_H \lesssim 0.6t_{lim}$; this is partly to save computational resources and partly to distinguish stable evolutions from collapsing ones. For unstable or metastable initial data, we find the best fit of the form $t_H = ae^{-p} + b$ to evolutions with $t_H > t_{fit}$, where t_{fit} is a constant time chosen such that amplitudes with evolutions that last longer are usually roughly perturbative;¹ in practice, $t_{fit} = 60$ gives results close to the perturbative result $p = 2$ for evolutions expected to be unstable from the literature, but we will also consider $t_{fit} = 80, 100$ as described below. In other words, since a given amplitude ϵ may be in the perturbative scaling regime for one set of initial data but nonperturbative for another, we compare initial data at similar horizon formation times (addressing the onset of perturbative behavior). Choosing t_{fit} as above gives consistent values of the fit parameters for the three values of t_{fit} for the largest and smallest initial data widths, which are unstable.

2.4 Phase Diagram of Stability

Here we give our main result, the phase diagram of stability classes as a function of initial profile width and scalar mass, along with a more detailed discussion of the scaling of horizon formation time with amplitude for varying initial data.

The stability phase diagram for spherically symmetric scalar field collapse in AdS₅, treating the width σ of initial data and scalar field mass μ as tunable parameters, appears in figure 2.2. Each (μ, σ) combination that we evolved numerically is indicated by a circle, with filled and empty circles representing unstable and stable initial data respectively. The metastable class is represented by

¹The power law plus constant fits the leading and first subleading contribution to t_H in a perturbative expansion in ϵ , and we have found that the subleading term is typically not negligible in the computationally accessible regime.

circles filled in the top half, while the irregular class are filled in the right half. At a glance, two features of the stability phase diagram are apparent: as μ increases, the island of stability moves toward smaller values of σ and takes up a gradually larger range of σ . To be specific, the stable class of initial data is centered at $\sigma = \bar{\sigma} \sim 1.4$ and has a width of $\Delta\sigma \sim 0.7$ for $\mu = 0, 0.5$, with $\bar{\sigma} \sim 1.2$ for $\mu = 1$. $\Delta\sigma$ increases to ~ 1.1 , and the island of stability is centered at $\bar{\sigma} \sim 0.9$ for $\mu = 5, 10$, while $\Delta\sigma \sim 1.2$ for $\mu = 15, 20$ with the stable class centered at $\bar{\sigma} \sim 0.8$. Note that the transition between “light field” and “heavy field” behavior occurs for $\mu > 1$ in AdS units.

The metastable and irregular classes appear at the shorelines of the island of stability, the boundary between unstable and stable classes. In particular, the slope of the power law $t_H \sim \epsilon^{-p}$ as $\epsilon \rightarrow 0$ increases as the width moves toward the island of stability, leading to metastable behavior. We find metastability at the large σ shoreline for all μ values considered and also at the small σ shoreline for several scalar masses. It seems likely that metastable behavior appears in only a narrow range of σ for larger μ , which makes it harder to detect in a numerical search, leading to its absence in some parts of the stability phase diagram. We find irregular behavior at the small σ shoreline for every mass and at the large σ boundary for large μ , closer to stable values of σ than metastable initial data. This class of initial data includes a variety of irregular and non-monotonic behavior, as detailed below. Evidence for chaotic behavior especially becomes more prominent at larger values of μ , as we will discuss below.

2.4.1 Metastable versus unstable initial data

While stable and irregular initial data are typically apparent by eye in a plot of t_H vs ϵ , distinguishing the unstable from metastable classes is a quantitative task. As we described in section 2.3.2, we find the least squares fit of $t_H = a\epsilon^{-p} + b$ to all evolutions with $t_H > t_{fit}$ for the given (μ, σ) , running over values $t_{fit} = 60, 80, 100$. Using the covariance matrix of the fit, we also find the standard error for each fit parameter. We classify a width as having unstable evolution if the best fit value of p is within two standard errors of $p = 2$ for $t_{fit} = 60, 80$ or one standard error for $t_{fit} = 100$ (due to a smaller number of data points, the standard errors for $t_{fit} = 100$ tend to be considerably larger). In contrast, we classify a width as having metastable evolution if the best fit p is statistically significantly different from 2 (in that the best fit value is more than 2 standard errors from $p = 2$ for $t_{fit} = 60, 80$ and more than 1 standard error from $p = 2$ for $t_{fit} = 100$). This indicates that either further subleading contributions in a perturbative expansion of t_H are non-negligible in this regime for metastable initial data or that possibly metastable initial data are stable at the first nontrivial order in perturbation theory. Considering larger values of t_{fit} helps to ensure that the leading perturbative terms do not come to dominate for particular initial profile at the smallest computationally accessible amplitude values. In the case that the fit to $t_H = a\epsilon^{-p} + b$ has large reduced χ^2 or is sensitive to fitting algorithm, the data is not well-described by our fitting function, so we classify it as irregular (see the next subsection).

The fits $t_H = a\epsilon^{-p} + b$ allow us to explore the time scale of horizon formation across the stability phase diagram, for example through a contour plot of one of the coefficients vs σ and μ . In most cases, this has not been informative, but an intriguing feature emerges if we plot the normalization coefficient a vs σ for unstable initial data at small σ , as shown in figure 2.3 for $t_{fit} = 60$. By eye, the coefficient is reasonably well described by the fit $a = (32.0 \pm 0.3)\sigma^{-(2.01 \pm 0.02)}$ (values following \pm are standard errors of the best fit values) *independent of scalar field mass*. This is not born out

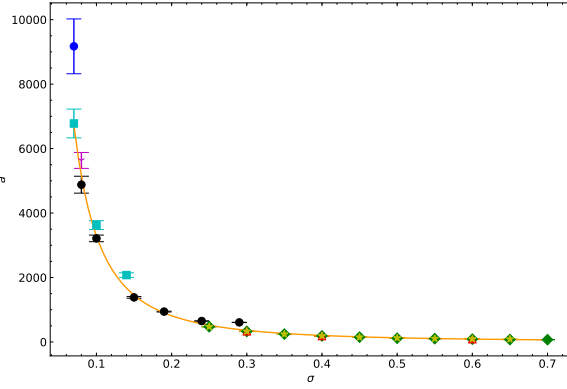


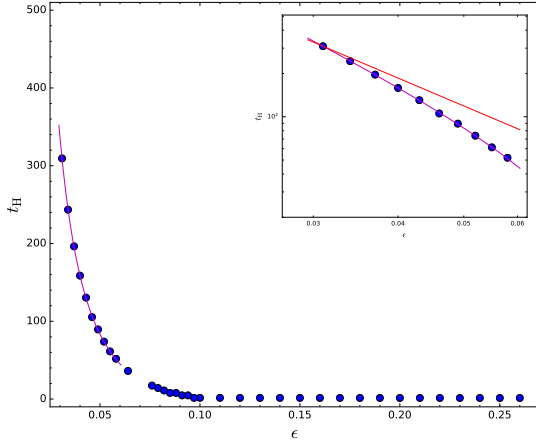
Figure 2.3: Coefficient a from the fit $t_H = a\epsilon^{-p} + b$ as a function of width σ using $t_{fit} = 60$. Shows data for $\mu = 0$ (green diamonds), 0.5 (red triangles), 1 (yellow stars), 5 (black circles), 10 (cyan squares), 15 (magenta Y), and 20 (blue circles). The orange line is the best power law fit.

very well quantitatively; the reduced χ^2 for the fit is $\chi^2/\text{d.o.f.} = 180$, indicating a poor fit. However, the large χ^2 seems largely driven by a few outlier points with large scalar mass, so it is tempting to speculate that the gravitational collapse in this region of parameter space is driven by gradient energy, making all fields effectively massless at narrow enough initial σ . The picture is qualitatively similar if we consider the parameter a for $t_{fit} = 80, 100$ instead.

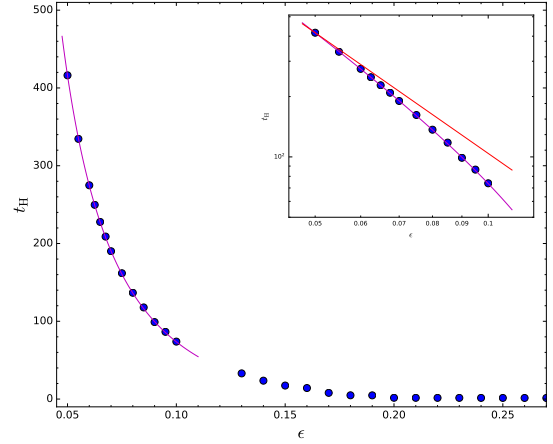
Several examples of metastable behavior appear in figure 2.4. These figures show both data from the numerical evolutions (blue dots and red triangles) and fits of the form $t_H = a\epsilon^{-p} + b$ for points with $t_H > t_{fit} = 60$ (magenta curves). The best fit parameters are given in table 2.1 along with the standard errors (listed following \pm for the fit values) and χ^2 values. The insets show the fit region with a log-log scale and an additional line (red) showing an ϵ^{-2} power law normalized to fit the smallest amplitude shown in the inset. It is visually clear that t_H grows faster than ϵ^{-2} for all these examples as ϵ decreases in the fit region (there is a significant constant offset in figure 2.4d).

Figures 2.4a,2.4b demonstrate behavior typical of most of the instances of metastable initial data we have found; specifically, the initial data continue to collapse through horizon formation times of $t_H \sim 0.6t_{lim}$ but with p significantly greater than the perturbative value of $p = 2$. Note that the evolutions of figure 2.4b have been extended to larger values of t_H to demonstrate that the evolutions continue to collapse to somewhat smaller amplitude values. Figure 2.4b is also of interest because its best fit value $p \approx 2.07 \pm 0.02$ is approximately as close to the perturbative value as several stable sets of initial data but has a smaller standard error for the fit, so the difference from the perturbative value is more significant (again, the value following the \pm is the standard error).

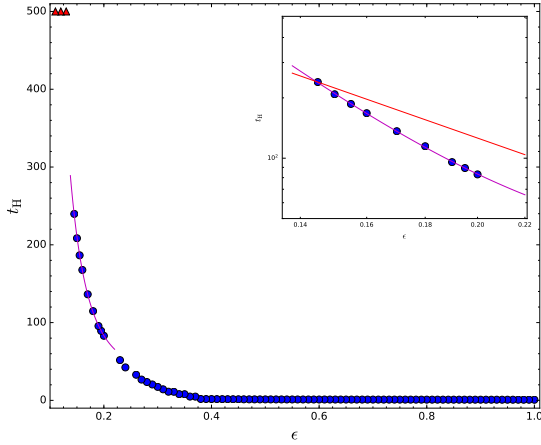
Figure 2.4c shows metastable evolution to $t_H \lesssim 0.6t_{lim}$ but then a sudden jump to stability until $t = t_{lim}$. In the figure, the fit has been extended to the largest non-collapsing amplitude, which demonstrates that there is no collapse over a time period significantly longer than the fit predicts. This example argues that metastable data may in fact become stable at the smallest amplitudes. On the other hand, figure 2.4d shows a similar jump in t_H to values $t_H < t_{lim}$; evolution at lower amplitudes shows metastable scaling with $p \approx 5.6 \pm 0.8$ for $360 < t_H < t_{lim}$. The figure also shows a metastable fit with larger reduced χ^2 at larger amplitudes corresponding to $t_{fit} < t_H < 0.4t_{lim}$. So



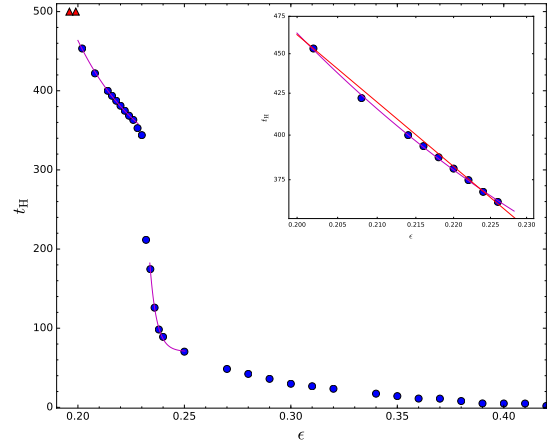
(a) $\mu = 15, \sigma = 1.5$



(b) $\mu = 5, \sigma = 1.7$



(c) $\mu = 0, \sigma = 1.8$



(d) $\mu = 0.5, \sigma = 1.7$

Figure 2.4: Metastable behavior: blue dots represent horizon formation and red triangles a lower limit on t_H . Magenta curves are fits $t_H = a\epsilon^{-p} + b$ over the shown range of amplitudes. Insets show the fit region with log-log scale; note that the fit is not strictly a power law, so the fits are not straight lines. See table 2.1 for best fit parameters. Red lines in insets are ϵ^{-2} power laws normalized to the t_H of the smallest amplitude shown.

this is another option: metastable behavior may transition abruptly to metastable behavior with different scaling (or possibly even perturbatively unstable behavior) at sufficiently small amplitudes. It is also reasonable to classify this case as irregular due to the sudden jump in t_H ; we choose metastable due to the clean metastable behavior at low amplitudes.

Our point of view is that initial data in the metastable class is distinct from the unstable class at finite amplitudes corresponding to $t_{fit} < t_H < 300$; they take longer to collapse at a fixed small value of ϵ than would be expected by the perturbative scaling. An alternate point of view is to ask whether we can determine if a given set of initial data is perturbatively unstable in the $\epsilon \rightarrow 0$ limit. We have already seen that metastable initial data does not follow the perturbative scaling when fit

	a	p	b	$\chi^2/\text{d.o.f.}$
$\mu = 15, \sigma = 1.5$	0.10 ± 0.01	2.33 ± 0.05	-27 ± 4	0.7736
$\mu = 5, \sigma = 1.7$	0.91 ± 0.06	2.07 ± 0.02	-33 ± 2	0.5070
$\mu = 0, \sigma = 1.8$	0.06 ± 0.02	4.3 ± 0.2	30 ± 5	1.502
$\mu = 0.5, \sigma = 1.7$ ($t_H < 0.4t_{lim}$)	$(4 \pm 32) \times 10^{-45}$	73 ± 5	70 ± 2	5.409
$(t_H > 0.72t_{lim})$	0.02 ± 0.03	5.6 ± 0.8	260 ± 20	1.078

Table 2.1: Best fit parameters for the cases shown in figure 2.4 restricting to $t_H > t_{fit} = 60$ and as noted. Listed errors (\pm values) are standard errors. $\chi^2/\text{d.o.f.}$ is the reduced χ^2 value used as a measure of goodness-of-fit.

to $t_H = a\epsilon^{-p} + b$, the first two terms of the perturbative expansion. However, it is possible that a perturbative description applies but requires a further subleading term. To test this hypothesis, we fit unstable and metastable initial data to $t_H = a\epsilon^{-p} + b + c\epsilon^2$; as described earlier in this section, we determine if p is within two standard errors of the perturbative value $p = 2$ (or one standard error for $t_{fit} = 100$).

The unstable class of initial data is instructive. For the new fits of unstable initial data, p is statistically equal to 2, and the new values of a, p, b are consistent with the values from the old fits to within two standard errors (or sometimes slightly more). The fit value of c is uniformly within a standard error of zero, and, for the amplitude values in the fit region, the ϵ^2 term is small compared to the constant and ϵ^{-2} terms. What is more, for some unstable initial data near the island of stability, the original $t_H = a\epsilon^{-p} + b$ fits for $t_{fit} = 60$ have $p > 2$ statistically; on the other hand, the new fits have $p = 2$ within statistical error. In other words, the perturbative expansion is still valid but requires more terms. Part of the metastable class of initial data also behaves in this manner and could therefore be reasonably considered to be perturbatively unstable. Of the metastable initial data we found, these are $\sigma = 1.9$ for $\mu = 0$, $\sigma = 0.8$ and 1.9 for $\mu = 0.5$, $\sigma = 0.7$ for $\mu = 1$, $\sigma = 1.7$ for $\mu = 5$, $\sigma = 0.155$ for $\mu = 10$, $\sigma = 0.11$ and 1.5 for $\mu = 15$, and $\sigma = 1.5$ for $\mu = 20$. In addition, $\mu = 1, \sigma = 1.8$ and $\mu = 10, \sigma = 1.7$ initial data have similar behavior, but p is not statistically consistent with 2 for any of the fit regions, though it is closer than in the original fits. On the other hand, the other metastable initial data ($\sigma = 0.85$ and 1.8 for $\mu = 0$, $\sigma = 1.7$ and 1.8 for $\mu = 0.5$, $\sigma = 1.45$ for $\mu = 10$, and $\sigma = 1.4$ for $\mu = 20$) show no evidence for perturbative behavior. Specifically, p remains statistically larger than 2 for all fits, the ϵ^2 term in the new fit is roughly the same magnitude as the other terms, and the a, p, b values in the new fits are not statistically consistent with the original fits.

2.4.2 Irregular behaviors

We have found a variety of irregular behaviors at the transition between the metastable and stable classes which we have classified together as irregular initial data; however, it may be better to describe them as separate classes. The stability phase diagram 2.2 indicates that the irregular class extends along the “inland” side of the small σ shoreline and at least part of the large σ shoreline

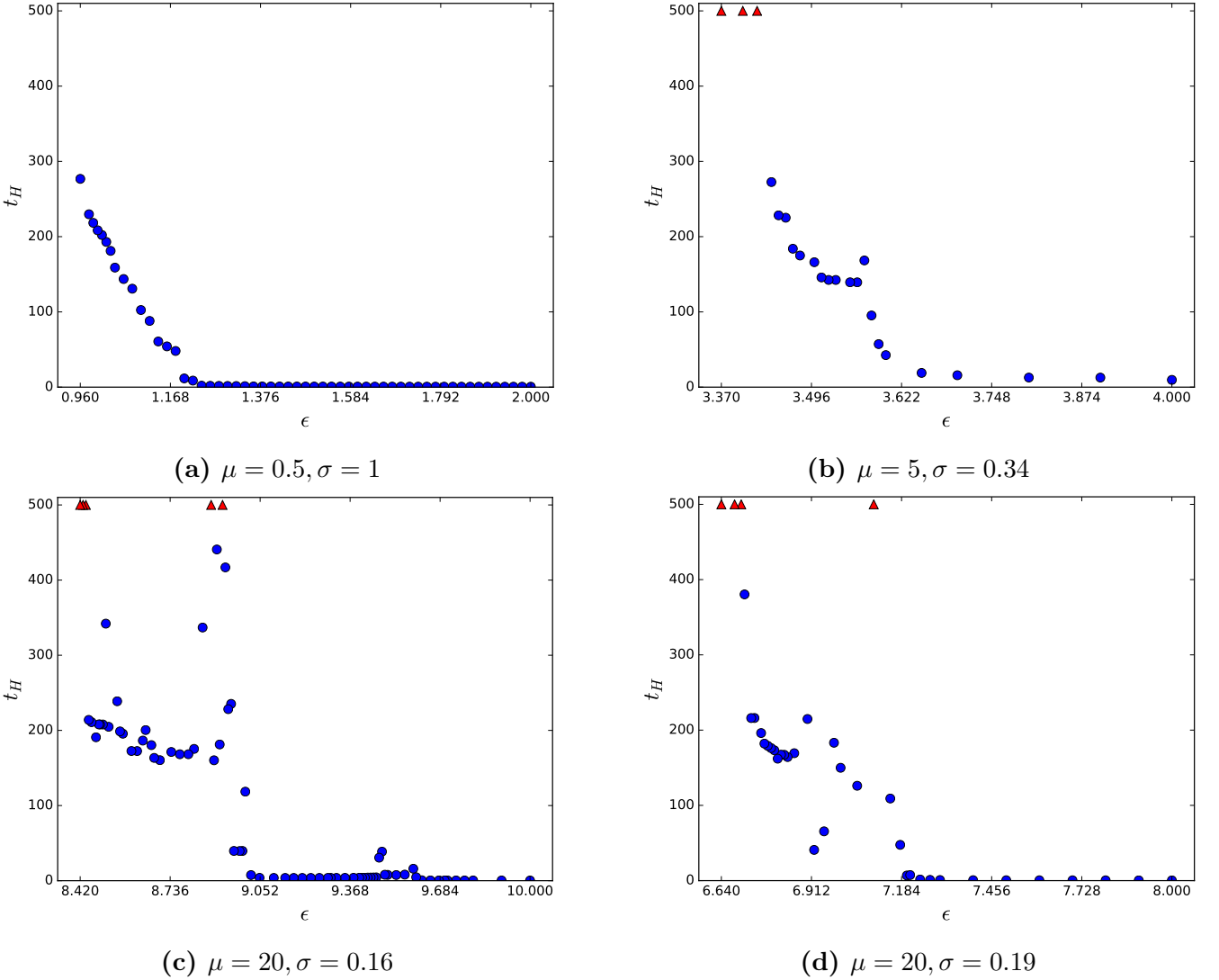


Figure 2.5: Irregular behavior: blue dots represent horizon formation and red triangles a lower limit on t_H .

of the island of stability. What is not clear from our evolutions up to now is whether each type of behavior appears along the entire shoreline or if they appear in pockets at different scalar field masses. Examples of each type of behavior that we have found appear in figure 2.5.

The first type of irregular behavior, shown in figure 2.5a, is monotonic (t_H increases with decreasing ϵ as usual), but it is not well fit by a power law. In fact, this behavior would classify as metastable by the criterion of section 2.4.1 in that the power law of the best fit $t_H = a\epsilon^{-p} + b$ is significantly different from $p = 2$, except for the fact that the reduced χ^2 value for the fit is very large (greater than 10) and also that different fitting algorithms can return significantly different fits, even though the data may appear to the eye like a smooth power law. In any case, this type of behavior apparently indicates a breakdown of metastable behavior and hints at the appearance of non-monotonicity. So far, our evolutions have not demonstrated sudden jumps in t_H typical of stability at low amplitudes, however.

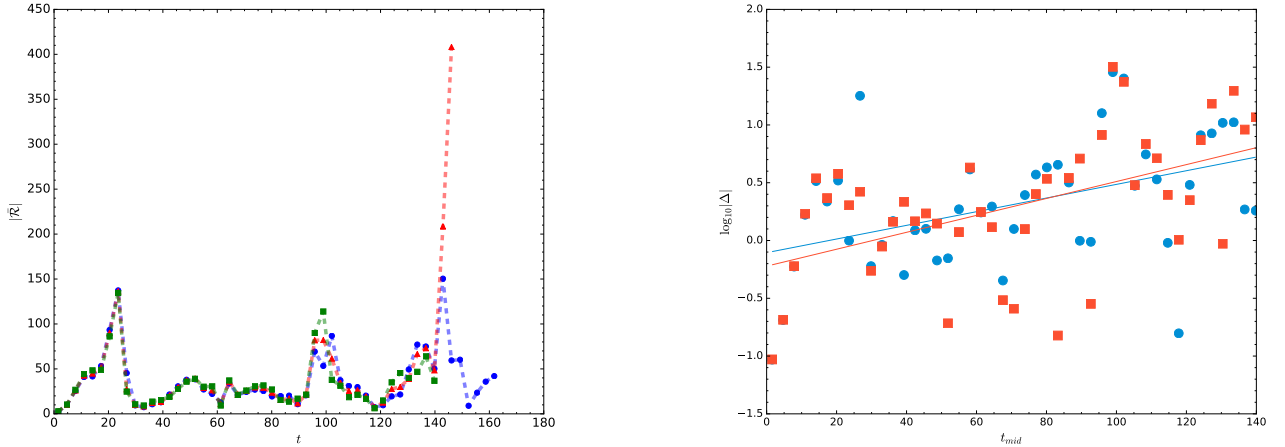
Figure 2.5b exemplifies non-monotonic behavior in the irregular class. This type of behavior, which was noted already by [18], involves one or more sudden jumps in t_H as ϵ decreases, which may be followed by a sudden decrease in t_H and then resumed smooth monotonic increase in t_H . There are suggestions that this type of initial data is stable at low amplitudes due to the usual appearance of non-collapsing evolutions, but it is worth noting that these amplitudes could instead experience another jump and decrease in t_H , just at $t_H > t_{lim}$. Finally, [34] studied this type of behavior in some detail, denoting it as “quasi-stable.”

Some irregular initial data demonstrates evidence of chaotic behavior, in that t_H appears to be sensitive to initial conditions (ie, value of amplitude) over some range of amplitudes. This type of behavior appears over the range of masses (see figure 2.1d for a mild case for massless scalars), but it is more common and more dramatic at larger μ . Figures 2.5c,2.5d represent the most extreme behavior of this type among the initial data that we studied with collapse at $t_H < 50$ not very far separated from amplitudes that do not collapse for $t < t_{lim}$ along with an unpredictable pattern of variation in t_H . This type of evidence for chaotic behavior has been seen previously in the collapse of transparent but gravitationally interacting thin shells in AdS [39] as well as in the collapse of massless scalars in AdS₅ Einstein-Gauss-Bonnet gravity [30, 31]; these references speculated that the t_H vs ϵ curve is fractal. In both cases, this type of behavior is hypothesized to be due to the transfer of energy between two infalling shells, with horizon formation only proceeding when one shell is sufficiently energetic. In the latter case, the extra scale of the theory (given by the coefficient of the Gauss-Bonnet term in the action) leads the single initial pulse of scalar matter to break into two pulses.

We should therefore ask two questions: does this irregular behavior show evidence of true chaos, and is a similar mechanism at work here? We note first that [30] found evidence (using a modified box test) that the t_H vs ϵ curve has a non-integer fractal dimension for plots visually similar to our figures 2.5c,2.5d. Here, to quantify the presence of chaos, we examine the difference in time evolution between similar initial conditions (nearby amplitudes), which diverge exponentially in chaotic systems. Specifically, any quantity Δ should satisfy $|\Delta| \propto \exp(\lambda t)$ for Lyapunov coefficient λ . Our characteristic will be the upper envelope of the Ricci scalar at the origin per light crossing time, $\bar{\mathcal{R}}(t)$. We consider three sets of irregular initial data: a massless scalar of width $\sigma = 1.1$ with amplitudes $\epsilon = 1.02, 1.01, 1.00$ (see figure 2.1d), a $\mu = 5$ massive scalar of width $\sigma = 0.34$ and $\epsilon = 3.52, 3.51, 3.50$, and a $\mu = 20$ scalar of width $\sigma = 0.19$ and $\epsilon = 6.98, 6.95, 6.92$ (figure 2.5d). We also calculated determined the Lyapunov coefficient for unstable initial data with $\mu = 0.5$, $\sigma = 0.3$, and $\epsilon = 1.22, 1.20, 1.18$ for comparison.

Figure 2.6 details evidence for chaotic evolution in the $\mu = 5, \sigma = 0.34$ case; figure 2.6a shows our characteristic function $\bar{\mathcal{R}}(t)$ for the amplitudes $\epsilon_1 = 3.50, \epsilon_2 = 3.51$, and $\epsilon_3 = 3.52$. By eye, $\bar{\mathcal{R}}$ shows noticeable differences after a long period of evolution. These are more apparent in figure 2.6b, which shows the log of the differences $\Delta_{ab} \equiv \bar{\mathcal{R}}_{\epsilon_a} - \bar{\mathcal{R}}_{\epsilon_b}$, along with the best fits. Although there is considerable noise — or oscillation around exponential growth — in the differences (leading to R^2 values $\sim 0.2, 0.26$ for the fits), the average slope gives Lyapunov coefficient $\lambda = 0.007$ (within the error bar of each slope), and each slope differs from zero by more than 3 standard errors. One interesting point is that the t_H vs ϵ curve in figure 2.5b does not appear chaotic to the eye, even though it shows some of the mathematical signatures of chaos at least for $\epsilon_1 < \epsilon < \epsilon_3$ (the visible spike in t_H is at $\epsilon \sim 3.57$).

The story is similar for the massless and $\mu = 20$ cases we studied, which exhibit λ values that differ



(a) Upper envelope of Ricci scalar at origin

(b) $\log(|\Delta|)$ vs. t_{mid}

Figure 2.6: Left: The upper envelope of the Ricci scalar for amplitudes $\epsilon_1 = 3.50$ (blue circles), $\epsilon_2 = 3.51$ (red triangles), and $\epsilon_3 = 3.52$ (green squares) for $\mu = 5, \sigma = 0.34$. Right: $\log(|\Delta_{12}|)$ and best fit (blue circles and line) and $\log(|\Delta_{23}|)$ and best fit (red squares and line), calculated as a function of the midpoint t_{mid} of the time interval.

		λ	average λ
$\mu = 0, \sigma = 1.1$	Δ_{12}	0.011 ± 0.005	0.011
	Δ_{23}	0.011 ± 0.005	
$\mu = 0.5, \sigma = 0.3$	Δ_{12}	0.021 ± 0.0007	0.022
	Δ_{23}	0.024 ± 0.001	
$\mu = 5, \sigma = 0.34$	Δ_{12}	0.006 ± 0.002	0.007
	Δ_{23}	0.007 ± 0.002	
$\mu = 20, \sigma = 0.19$	Δ_{12}	0.046 ± 0.009	0.032
	Δ_{23}	0.019 ± 0.007	

Table 2.2: Best fit Lyapunov coefficients λ for adjacent amplitude pairs and average λ value for each μ, σ system studied. Standard errors are given following \pm signs.

from zero by at least 1.9 standard errors; see table 2.2. This is a milder version of the behavior noted by [30, 31, 39], especially for the $\mu = 5$ case studied. One thing to note is that the strength of oscillation in $\log(|\Delta|)$ around the linear fit increases with increasing mass, so that the two best fit Lyapunov exponents for $\mu = 20$ are no longer consistent with each other at the 1-standard deviation level. We should note, however that the unstable initial data with $\mu = 0.5, \sigma = 0.3$ also exhibits a statistically positive Lyapunov exponent, though we should note that the value of λ quoted in table 2.2 includes the time shortly before horizon formation, which does increase λ somewhat (though not more than the quoted error).

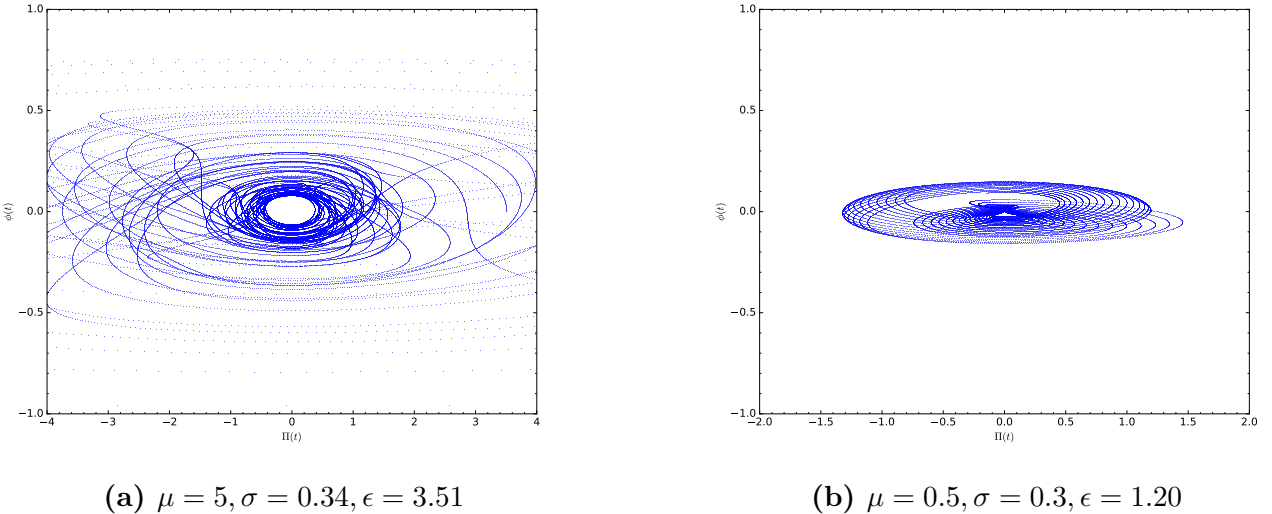
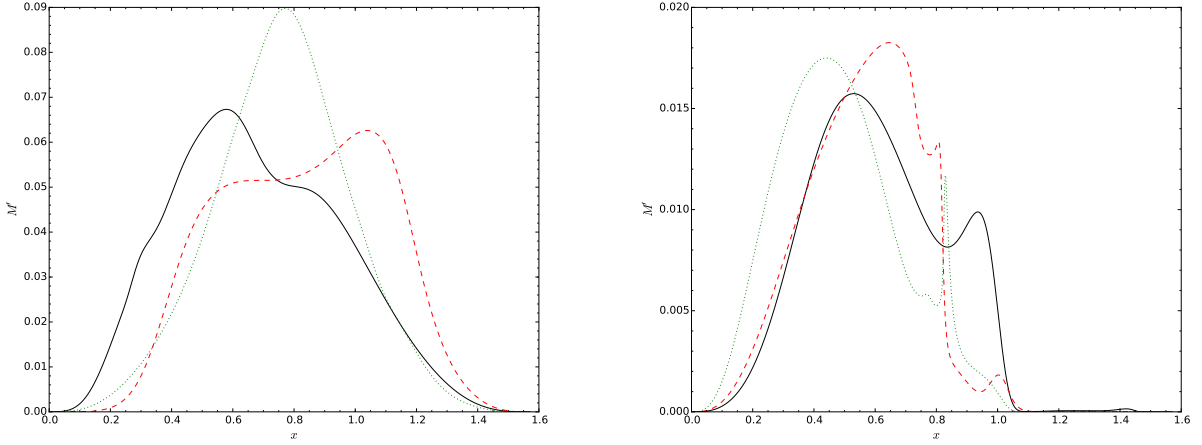


Figure 2.7: Trajectories in $\Pi(x=0), \phi(x=0)$ phase space for one irregular and one unstable evolution. Trajectories are shown for $t < 50$.

Since the Lyapunov coefficients do not distinguish the irregular and unstable cases, we also consider the phase space trajectories of the evolutions. Following [40], we consider the trajectory of evolutions in Π and ϕ evaluated at the origin for $t \leq 50$ in figure 2.7. Neither the $\mu = 5, \sigma = 0.34, \epsilon = 3.51$ (figure 2.7a) or $\mu = 0.5, \sigma = 0.3, \epsilon = 1.20$ (figure 2.7b) trajectories close, though there is a clear difference. Specifically, the former trajectory is visually disorganized (that is, strongly varying orbits) with very rapid motion (seen in the gap between points on the trajectory between plotted time steps). Meanwhile, the latter motion is comparatively regular, typical of quasi-periodic motion. Figure 2.7a is typical of turbulence and clearly shows that these evolutions are nonperturbative, even though t_H is large (well into the perturbative regime for unstable initial data).

To sum up, we have identified irregular initial data that shows evidence of chaotic behavior. Specifically, several of the t_H vs ϵ curves appear qualitatively similar to analogous plots in [30, 31, 39], which were demonstrated to have fractal-like behavior (including fractional fractal dimension in one case). Furthermore, a number of cases of irregular initial data (and some unstable) have positive Lyapunov exponents; phase space trajectories for irregular initial data show very rapid motion typical of turbulence, while unstable initial data have more regular trajectories. Taken together, this is strong evidence for chaotic behavior for some irregular initial data, similar to that discussed in other studies of gravitational collapse in AdS. Furthermore, this is the first evidence of chaos in the t_H vs ϵ curve for gravitational collapse of a massless scalar in AdS to our knowledge.

The mechanism underlying the possibly chaotic behavior seems somewhat different or at least weaker than the two-shell or Einstein-Gauss-Bonnet systems. When examining the time evolution of the mass distributions of these data, we see a single large pulse of mass energy that oscillates between the origin and boundary without developing a pronounced peak. However, there is also apparently a smaller wave that travels across the large pulse. We can see this by comparing snapshots of the mass distribution at different times, as in figure 2.8. In the massless case examined, this wave deforms the pulse, leading to a double-shoulder appearance seen at two times in figure 2.8a. In the $\mu = 5, \sigma = 0.34$ case, the secondary wave is more like a ripple, usually smaller in amplitude but more



(a) $\mu = 0, \sigma = 1.1, \epsilon = 1.01$, at times $t = 60$ (solid black), $t = 62$ (dashed red), $t = 64$ (dotted green) **(b)** $\mu = 5, \sigma = 0.34, \epsilon = 3.52$, at times $t = 132$ (solid black), $t = 137$ (dashed red), $t = 140$ (dotted green)

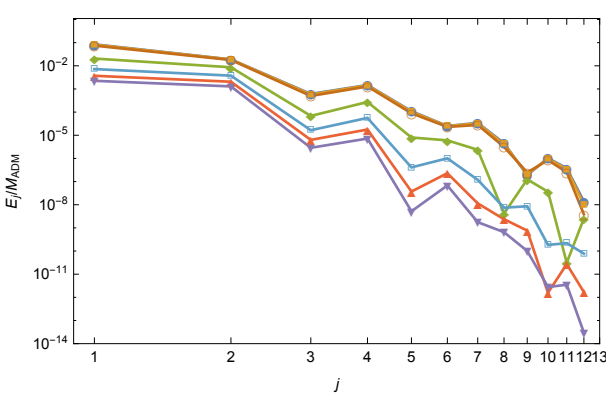
Figure 2.8: Radial derivative of the mass function at the indicated time for two systems that show evidence of chaos. Note the appearance of a secondary wave on top of the main pulse. (μ, σ, ϵ) as indicated.

sharply localized, as toward the right side of the main pulse in figure 2.8b. So the chaotic behavior may be caused by the relative motion of the two waves, rather than energy transfer between two shells. In this hypothesis, a horizon would form when both waves reach the neighborhood of the origin at the same time.

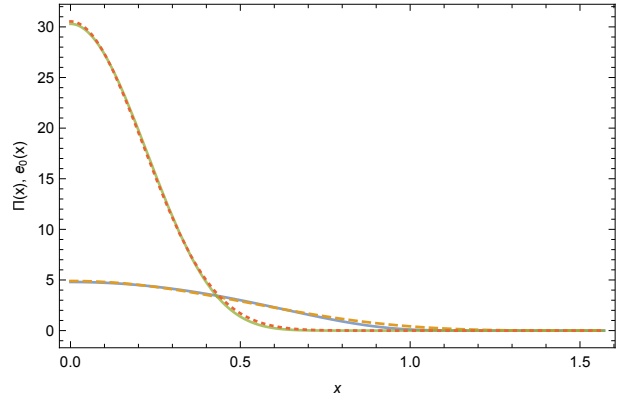
As a note, we have run convergence tests on several sets of irregular initial data and find that our calculations are convergent overall, as expected (even at lower resolution than we used). In particular, the massless scalar evolutions studied in table 2.2 are convergent already at resolution given by $n = 12$ (note that we typically start at $n = 14$); we also observe convergent behavior for the $\mu = 5$ evolutions discussed in table 2.2. We have therefore validated that nonmonotonic behavior and even evidence of chaos occurs. The only caveat may be for some of the apparently initial data with scalar mass $\mu = 20$, which nonetheless appear well-behaved according to other indicators. The reader may or may not wish to take them at face value but should recall that we have presented other chaotic initial data with rigorously convergent evolutions. See the appendix for a more detailed discussion.

2.5 Spectral analysis

As we discussed in the introduction, instability toward horizon formation proceeds through a turbulent cascade of energy to shorter wavelengths or, more quantitatively, to 1st-order scalar eigenmodes with more nodes. Inverse cascades are typical of stable evolutions. Therefore, understanding the energy spectrum of our evolutions, both initially and over time, sheds light on the behavior of the self-gravitating scalar field in asymptotically AdS spacetime, providing a heuristic analytic understanding of the stability phase diagram.



(a) Best fit gaussian energy spectra.



(b) Best fit gaussian and zeroth eigenmode.

Figure 2.9: Left: Spectra of the best fit gaussians (2.7) to the $j = 0$ eigenmode for masses $\mu = 0$ (blue circles), 0.5 (yellow squares), 1 (empty orange circles), 5 (green diamonds), 10 (empty cyan squares), 15 (upward red triangles), and 20 (downward purple triangles). Right: an overlay of the best fit Gaussian and e_0 eigenmode for $\mu = 0$ (solid blue is best fit, orange dashed is eigenmode) and $\mu = 20$ (solid green, red short dashes).

The (normalizable) eigenmodes e_j are given by Jacobi polynomials as

$$e_j(x) = \kappa_j \cos^{\lambda_+}(x) P_j^{(d/2-1, \sqrt{d^2+4\mu^2}/2)}(\cos(2x)) \quad (2.8)$$

(κ_j is a normalization constant) with eigenfrequency $\omega_j = 2j + \lambda_+$ and $\lambda_+ = (d + \sqrt{d^2 + 4\mu^2})/2$ in AdS_{d+1} for $j = 0, 1, \dots$ (see [41, 42] for reviews). Including gravitational backreaction, we define the energy spectrum

$$E_j \equiv \frac{1}{2} \left(\Pi_j^2 - \phi_j \ddot{\phi}_j \right), \quad (2.9)$$

where

$$\begin{aligned} \Pi_j &= (\sqrt{A}\Pi, e_j), \quad \phi_j = (\phi, e_j), \\ \ddot{\phi}_j &= (\cot^{d-1}(x)\partial_x [\tan^{d-1}(x)A\Phi] - \mu^2 \sec^2(x)\phi, e_j), \end{aligned} \quad (2.10)$$

and the inner product is $(f, g) = \int_0^{\pi/2} dx \tan^{d-1}(x) fg$. The sum of E_j over all modes is the conserved ADM mass.

2.5.1 Dependence on mass

The most visibly apparent feature of the stability phase diagram of figure 2.2 is that the island of stability both expands and shifts to smaller widths as the scalar mass increases. As it turns out, the energy spectrum of the Gaussian initial data (2.7) provides a simple heuristic explanation.

It is well established both in perturbation theory and numerical studies that initial data given by a single scalar linear-order eigenmode is in fact nonlinearly stable, and the spectra of many quasi-periodic solutions are also dominated by a single eigenmode. As a result, we should expect Gaussian initial data that approximates a single eigenmode (which must be $j = 0$ due to lack of nodes) to

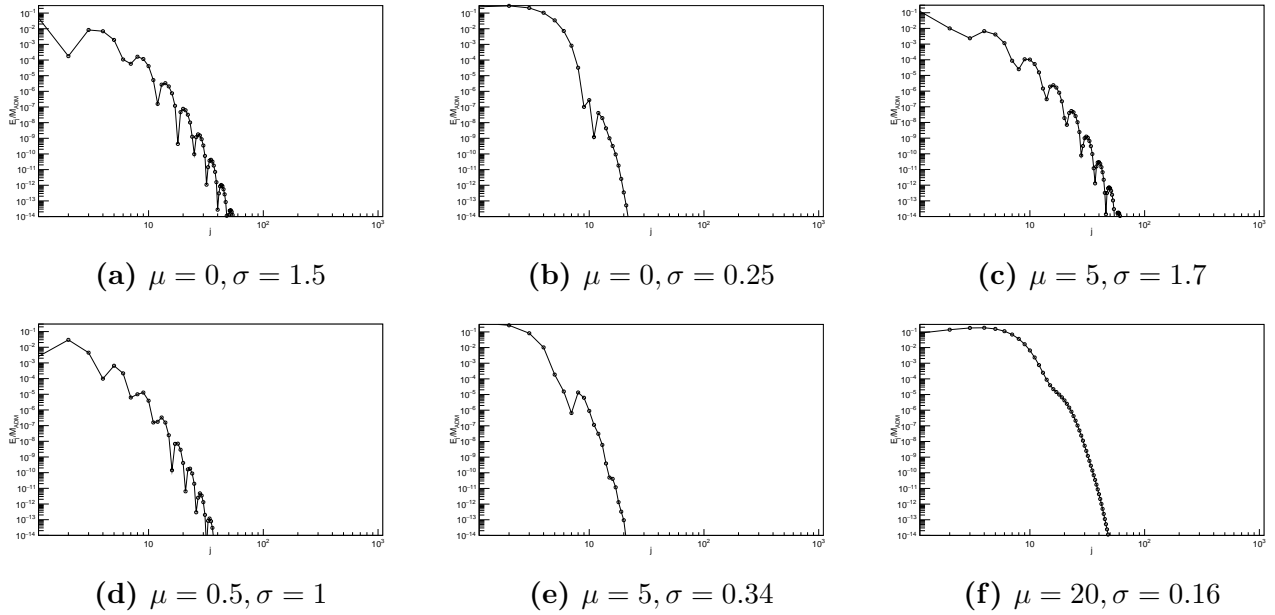


Figure 2.10: Initial ($t = 0$) energy spectra for the indicated evolutions. In order, these represent stable, unstable, metastable, monotonic irregular, non-monotonic irregular, and chaotic irregular initial data.

be stable. To explore how this depends on mass, we find the best fit values of ϵ, σ for the $j = 0$ eigenmode for each mass that we consider (defined by the least-square error from the Gaussian to a discretized eigenmode); this is the “best approximation” Gaussian to the eigenmode. Then we find the energy spectrum of that best-fit Gaussian; these are shown in figure 2.9a. From the figure, it is clear that the $j = 0$ eigenmode is closer to a Gaussian at larger masses. That is, other eigenmodes contribute less to the Gaussian’s spectrum at higher masses (by several orders of magnitude over the range from $\mu = 0$ to 20). Simply put, the shape of the $j = 0$ eigenmode is closer to Gaussian at higher masses, which suggests that the island of stability should be larger at larger scalar field mass. Figure 2.9b compares the $j = 0$ eigenmode and best fit Gaussian for $\mu = 0$ and 20; on inspection, there is more deviation between the eigenmode and Gaussian for the massless scalar.

In addition, the best-fit Gaussian width decreases from $\sigma \sim 0.8$ for a massless scalar as the mass increases. At $\mu = 20$, the best-fit width is $\sigma \sim 0.31$. This suggests that Gaussians that approximate the $j = 0$ mode well enough are narrower in width at higher masses. An interesting point to note is that the island of stability for $\mu = 0, 0.5$ is actually centered at considerably larger widths than the best-fit Gaussian. This may not be surprising, since the best-fit Gaussians at low masses actually receive non-negligible contributions from higher mode numbers; moving away from the best-fit Gaussian can actually reduce the power in higher modes. For example, the stable initial data shown in figure 2.10a below has considerably less power in the $j = 2$ mode.

2.5.2 Spectra of different behaviors

A key question that one might hope to answer is whether the stability class of a given (μ, σ) can be determined easily by direct inspection of the initial data without requiring many evolutions at varying amplitudes. The initial energy spectra for examples of each class, including monotonic,

non-monotonic, and apparently chaotic irregular behaviors, are shown in figure 2.10. These spectra are taken from among the smallest amplitudes we evolved in order to minimize backreaction effects.

Unfortunately, the initial energy spectra do not seem to provide such a method for determining the stability class. Very broadly speaking, stable and metastable (μ, σ) correspond to initial spectra that drop off fairly quickly from the $j = 0$ mode as j increases, while unstable and irregular behaviors tend to have roughly constant or even slightly increasing spectra up to $j = 5$ or 10. However, figure 2.10d shows that some irregular initial data have spectra that decrease rapidly after a small increase from $j = 1$ to $j = 2$. Kinks in the spectrum are more prevalent for widths of the AdS scale or larger, while spectra for smaller widths tend to be smoother.

2.5.3 Evolution of spectra

While the initial spectrum for a given (μ, σ) pair does not have predictive value regarding the future behavior as far as we can tell, the time dependence of the spectrum throughout the evolution of the system is informative. Figure 2.11 shows the time-dependence of spectra for examples of the stable, unstable, metastable, and chaotic irregular classes. In each figure, the lower panel shows the fraction E_j/M_{ADM} in each mode up to $j = 6$, while the upper panel shows the cumulative fraction $\sum_j E_j/M_{ADM}$ to the mode 2^k with $k = 0$ to 5.

The difference between stable evolution in figure 2.11a and unstable evolution in figure 2.11b is readily apparent. As the evolution proceeds, we expect a cascade of energy into higher mode numbers, but inverse cascades to lower modes can also occur. The stable evolution shows a slow pattern of cascades and inverse cascades, in fact. On the other hand, the unstable evolution shows a nearly monotonic cascade of energy into the highest modes along with a simultaneous cascade of energy into the lowest modes (therefore depleting intermediate modes). These are common observations in the literature and are included here for completeness.

The metastable evolution shown in figure 2.11c is interesting in light of the stable and unstable spectra. The amplitude shown is from the “unstable” portion of figure 2.4d, the part consistent with the perturbative scaling $t_H \sim \epsilon^{-2}$. However, the spectrum shows a similar pattern of slow cascades and inverse cascades to the stable initial data example, though on a somewhat faster time scale in this case. While perhaps surprising, this is in keeping with the similarities noted between the initial spectra in figures 2.10a and 2.10c. We have also checked that the time-dependent spectrum at a higher amplitude with $t_H \sim 100$ follows the same pattern as 2.11c; in fact, it looks essentially the same but simply ends at an earlier time. This lends some credence to the idea that metastable initial data is stable at lowest nontrivial order in perturbation theory, with instability triggered by higher-order corrections. Alternately, the instability could be caused by an oscillatory singularity in the perturbative theory, as discussed in [15, 23–25] in the case of two-mode initial data. These divergences do not appear in the energy spectrum.

Figure 2.11d shows the time-dependence of the spectrum in an irregular evolution, specifically $\mu = 20, \sigma = 0.19$ at $\epsilon = 6.95$, which is in the chaotic region of the t_H vs ϵ plot in figure 2.5d. There is rapid energy transfer among modes, including cascades out of and inverse cascades into mode numbers $j \leq 32$ over approximately a light-crossing time. It is easy to imagine that horizon formation might occur at any of the cascades of energy into higher modes, leading to seemingly random jumps in t_H as a function of amplitude.

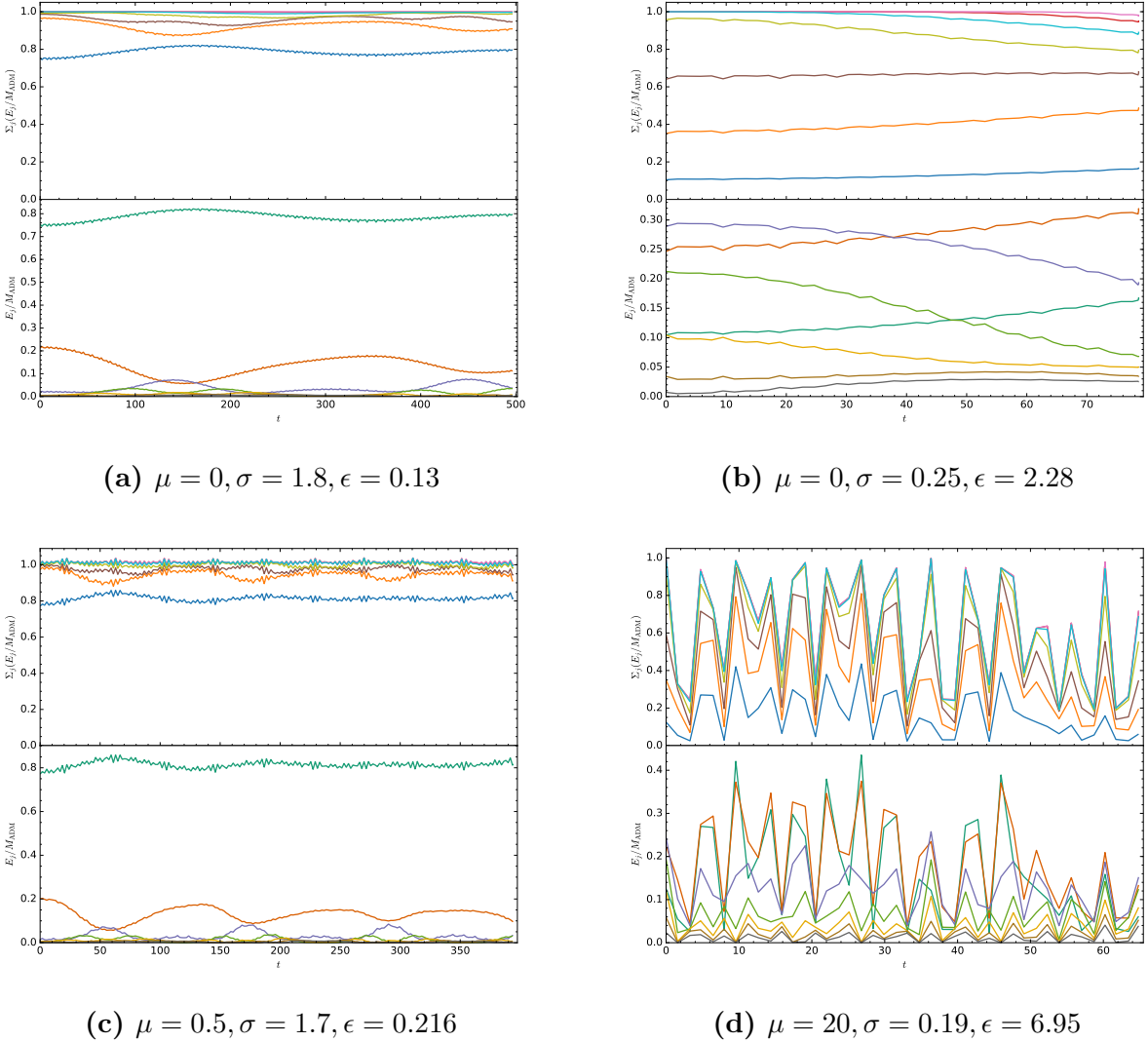


Figure 2.11: The time dependence of the energy spectra as a fraction of the total ADM mass for the indicated μ, σ, ϵ . Lower panels show the lowest 7 modes (in colors cyan, red, purple, green, yellow, brown, and gray respectively). Upper panels show cumulative energy to mode $j = 0, 1, 2, 4, 8, 16, 32$ (in colors blue, orange, brown, yellow, aqua, red, and magenta).

Finally, the time-evolved energy provide another possible measure of approximate thermalization in the dual CFT; namely, the spectrum should approach an (exponentially cut-off) power law at thermalization. In most cases, this occurs shortly before horizon formation, but there are exceptions, such as the late time behavior of initial data below the critical mass for black hole formation in Einstein-Gauss-Bonnet gravity [30]. When there is evidence of chaotic behavior, it is particularly interesting to know if the spectra for similar amplitudes approach a power law at similar times even if horizons form at very different times. Figure 2.12 shows the energy spectra for two amplitudes in the chaotic region of the t_H vs ϵ plot for $\mu = 0, \sigma = 1.1$. Figure 2.12a is the spectrum just before horizon formation for $\epsilon = 1.01$, while figure 2.12b is the spectrum at approximately the same time for $\epsilon = 1.02$, which is very long before horizon formation. In this example, we see that the spectrum does approach a power law for the evolution that is forming a horizon, while the other

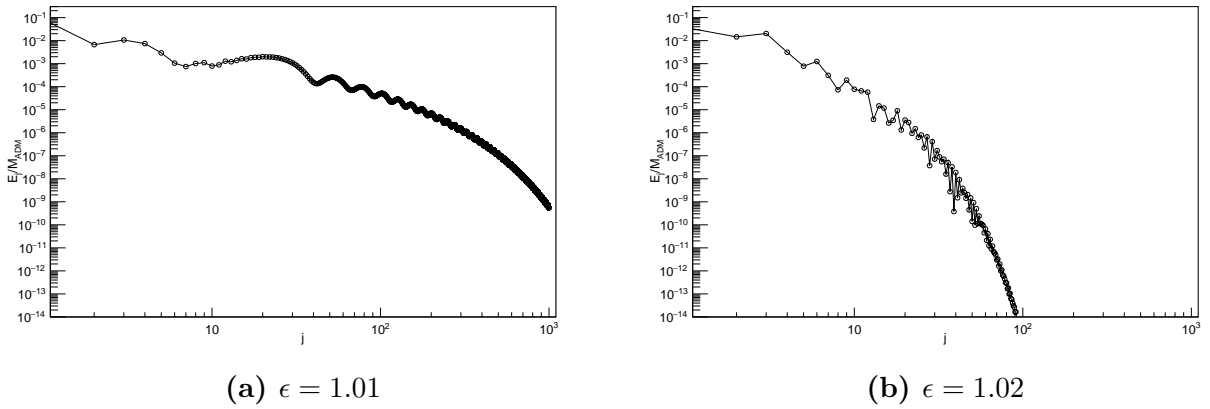


Figure 2.12: Spectra at time $t \approx 71$ for $\mu = 0, \sigma = 1.1$ for the two amplitudes given. $\epsilon = 1.01$ forms a horizon at $t_H \approx 71.1$, $\epsilon = 1.02$ at $t_H \approx 248.0$.

evolution demonstrates a more rapid decay (typically fit by a power law times an exponential in the literature). Therefore, this example suggests that a power law spectrum may yield similar results to horizon formation as a measure of thermalization in the dual CFT.

2.6 Discussion

For the first time, we have presented the phase diagram of stability of AdS_5 against horizon formation, treating the scalar field mass μ and width σ of initial data as free parameters. In addition to mapping the location of the so-called ‘‘island of stability,’’ we have gathered evidence for two non-perturbative classes on the ‘‘shorelines’’ of the island, the metastable and irregular classes. While these must either exhibit stability (no collapse below some critical amplitude) or instability (collapse at arbitrarily small but finite amplitude) as the amplitude $\epsilon \rightarrow 0$, they are distinguished by their behavior at computationally accessible (finite) amplitudes. While perturbatively unstable evolutions obey $t_H \propto \epsilon^{-2}$ as $\epsilon \rightarrow 0$ (and show evidence of this behavior at finite ϵ), metastable initial data follows $t_H \propto \epsilon^{-p}$ for $p > 2$ over a range of amplitudes $\epsilon > 0$. The irregular class is characterized by horizon formation times t_H that are not well described by a power law and sometimes exhibit non-monotonicity or even evidence of chaos. Both of these classes appear across the range of μ values that we study and at both small- and large-width boundaries of the stable class of initial data.

At this time, it is impossible to say whether metastable initial data is stable or unstable as $\epsilon \rightarrow 0$ (or if all metastable data behaves in the same way in that limit). Our numerical evolutions include cases in which the lowest amplitudes jump either to metastable scaling with smaller p or to evolutions that do not collapse over the timescales we study. In many cases, too, the power law $t_H \propto \epsilon^{-p}$ with p some fixed value > 2 is robust as we exclude larger amplitudes from our fit. It is also possible that some metastable initial data is stable in the perturbative theory (ie, to ϵ^3 order in a perturbative expansion) but not at higher orders.

The irregular class seems likely to be (mostly) stable at arbitrarily small amplitudes based on our numerical evolutions, though we have not found a critical amplitude for monotonic irregular initial

data. The irregular initial data includes the “quasi-stable” initial data described in [18, 34], which has a sudden increase then decrease in t_H as ϵ decreases as well as evidence for chaotic behavior. In fact, we have found evidence for weakly chaotic behavior for non-monotonic initial data in the form of a small but nonzero Lyapunov coefficient and in the phase space trajectory. Both non-monotonicity and chaos become stronger and more common at larger scalar masses; however, we have also found evidence of chaotic behavior for the massless scalar including in the t_H vs ϵ curve. To our knowledge, this is the first evidence of chaos in this relationship for spherically symmetric massless scalar collapse in AdS, which is particularly interesting because there is only one physically meaningful ratio of scales, σ as measured in AdS units.

While we have emphasized the appearance of new behaviors outside perturbation theory, metastable and irregular initial data are interesting potential subjects for analysis in the multiscale perturbation theory. A key question is if they demonstrate any unusual behavior there or map directly onto the stable or unstable classes.

Aside from the ultimate stability or instability of metastable and irregular initial data, several questions remain. For one, black holes formed in massive scalar collapse in asymptotically flat spacetime exhibit a mass gap for initial profiles wider than the Compton wavelength $1/\mu$ [43]. Whether this mass gap exists in AdS is not clear, and it may disappear through repeated gravitational focusing as the field oscillates many times across AdS; investigating this type of critical behavior will likely require techniques similar to those of [44]. Returning to our stability phase diagram, the physical mechanism responsible for chaos that seems to occur for some irregular initial data is not yet clear. Is it some generalization of the same mechanism as found in the two-shell system? Also, would an alternate definition of approximate thermalization in the dual CFT, such as development of a power-law spectrum, lead to a different picture of the stability phase diagram? Finally, the big question is whether there is some test that could be performed on initial data alone that would predict in advance its behavior? So far, no test is entirely successful, so new ideas are necessary.

Acknowledgments We would like to thank Brayden Yarish for help submitting jobs for the $\mu = 10$ evolutions. The work of ND is supported in part by a Natural Sciences and Engineering Research Council of Canada PGS-D grant to ND, NSF Grant PHY-1606654 at Cornell University, and by a grant from the Sherman Fairchild Foundation. The work of BC and AF is supported by the Natural Sciences and Engineering Research Council of Canada Discovery Grant program. This research was enabled in part by support provided by WestGrid (www.westgrid.ca) and Compute Canada Calcul Canada (www.computecanada.ca).

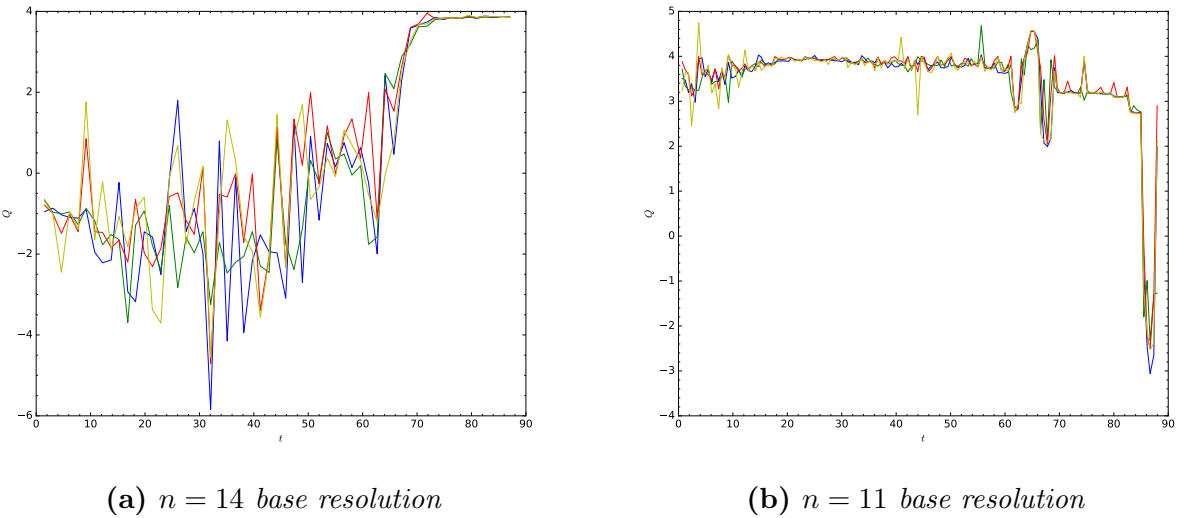


Figure 2.A.1: Convergence results for $\mu = 0.5$, $\sigma = 1$, $\epsilon = 1.12$ showing order of convergence Q vs time for ϕ, M, A, δ (blue, green, red, yellow respectively). Left: Resolutions $n = 14, 15, 16$ used. Right: Resolutions $n = 11, 12, 13$ used.

Appendix

2.A Convergence Testing

Due to the large number of evolutions we have carried out, it is not computationally feasible to test all of them for convergence. Therefore, we have checked several interesting cases of irregular initial data, which are the most curious. These are carried out by evolving the initial data with a base resolution $n = 14$ and again at $n = 15, 16$ with commensurate time steps, as described in [34]. In the cases indicated, we evaluated the order of convergence at lower resolutions. We remind the reader that the order of convergence Q is the base-2 logarithm of the ratio of L^2 errors (root-mean-square over all corresponding grid points) between successive pairs of resolutions. We also note that the initial data is defined analytically, so Q can appear poor at $t = 0$ since the errors are controlled by round off; in some cases, Q is therefore undefined and not plotted.

First, we carried out convergence tests for mass $\mu = 0.5$, width $\sigma = 1$, and amplitude $\epsilon = 1.12$, which is monotonic irregular initial data presented in figure 2.5a. This amplitude collapses with $t_H \sim 88$. Figure 2.A.1a shows the (L^2 norm) order of convergence for the field variable ϕ , the mass function M , and the metric functions A, δ . While the order of convergence is initially poor and even

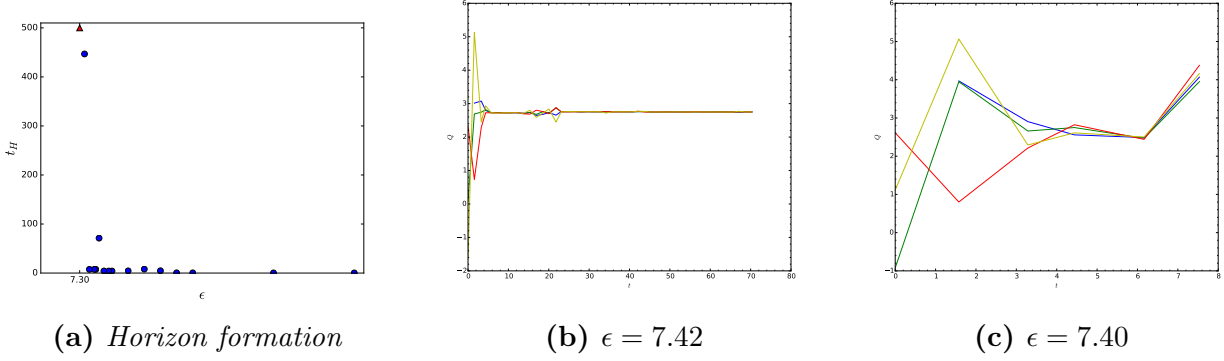


Figure 2.A.2: Convergence results for $\mu = 15$, $\sigma = 0.2$. Left: t_H vs ϵ . Middle & Right: order of convergence vs time for ϕ, M, A, δ (blue, green, red, yellow respectively) for indicated amplitudes.

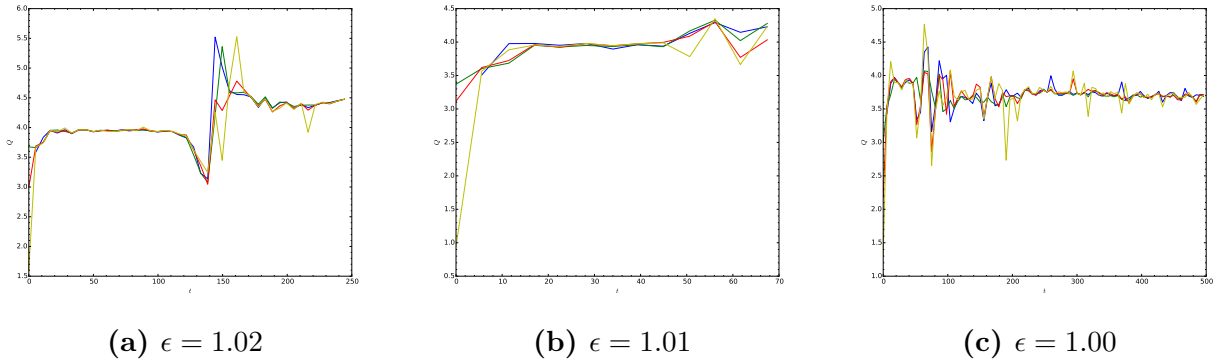


Figure 2.A.3: Convergence results for $\mu = 0$, $\sigma = 1.1$ for listed amplitudes showing order of convergence Q vs time for ϕ, M, A, δ (blue, green, red, yellow respectively); resolutions $n = 12, 13, 14$.

negative, all these variables show approximately fourth order convergence for times $t \gtrsim 70$. The reason for the initially poor convergence is that the error between successive resolutions is already given by (machine limited) round off. As a demonstration, we tested the order of convergence with base resolution $n = 11$, as shown in figure 2.A.1b. The variables show order of convergence $Q \gtrsim 3$ already at this resolution for most of the evolution, losing convergence only for $t > 80$, where we see approximately 4th-order convergence in the $n = 14$ resolution computations.

Two of the authors have discussed the convergence properties of evolution for the nonmonotonic irregular initial data with $\mu = 20, \sigma = 0.1, \epsilon = 11.74$, which is in an amplitude region of increased t_H surrounded by smaller values, in detail in [34]. In short, the variables ϕ, M, A, δ all exhibit fourth order convergence, as does $\Pi^2(t, 0)$, and the conserved mass actually has 6th order convergence.

Initial data for $\mu = 15, \sigma = 0.2$ is also nonmonotonic, as shown in figure 2.A.2a. While we have not analyzed all aspects of the convergence, we see from the remainder of figure 2.A.2 that ϕ, M, A, δ exhibit convergent behavior at better than second order for $\epsilon = 7.42$ (figure 2.A.2b, second-largest value of t_H in figure 2.A.2a) and $\epsilon = 7.40$ (figure 2.A.2c, adjacent amplitude in figure 2.A.2a). It is important to note that the larger amplitude also has the larger horizon formation time, contrary to the usual monotonic behavior. In other words, we have validated the nonmonotonicity of this initial data through convergence testing.

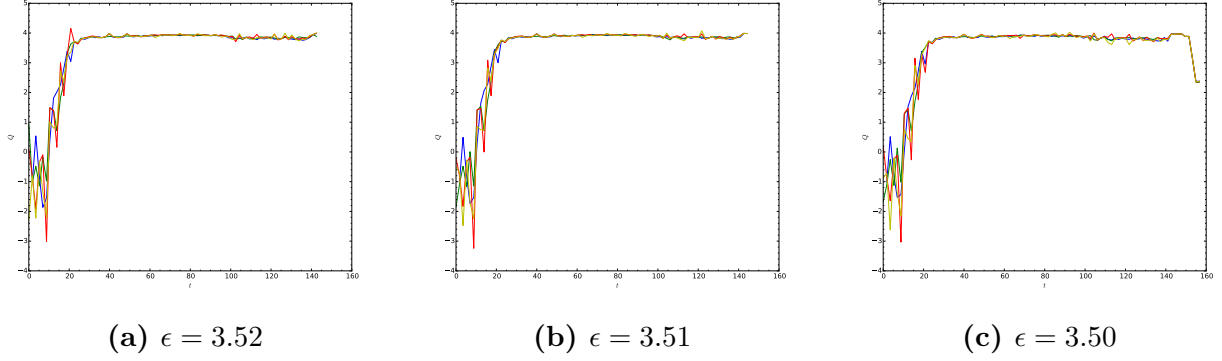


Figure 2.A.4: Convergence results for $\mu = 5$, $\sigma = 0.34$ for listed amplitudes showing order of convergence Q vs time for ϕ, M, A, δ (blue, green, red, yellow respectively); resolutions $n = 14, 15, 16$.

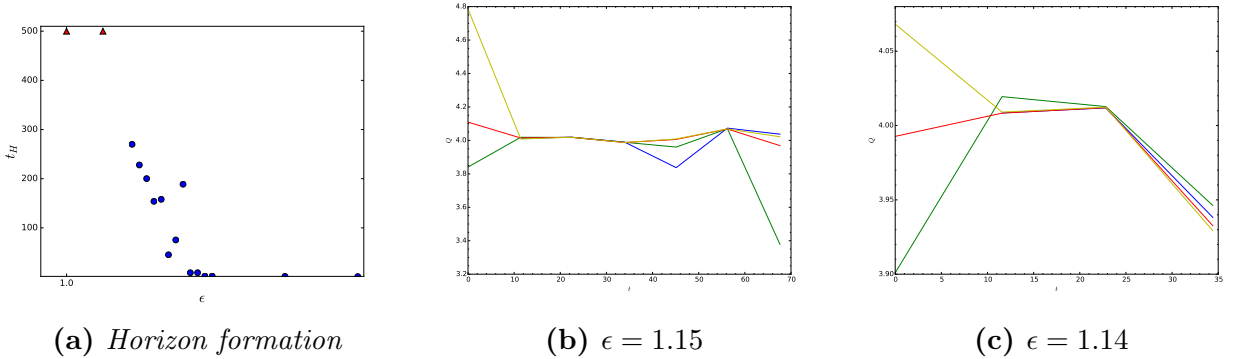


Figure 2.A.5: Convergence results for $\mu = 1$, $\sigma = 1$. Left: t_H vs ϵ . Middle & Right: order of convergence Q vs time for ϕ, M, A, δ (blue, green, red, yellow respectively); resolutions $n = 11, 12, 13$.

It is most crucial to validate the convergence of chaotic evolutions. In table 2.2, we noted that the Ricci scalar at the origin has nonzero Lyapunov exponent at almost the 2 sigma level for amplitudes $\epsilon = 1.02, 1.01, 1.00$ for $\mu = 0, \sigma = 1.1$. We show the results of convergence tests for these amplitudes in figure 2.A.3; because these are longer evolutions, we consider the convergence at the lower resolutions $n = 12, 13, 14$. After a transient start-up period, these are all convergent with $Q > 2.5$ for all variables considered at all times; for most of the time, the order of convergence is $Q > 3.5$. It is worth noting that one of the amplitudes does not form a horizon through $t = 500$. These convergence tests validate both the nonmonotonic nature of the evolution ($t_H \approx 248, 71$ and > 500 for $\epsilon = 1.02, 1.01, 1.00$ respectively) and also the calculation of the Lyapunov coefficient.

Also in table 2.2, we found a nonzero Lyapunov exponent for $\mu = 5, \sigma = 0.34$ at amplitudes $\epsilon = 3.52, 3.51, 3.50$. The results of convergence tests for these amplitudes appear in figure 2.A.4. For $t \gtrsim 20$, these evolutions exhibit convergent behavior with $Q > 3.5$ (and always $Q > 2$). At early times, the apparent poor convergence is again due to the errors being dominated by round-off; we have carried out additional convergence tests (not shown) and verified that these evolutions are already convergent with order of convergence close to $Q = 4$ at base resolutions $n = 12$ for $t \lesssim 20$. Again, convergence tests validate chaotic behavior for these initial data.

Initial data with $\mu = 1, \sigma = 1$ is chaotic over a narrow range of amplitudes. We have carried out

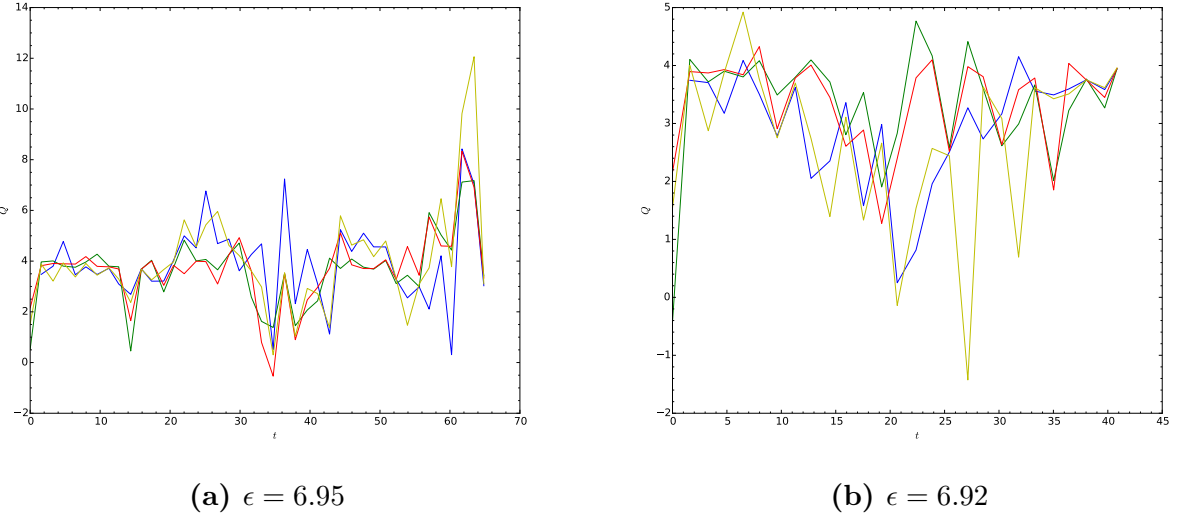


Figure 2.A.6: Order of convergence vs time for ϕ, M, A, δ (blue, green, red, yellow) for $\mu = 20, \sigma = 0.19$ and indicated amplitudes.

convergence testing for amplitudes $\epsilon = 1.15, 1.14$, which are the two amplitudes with $t_H < 100$ between amplitudes with $t_H \gtrsim 150$ in figure 2.A.5a. The order of convergence was poor for these amplitudes in our initial tests with base resolution $n = 14$ because the error between resolutions was dominated by round-off, similar to the convergence tests we discussed above for $\mu = 0.5, \sigma = 1$. In subsequent tests with lower resolutions $n = 11, 12, 13$, we find an order of convergence $Q \sim 4$ for most of the evolutions (and always $Q > 3$). It is important to note again that our evolutions exhibit convergence while showing horizon formation at a later time for a larger amplitude in this case, again validating the nonmonotonic behavior.

Finally, we ran convergence tests for the chaotic initial data with $\mu = 20, \sigma = 0.19$ for $\epsilon = 6.95, 6.92$, with $t_H \approx 65.5, 40.8$ respectively. As shown in figure 2.A.6, the simulations are close to fourth order convergence for most of the evolution, but there are periods where the order of convergence for evolution and constraint variables becomes negative. This of course leads to the concern that the evolutions should have collapsed during those periods and extend into an “afterlife” evolution. We have therefore evolved these amplitudes through these regions (approximately $t = 30 - 40$ for $\epsilon = 6.95$ and $t = 18 - 30$ for $\epsilon = 6.92$) at high resolution ($n = 18$). If the evolutions are truly in an afterlife, this higher resolution calculation may include horizon formation. We do not observe this. Another tell-tale of would-be horizon formation is a decrease in the timestep size by an order of magnitude or more followed by an increase. We monitor the timestep size every 500 time steps through this evolution but do not observe a decrease in timestep size by more than a factor of 2. As a result, we believe the values of t_H found are reliable, though the reader may wish to consider them with some caution. In other words, while convergence testing is the gold standard to validate our numerical evolutions, there are other indicators of reliability, which these evolutions satisfy. It is also worth noting that the rapid energy transfer characteristic of figure 2.11d for $\epsilon = 6.95$ begins immediately and is therefore seen in a convergent region of the evolutions, particularly for $t \lesssim 14$.

Nonetheless, we emphasize that we have found convergent evolutions for irregular initial data at scalar masses from $\mu = 0$ to 20. It is important to note that we have validated nonmonotonic

behavior in plots of t_H vs ϵ . Convergence testing also specifically validates the evolutions used to find a nonzero Lyapunov coefficient (at nearly the 2σ level) for massless scalar collapse.

3 Perturbative Stability of Massless Scalars in AdS₄

Will be published to the arXiv, then submitted to JHEP

3.1 Contributions

What my contributions were

Paper Title

To Appear on arxiv.org

Brad Cownden¹, Nils Deppe², and Andrew R. Frey^{3,4}

¹*Department of Physics & Astronomy,
University of Manitoba
Winnipeg, Manitoba R3T 2N2, Canada
cowndenb@myumanitoba.ca*

²*Cornell Center for Astrophysics and Planetary Science and Department of Physics,
Cornell University
122 Sciences Drive, Ithaca, New York 14853, USA
nd357@cornell.edu*

³*Department of Physics & Astronomy,
University of Manitoba
Winnipeg, Manitoba R3T 2N2, Canada*

⁴*Department of Physics and Winnipeg Institute for Theoretical Physics,
University of Winnipeg
515 Portage Avenue, Winnipeg, Manitoba R3B 2E9, Canada
a.frey@uwinnipeg.ca*

We construct a family of perturbative solutions for massless scalar fields in AdS_4 using the *Two-Time Formalism* (TTF) to high eigenmode numbers. We furthermore investigate the validity of *quasi-periodic* (QP) solutions with high j_{\max} values and examine their stability to perturbations. Finally, check that TTF and QP solutions continue to satisfy the Einstein equation at times greater than $t \sim \epsilon^{-2}$ and compare these results to the full numerical solutions at low amplitude.

3.2 Introduction

The question of the nonperturbative stability of AdS_{d+1} has been examined extensively, both as a question of mathematical physics and given its application to the AdS/CFT correspondence; see [45] for a recent review. Beginning with the seminal work of [1], many works [2–4, 46, 47] have demonstrated the generic instability of AdS_{d+1} gravity minimally coupled to a scalar field in a variety of dimensions. The primary driver of the instability in the fully nonlinear system is the weakly turbulent flow of energy to short length scales; in the perturbative description, secular growth of resonant terms with high frequencies triggers the collapse [5, 28, 48]. However, [19, 49, 50] (and others) have shown that some initial conditions in asymptotically AdS spacetime resist gravitational collapse and therefore form islands of stability in the space of initial data. The stable solutions within the island are variously known as oscillons or breathers for real scalars [1, 46, 49, 51], boson stars for complex scalars [18, 19], and geons for pure gravity [5, 52].¹ [34, 53, 54] have shown that

¹citations given for studies in asymptotically AdS space.

the classification of initial data is more complex nonperturbatively, intriguingly finding evidence of chaos at the boundary between stable and unstable initial data. While past studies have mostly dealt with spherically symmetric collapse, an increasing amount of work is focused on removing this restriction [55–57].

While the nonperturbative physics of AdS instability requires numerical study, a perturbative formulation should give insight into stability at low amplitudes. In a naive perturbation theory, the fully resonant spectrum of eigenmodes of pure AdS leads to secular growth; this can be removed order by order by frequency shifts if the initial data consists of a single eigenmode but not for superpositions of eigenmodes [5]. If instead the amplitude and phase of each eigenmode are allowed to flow slowly, resummation of the perturbation theory leads to a ladder of coupled first-order ordinary differential equations describing the flow. There are several equivalent methods to arrive at the flow equations: a “two-time formalism” (similar to a temporal gradient expansion for the amplitude and phase variables) [6], a renormalization-like formalism [7, 11], time averaging [11, 17], and keeping only resonant source terms [23]. (We will commonly refer to the perturbative theory as the TTF theory, for two-time formalism.) A key feature of this perturbative theory is a scaling symmetry $\phi(t) \rightarrow \epsilon^{-1}\phi(\epsilon^2 t)$, so it is possible to divide out the amplitude of the scalar and describe the solution in terms of the “slow time” $\tau = \epsilon^2 t$. Furthermore, the perturbative theory has conserved quantities beyond the total energy E , including a “particle number” N , which leads to inverse cascades in energy from higher eigenmodes to lower modes along with the expected direct cascades from low to high. On the other hand, while the flow equations are significantly less computationally intensive than the full Einstein and Klein-Gordon equations, finding a solution requires truncating to a maximum eigenmode number j_{max} .

At a given mode truncation j_{max} , the TTF theory has stable quasi-periodic (QP) solutions with constant energy spectrum as described in [6, 14], and other stable solutions orbit the QP solutions in phase space. Since the amplitude scales out of the TTF, the QP solutions are described by “temperature” $T = E/N$; for fixed maximum mode number j_{max} , the maximum possible temperature is $d + 2j_{max}$. The QP solutions are special in that the time-dependence of each mode is harmonic, so QP solutions satisfy algebraic equations; [14] found low-temperature solutions to these equations directly. To reach higher temperatures, [14] perturbed low-temperature solutions by the addition of energy. Our main concern in this work is the persistence of QP solutions, especially those at high temperatures, as j_{max} increases since the full TTF theory takes $j_{max} \rightarrow \infty$.

**** LEFT THE REST ALONE, NEED TO DISCUSS ORGANIZATION AND METHODS WHEN WE'RE FINISHED

We show that high temperature QP solutions are very sensitive to truncation error and cannot be interpreted as physically relevant solutions. We then examine the time evolution of large j_{max} QP solutions at all temperatures in both the perturbative theory and the full, nonlinear theory.
[OTHER MAJOR GOALS HERE]

This work is organized as follows: we begin in § 3.3 with a review of the linearized solutions for a minimally coupled, massless scalar field in AdS_{d+1} and establish the renormalization flow equations that govern the time evolution of the amplitude and phase functions in the scalar field. In § 3.4, we find quasi-periodic solutions in AdS_4 by directly solving a set of algebraic equations, and discuss the viability of reaching new QP solutions through repeated application of a perturbative scheme. We then examine the time evolution of a wide range of QP solutions in § 3.5 in both the linearized

theory and the full, nonlinear system. We end with a discussion in § 4.6.

3.3 Minimally Coupled Scalar Fields in AdS_{d+1}

Consider a spherically-symmetric, asymptotically AdS_{d+1} spacetime with characteristic curvature ℓ . Written in Schwarzschild-like coordinates, the metric in units of AdS scale is given by

$$ds^2 = \frac{1}{\cos^2(x)} (-Ae^{-2\delta}dt^2 + A^{-1}dx^2 + \sin^2(x)d\Omega^{d-1}), \quad (3.1)$$

where the radius $x \in [0, \pi/2]$ and $-\infty < t < \infty$. A minimally-coupled, massless scalar field $\phi(t, x)$ is subject to the following Einstein and Klein-Gordon equations:

$$G_{ab} + \Lambda g_{ab} = 8\pi \left(\nabla_a \phi \nabla_b \phi - \frac{1}{2} g_{ab} (\nabla \phi)^2 \right) \quad (3.2)$$

$$0 = \frac{1}{\sqrt{-g}} \partial_a \sqrt{-g} g^{ab} \partial_b \phi. \quad (3.3)$$

The canonical equations of motion for the scalar field are

$$\partial_t \phi = Ae^{-\delta}\Pi, \quad \partial_t \Phi = \partial_x(Ae^{-\delta}\Pi), \quad \text{and} \quad \partial_t \Pi = \frac{\partial_x(\Phi A e^{-\delta} \tan^{d-1}(x))}{\tan^{d-1}(x)}, \quad (3.4)$$

where the canonical momentum is $\Pi(t, x) = A^{-1}e^\delta \phi$ and $\Phi(t, x) \equiv \partial_x \phi$ is an auxiliary variable. In terms of these fields, (3.2)-(3.3) reduce to

$$\partial_x \delta = -(\Pi^2 + \Phi^2) \sin(x) \cos(x), \quad (3.5)$$

$$\partial_x A = \frac{d-2+2\sin^2(x)}{\sin(x) \cos(x)} (1-A) - A \sin(x) \cos(x) (\Pi^2 + \Phi^2). \quad (3.6)$$

3.3.1 Linearized Solutions

The linearized scalar field solutions come from expanding in terms of a small amplitude

$$\phi(t, x) = \sum_{j=0}^{\infty} \epsilon^{2j+1} \phi_{2j+1}(t, x), \quad A(t, x) = 1 - \sum_{j=1}^{\infty} \epsilon^{2j} A_{2j}(t, x), \quad \delta(t, x) = \sum_{j=1}^{\infty} \epsilon^{2j} \delta_{2j}(t, x). \quad (3.7)$$

Under this expansion, the $\mathcal{O}(\epsilon)$ terms give the linearized equation of motion for the scalar field:

$$\partial_t^2 \phi_1 + \hat{L} \phi_1 = 0 \quad \text{where} \quad \hat{L}_1 \equiv -\frac{1}{\tan^{d-1}(x)} \partial_x (\tan^{d-1}(x) \partial_x). \quad (3.8)$$

The eigenvalues of \hat{L} are simply $\omega_j^2 = (d+2j)^2$ and the eigenfunctions are

$$e_j(x) = k_j \cos^d(x) P_j^{(\frac{d}{2}-1, \frac{d}{2})}(\cos(2x)) \quad \text{with} \quad k_j = \frac{2\sqrt{j!(j+d-1)!}}{\Gamma(j+\frac{d}{2})}. \quad (3.9)$$

Note the the normalizations are chosen such that $\hat{L}e_j = \omega_j^2 e_j$ and

$$\langle e_i | e_j \rangle \equiv \int_0^{\frac{\pi}{2}} dx \bar{e}_i e_j \tan^{d-1}(x). \quad (3.10)$$

By expanding the scalar field functions in terms of the eigenbasis given in (3.9) and substituting into (3.8), we find that the time-dependent functions $c_n^{(2j+1)}(t) = \langle \phi_{2j+1}(t, x), e_n(x) \rangle$ satisfy $\ddot{c}_j^{(1)} + \omega_j^2 c_j^{(1)} = 0$. The general solution for the scalar field is can then be written in terms of time-dependent amplitude and phase variables:

$$\phi_1(t, x) = \sum_{j=0}^{\infty} A_j(t) \cos(\omega_j t + B_j(t)) e_j(x). \quad (3.11)$$

As discussed in [7, 11, 15], the integer nature of the mode frequencies mean that the spectrum is fully resonant. Unlike solutions such as oscillons, the resonant terms cannot be absorbed by a frequency shift and therefore result in *secular* terms: resonant contributions that grow rapidly with time and induce collapse. These resonant terms appear at $\mathcal{O}(\epsilon^3)$ and can be expressed in terms of a source, $S(t)$:

$$\ddot{\phi}_3 + \hat{L}\phi_3 = S \equiv 2(A_2 - \delta_2)\ddot{\phi}_1 + (\dot{A}_2 - \dot{\delta}_2)\dot{\phi}_1 + (A'_2 - \delta'_2)\phi'_1, \quad (3.12)$$

where A_2, δ_2 are the leading-order contributions to the metric functions in (3.7) that are determined by the $\mathcal{O}(\epsilon^2)$ backreaction with the metric. Projecting onto the $e_j(x)$ basis, the source term (*i.e.*, resonant contributions) can be expressed in terms of the time-dependent coefficients

$$\ddot{c}_j^{(3)} + \omega_j^2 c_j^{(3)} = S_j. \quad (3.13)$$

To control the growth of secular terms, [11] used resummation techniques to absorb singular contributions into the amplitude A_j and phase B_j of (3.11). This also resulted in a set of conserved quantities: the energy of the system, E , and particle number, N . The simultaneous conservation of both E and N implied that weakly turbulent systems exhibit dual cascades of energy, providing a mechanism through which two-mode data could remain stable [10].

3.3.2 Two-Time Formalism

The Two-Time Formalism (TTF) describes the solution to (3.8) in terms of slowly-modulating amplitude and phase variables, A_j and B_j , that are functions of the slow time $\tau = \epsilon^2 t$,

$$\phi(t, x) = \epsilon \sum_{j=0}^{\infty} A_j(\epsilon^2 t) \cos(\omega_j t + B_j(\epsilon^2 t)) e_j(x). \quad (3.14)$$

The next non-trivial order in the equations of motion include gravitational self-interactions of the scalar field, and provides source terms for A_j and B_j . Following the time-averaging procedure of [7]

– and using the resonance condition $\omega_i + \omega_j = \omega_k + \omega_l$ to eliminate one of the indices – the l^{th} amplitude and phase are given by

$$-\frac{2\omega_l}{\epsilon^2} \frac{dA_l}{dt} = \sum_{i \neq l} \sum_{j \neq l}^{l \leq i+j} S_{ij(i+j-l)l} A_i A_j A_{i+j-l} \sin(B_l + B_{i+j-l} - B_i - B_j), \quad (3.15)$$

$$\begin{aligned} -\frac{2\omega_l A_l}{\epsilon^2} \frac{dB_l}{dt} &= T_l A_l^3 + \sum_{i \neq l} R_{il} A_i^2 A_l \\ &+ \sum_{i \neq l} \sum_{j \neq l}^{l \leq i+j} S_{ij(i+j-l)l} A_i A_j A_{i+j-l} \cos(B_l + B_{i+j-l} - B_i - B_j). \end{aligned} \quad (3.16)$$

The coefficients T, R, S are calculated directly from integrals over the product of eigenmodes and contain some useful symmetry properties: the integrals vanish except with the resonance condition $\omega_i + \omega_j = \omega_l$ is met.

Computationally, we find it more convenient to write T, R, S in terms of auxiliary coefficients with greater symmetry properties (as shown in [15]). The explicit expressions for these integrals in the interior gauge, in which $\delta(t, x = 0) = 0$, are given in appendix 3.B.

Using a complex amplitude of the form $\mathcal{A}_j(\tau) = A_j \exp(-iB_j)$ in (3.14) allows us to combine equations (3.15) and (3.16) into a single TTF equation:

$$-2i\omega_l \frac{\mathcal{A}_l}{d\tau} = T_l |\mathcal{A}_l|^2 \mathcal{A}_l + \sum_{i \neq l} R_{il} |\mathcal{A}_i|^2 \mathcal{A}_l + \sum_{i \neq l} \sum_{j \neq l}^{l \leq i+j} S_{ij(i+j-l)l} \mathcal{A}_i \mathcal{A}_j \bar{\mathcal{A}}_{i+j-l}. \quad (3.17)$$

3.4 Quasi-periodic Solutions in AdS₄

The stability of the solutions to (3.17) can be examined using a *quasi-periodic* (QP) ansatz for the complex amplitude,

$$\mathcal{A}_j = \alpha_j e^{i\beta_j \tau}, \quad (3.18)$$

where $\alpha_j, \beta_j \in \mathbb{R}$. Substituting (3.18) into (3.14) allows us to relate the QP modes α_j and β_j to the amplitude/phase modes via $A_j = 2\alpha_j$, $B_j = \beta_j \tau$. When we examine how well the QP solutions solve the Einstein equations, we use this conversion to re-construct the scalar and metric fields from the QP solutions. The time dependence in (3.17) is removed via the condition $\beta_j = \beta_0 + j(\beta_1 - \beta_0)$, leaving β_0 and β_1 as unknown parameters. Considering modes of (3.14) up to some j_{max} , the QP ansatz results in a set of $j_{max} + 1$ algebraic equations for $j_{max} + 3$ unknowns

$$2\omega_l \alpha_l \beta_l = T_l \alpha_l^3 + \sum_{i \neq l} R_{il} \alpha_i^2 \alpha_l + \sum_{i \neq l} \sum_{j \neq l}^{l \leq i+j} S_{ij(i+j-l)l} \alpha_i \alpha_j \alpha_{i+j-l}. \quad (3.19)$$

As shown in [14, 17], the TTF is invariant under a $U(1)$ transformation that leads to the conserved quantities

$$E = 4 \sum_j \omega_j^2 \alpha_j^2 \quad \text{and} \quad N = 4 \sum_j \omega_j \alpha_j^2. \quad (3.20)$$

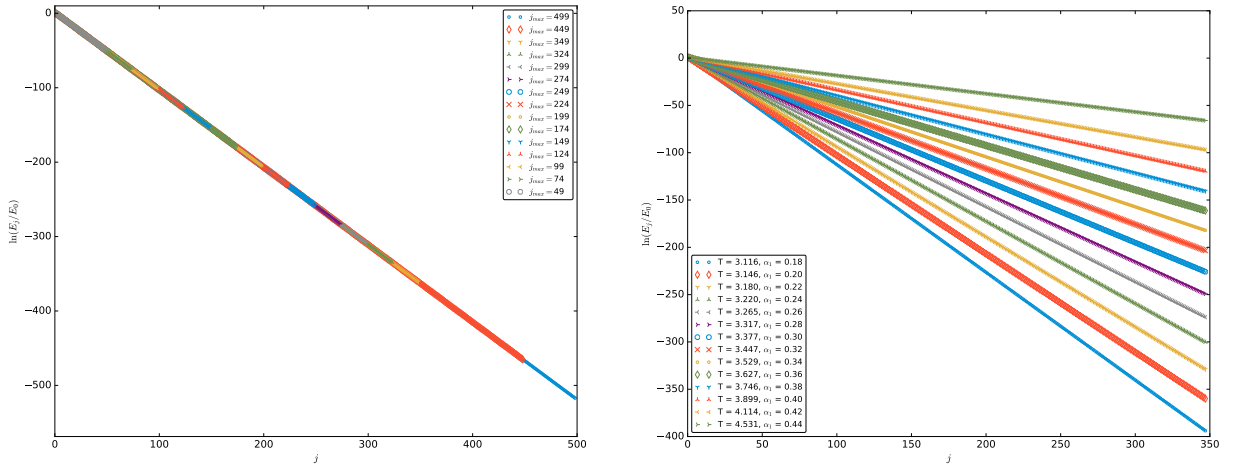
These definitions allow for two of the free parameters to be fixed. Families of solutions can be examined by fixing $\alpha_0 = 1$ and sampling a range of α_1 values in the range $\alpha_1 \ll \alpha_0$. The families of solutions can be distinguished by their “temperature”, or energy per particle number $T = E/N$.

Practically speaking, finding solutions to the j_{max} equations that arise from (3.17) requires truncating the series at a finite value $j_{max} < \infty$. These solutions must continue to be present and unaffected by increasing j_{max} to represent true solutions to the perturbative system.

3.4.1 Persistence at Large j_{max}

The question of edge effects in determining the stability of a particular solution is important to investigate. For instance, if a particular solution to (3.19) is found for some α_1 when $j_{max} = 50$, does this continue to be a solution when we consider more modes, say $j_{max} = 250$? By following the methods outlined in appendix 3.A, we are able to start with a low j_{max} solution and incrementally increase the number of modes being considered up to several hundred. This method was found to be more successful, given the optimization algorithms being used, than other seeding methods.

As an example, consider solutions to (3.19) with the conditions $\alpha_0 = 1.0$ (since all QP solutions are defined up to an overall scale, $\alpha_0 = 1.0$ is taken to always be true) and $\alpha_1 = 0.2$, which corresponds to an initial temperature of $T_0 \simeq 3.146$. In figure 3.1a, we present an overlay of QP solutions generated by successive solving, fitting, and seeding from $j_{max} = 50$ to $j_{max} = 500$ for two families of QP solutions. Similar high j_{max} solutions were confirmed for $\alpha_1 \leq 0.442$.



(a) An overlay of QP solutions with $\alpha_1 = 0.2$, corresponding to $T_0 \simeq 3.146$. (b) QP solutions up to $j_{max} = 350$.

Figure 3.1: Energy spectra for various QP solutions.

When examining the range of α_1 values that result in QP solutions existing, it was found that any solution that existed at small j_{max} could be extended to large j_{max} with proper seeding and sufficient computing power. However, a hard limit exists at the maximum α_1 value of $\alpha_1 = 0.442$, corresponding to a temperature of $T \simeq 4.643$. Above this limit, no QP solutions can be found even for j_{max} values as low as $j_{max} = 50$. There seem to be no solutions that exist at low j_{max} that cease

to exist at high j_{max} . Furthermore, there is no corresponding lower limit to α_1 values; as $\alpha_1 \rightarrow 0$ with $\alpha_j > \alpha_{j+1}$, the TTF solution approaches the well-known single-mode solution.

3.4.2 High Temperature Perturbations

In [14], additional QP solutions can be found by repeatedly perturbing existing solutions. The addition of some energy δE corresponds to the changes $\alpha_j \rightarrow \alpha_j + u_j$ and $\beta_j \rightarrow \beta_j + \theta_1 + \omega_j \theta_2$. The perturbed quantities are given by the system of *linear* equations

$$\delta E = 4 \sum_j \omega_j^2 \alpha_j u_j \quad (3.21)$$

$$\delta N = 4 \sum_j \omega_j \alpha_j u_j = 0 \quad (3.22)$$

$$0 = \omega_l (\alpha_l (\theta_1 + \omega_l \theta_2) + \beta_l u_l) + 6T_l \alpha_l^2 u_l + 2 \sum_{i \neq l} R_{il} (\alpha_i^2 u_l + 2\alpha_i \alpha_l u_l) \\ + 2 \sum_{i \neq l} \sum_{j \neq l}^{l \leq i+j} S_{ij(i+j-l)l} [u_i \alpha_j \alpha_{i+j-l} + u_j \alpha_i \alpha_{i+j-l} + \alpha_i \alpha_j u_{i+j-l}] . \quad (3.23)$$

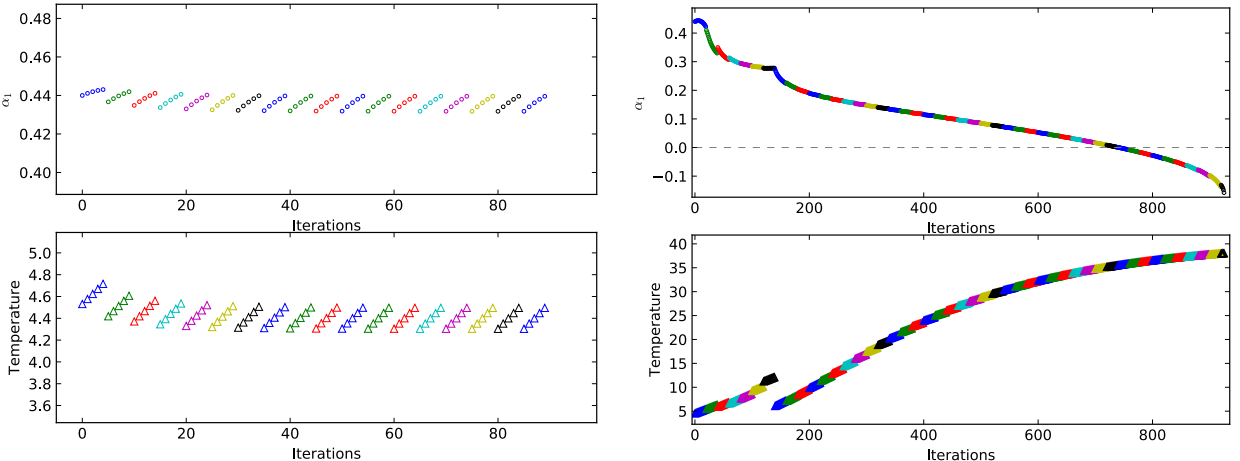
Therefore, by solving (3.21)-(3.23) for $\{u_j, \theta_1, \theta_2\}$, the existing QP solution can be updated and the process can be repeated.

For a standard QP solution with $\alpha_1 = 0.2$, the initial temperature is $T_0 = 3.146$. By applying the high temperature perturbation method described above, we are able to increase the temperature of the solution. However, this process must be examined with some scrutiny; applying repeated perturbations to a known solution does not guarantee the final result remains a valid solution. To investigate this further, we have implemented a solver that projects back down to the QP solution plane after either a set number of perturbations, or after every perturbation. When a solution can no longer be projected back to the QP plane, we have perturbed too far and the state no longer represents a quasi-periodic TTF solution.

Consider figure 3.2. When the result of the linear perturbations is projected back down to the QP plane every 5 iterations, we see that the solution approaches an attractor and is unable to accumulate enough energy to escape this local minimum before being projected back down to the QP plane. However, when the projection frequency is decreased to every 20 iterations, the attractor solution is able to be bypassed; note that as the iteration number increases, we actually see a *decrease* in α_1 value while the temperature continues to increase. At iteration 150 in figure 3.2b, there is a cusp in α_1 and a corresponding drop in temperature. Moreover, α_1 becomes negative after several hundred iterations.

Let us examine the energy spectra of the solutions shown in figure 3.3a. When projecting back to the QP plane every 5 perturbations, the energy spectra do not deviate far from the initial solution; however, no temperature increase is observed. We denote solutions found by this method as “threshold temperature” solutions. The threshold temperature T_{th} is robust against increases in j_{max} and therefore is independent of edge effects. See table 3.1 for further details.

When the projection frequency is decreased to 20 iterations an increase in temperature can be observed, as seen in figure 3.3b. However, the discontinuous behaviour of the temperature as a



(a) The result of applying repeated iterations of the linear perturbations to the initial QP solution of $\alpha_1 = 0.44$, projecting back to the QP plane every five iterations. The perturbation amount (δE in (3.21)) is fixed to 1% of the initial energy.

(b) Starting from the same $\alpha_1 = 0.44$ QP solution, linear perturbations are again applied, this time projecting back to the QP plane every 20 iterations.

Figure 3.2: The results of projecting a $j_{max} = 50$, $\alpha_1 = 0.44$ solution back to the QP plane at various frequencies during high temperature perturbations. Colour changes indicate that the non-linear solver has been applied.

function of iteration is a signal of the energy spectrum loosing its smooth profile (c.f. spectra of iterations 120 and 180). This in itself is not necessarily a breakdown of the quasi-periodic nature of the solution. Upon examining the condition number of the matrix formed by (3.21)-(3.23), we find that in fact the problem becomes ill-conditioned. This results in a absolute value of u_i that is greater than α_i ; that is, the perturbative condition required to derive the system of linear equations (3.21)-(3.23) breaks down. For many prospective high-temperature solutions, this break-down of the perturbative condition is signalled by the development of spikes in the energy spectra caused by the values of α_j becoming negative. In § 3.5.2.1 we will examine the effects of using such solutions as initial data in the evolution of the QP solution.

3.4.3 Building High-Temperature Solutions

Despite high-temperature solutions being inaccessible via repeated energy perturbations, we may ask if such solutions can be found by using different methods. First, we consider perturbing a known QP solution to a high temperature *without* regular projections back to the QP plane. Then, at some sufficiently high temperature T_{max} , we attempt to project back to the QP plane. In figure 3.4a, the spectra of QP solutions before and after projection are shown for increasing j_{max} . For solutions with $j_{max} \geq 100$, high-temperature solutions are in fact projected to low-temperature solutions that may contain negative α_j values. Low- j_{max} solutions, however, appear to remain at high-temperatures after projecting back to the plane. We use this type of solution in our next method.

Starting with a low- j_{max} , high-temperature solution, we can use a fitting procedure similar to that

j_{max}	T_{th}	Iterations
50	4.30344575697724e+00	350
75	4.30344544264076e+00	210
100	4.30344544023857e+00	540
150	4.30344544024198e+00	280
200	4.30344544023915e+00	300

Table 3.1: Values of the threshold temperature T_{th} for QP solutions with given j_{max} . Also included is the number of iterations applied (projecting back to the solution plane after every five iterations).

used to find high- j_{max} , quasi-periodic solutions in §3.4.1. Instead of fitting α_j values away from the highest modes, we instead apply the tail fitting the final 5 modes and use the fit to generate seed values for a $j_{max} + 5$ solution. We see in figure 3.4b that this method results in spectra where energy becomes increasingly concentrated in high- j modes. In fact, for solutions with $j_{max} \geq 90$, and equal or greater amount of energy resides in the high- j modes than in the zero-mode. Intuitively, such a solution would collapse very quickly in the full system due to the high concentration of energy on small length scales. However, because we have arrived at this solution through the two-time formalism, evolution using (3.15)-(3.16) would ensure the solutions remain stable. To help quantify the stability of QP solutions against collapse, we calculate the scalar curvature at the origin.

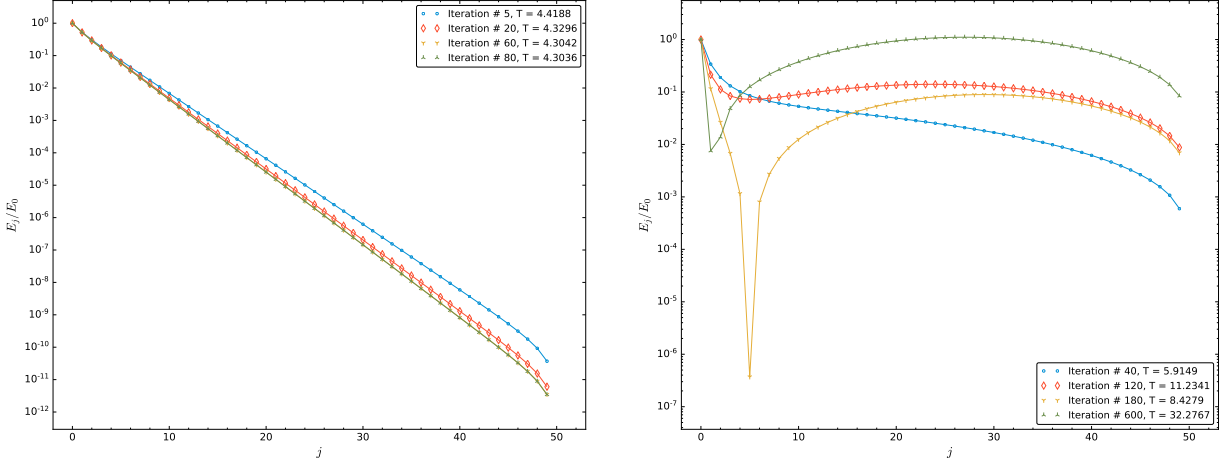
3.4.4 Stability of QP Solutions

3.4.4.1 The Ricci Scalar at the Origin

While the TTF theory itself is stable by construction, we can examine the behaviour of the Ricci scalar at the origin for indications that collapse might occur in the full, nonlinear system. Large values or rapid increases in the Ricci curvature at the origin often indicates impending collapse ([ref?](#)) in numerical simulations. Therefore, we use increases in scalar curvature as a potential indication of collapse. In figure 3.5, we show the highly oscillatory behaviour of the Ricci scalar corresponding to the $T \simeq 66.6$ high-temperature solution presented in figure 3.4b. Note that the upper envelope of Π^2 is $\mathcal{O}(10^{12})$ immediately; this suggests that the high-temperature solution is *not stable* against collapse, even on perturbative timescales. Conversely, the constant behaviour and maximum amplitude $\mathcal{O}(10^4)$ of Π^2 for the $T \simeq 3.15$ QP solution – over multiples of the perturbative timescale – confirms that the solution remains quasi-periodic and does not collapse.

3.4.4.2 Constraint Equations

Another indicator of possible collapse and/or violation of the perturbative approximation is the growth of residuals when the TTF solutions are substituted into the Einstein equations. The residuals are calculated by reconstructing the time dependence of the scalar field and its derivatives using the amplitude-phase variables, and comparing the $\mathcal{O}(\epsilon^2)$ values of the derivatives of the metric



(a) Energy spectra when projecting back to the QP solution plane every 5 iterations for an initial $\alpha_1 = 0.44$, QP solution (see figure 3.2a for temperature and α_1 as a function of iteration).

(b) The same initial QP solution as figure 3.3a is used, but is projected back to the QP plane every 20 iterations.

Figure 3.3: Comparing energy spectra of high-temperature perturbations of an $\alpha_1 = 0.44$ QP solution that have been projected back to the QP plane at different frequencies.

functions in (3.5)-(3.6). In particular, using the numerical values of the amplitude-phase variables A_j and B_j , (3.11) gives the value of the leading-order scalar field contribution, $\phi_1(t, x)$. The $\mathcal{O}(\epsilon^2)$ contribution to the derivatives of metric functions come from

$$\partial_x \delta_2(t, x) = -\sin(x) \cos(x) ((\partial_x \phi_1)^2 + (\partial_t \phi_1)^2), \quad (3.24)$$

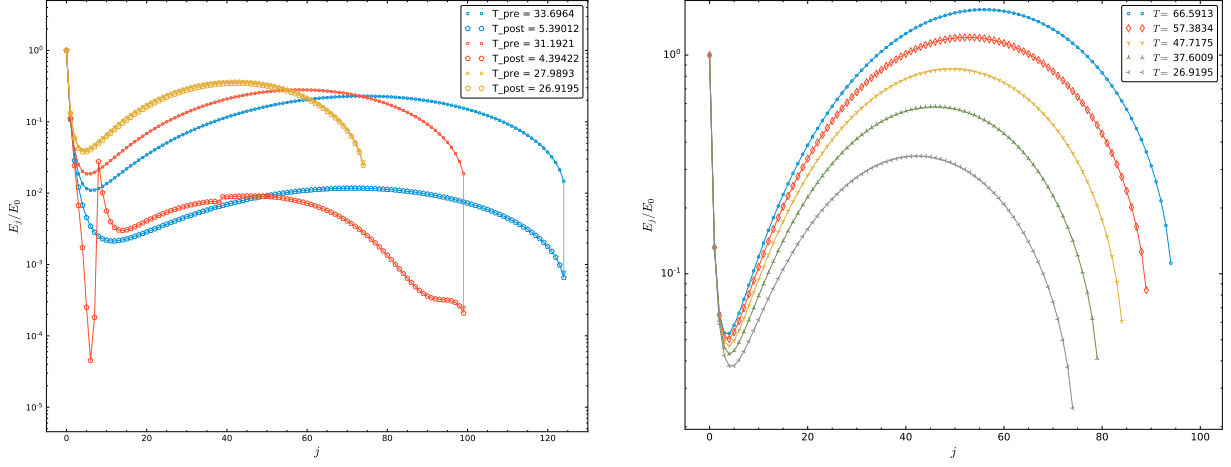
$$\partial_x A_2(t, x) = -\frac{1-d+\cos(2x)}{\sin(x) \cos(x)} (A_2 - 1) - \sin(x) \cos(x) ((\partial_x \phi_1)^2 + (\partial_t \phi_1)^2), \quad (3.25)$$

$$\text{with } A_2(t, x) = -\frac{\cos^d(x)}{\sin^{d-1}(x)} \int_0^x \tan^{d-1}(y) ((\partial_t \phi_1)^2 + (\partial_x \phi_1)^2) dy. \quad (3.26)$$

The L^2 -norm of the differences between (3.24)-(3.25) and (3.5)-(3.6) would constitute the residuals of the Einstein equations. However, while the leading-order contribution to the residuals is $\mathcal{O}(\epsilon^4)$, there are in fact higher order terms that enter into the calculation of $\partial_t \phi$. A careful evaluation of the constraints would therefore include calculating the $\mathcal{O}(\epsilon^4)$ term in the metric function $A(t, x)$ so that the product $A(\Phi^2 + \Pi^2)$ would include terms $\mathcal{O}(\epsilon^6)$. Instead, we limit our focus to examining only the difference between (3.5) and (3.24), which does not suffer from higher-order contributions. The examination of residuals is taken as a suggestion of how well a TTF solution continues to satisfy the Einstein equations throughout its evolution. In figure 3.6, we show the absolute and relative L^2 -norms both QP and high temperature solutions.

3.5 Time Evolution of Quasi-Periodic Solutions

Using the numerical evolution methods from [24], we use a variety of quasi-periodic and high-temperature solutions discussed above as initial data. We then examine their evolution under



(a) QP solutions perturbed to $T_{\text{max}} = 30.00$, which were then used as seeds for the nonlinear solver. Arrows are oriented from pre-optimized to post-optimized solutions.

(b) Extensions of the $j_{\text{max}} = 50$ solution from figure 3.4a to larger j_{max} solutions using tail fitting on only the final 5 modes of the solution.

Figure 3.4: Constructing high temperature solutions “by hand.”

(3.15)-(3.16).

For each type of solution below, we can generate the following plots:

- Ricci scalar at the origin
- Einstein equation residuals
- Energy spectra (mode evolution, full spectrum evolution)
- QP equation residuals
- Projection of amp/phase intermediate solutions back to QP plane

3.5.1 Quasi-Periodic Solutions

Consider first the evolution of a known QP solution. We see in figure 3.7 that the fraction of the total energy in the lowest- j modes remains constant over the duration of the evolution, while the fraction in the highest- j modes increases after $\tau \simeq 0.3$. Given the scale of the energy in the modes $j \geq 96$, this growth can mainly be attributed to numerical errors.

To better understand how well the QP solutions continue to satisfy the TTF equation throughout their time evolution, we evaluate the residuals of (3.19) using data taken during the evolution. Figure 3.8 is a sample of the L^2 -norm of these residuals using values for the amplitude-phase variables $A_j(\tau)$, $B_j(\tau)$ during evolution. We also examine changes in the spectrum during the evolution, and show that there is very little deviation between the initial and final spectra for QP solutions beyond numerical drift.

Furthermore, we can attempt to project the evolved solutions back to the QP plane at various times

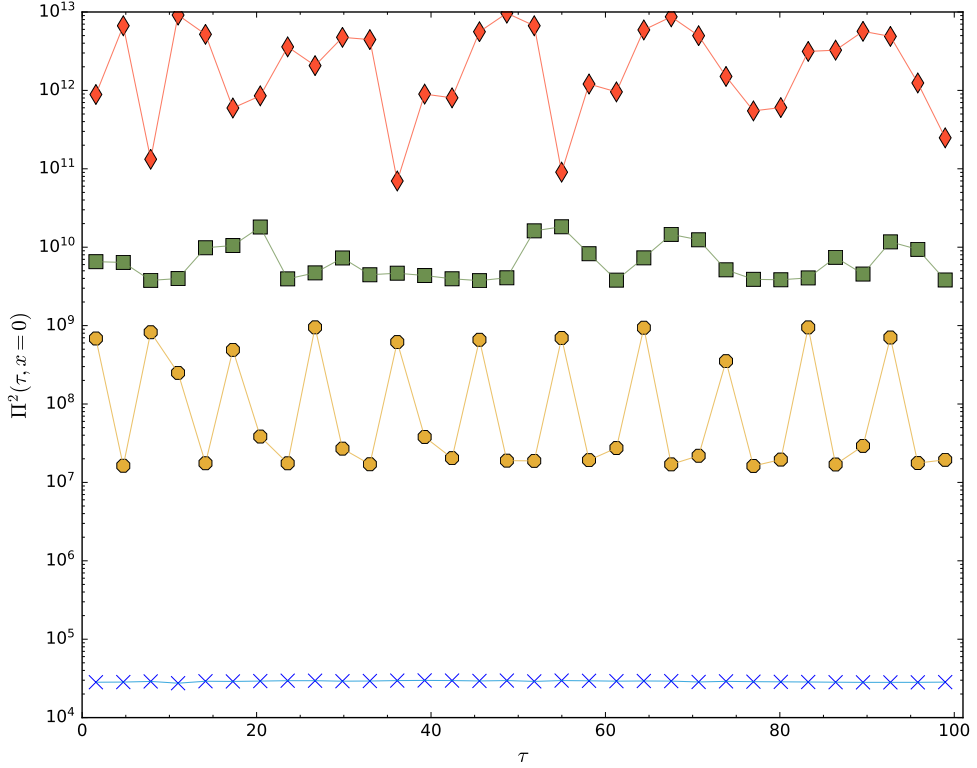
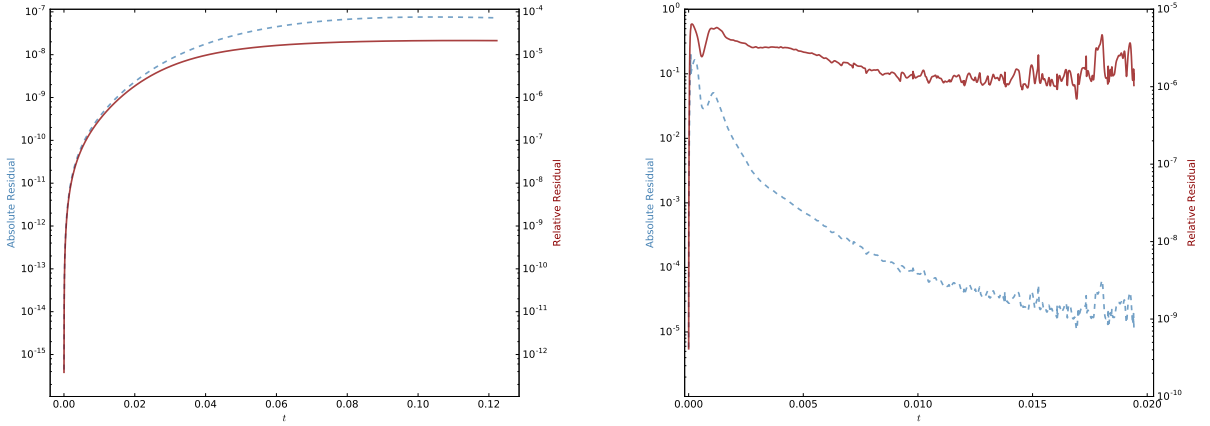


Figure 3.5: Comparing the upper envelope of Π^2 at the origin per light-crossing time for selected low- and high-temperature solutions with $\epsilon = 1$: $j_{\max} = 375$, $QP T \simeq 3.15$ (blue crosses); $j_{\max} = 75$, high-temperature $T \simeq 26.9$ (yellow octagons); $j_{\max} = 100$, high temperature $T \simeq 75.35$ (green squares); $j_{\max} = 95$, high temperature $T \simeq 66.6$ (red diamonds).

to explore if these solutions loose their quasi-periodic nature. We observe that the time-evolved, low-temperature QP solutions are easily projected back to the solution plane at all times during the evolution, and that the resulting solutions solve the QP equation (3.19) to a high degree of accuracy (see figure 3.9a). While this is to be expected for such low-temperature QP solutions, we will soon see that even padding a known QP solution with zeros causes the loss of quasi-periodicity during evolution. For comparison, figure 3.9b shows the results of attempting to project a QP solution that has been padded with zeros back to the QP plane during its evolution. Note the scale on the plot of the L^2 -norm in either case.

3.5.1.1 Padded QP Solutions

In an effort to extend the space of QP solutions, another method used to find solutions that exist nearby known QP solutions – but are not accessible through perturbative or conventional seeding methods – is to pad a given quasi-periodic solution with extra modes that are initially set to zero. Upon amplitude-phase evolution, the energy in the lower- j modes will flow into the higher- j modes and a new quasi-periodic solution may be found. In figure 3.10, we construct initial data out of a known $j_{\max} = 100$, $T \simeq 3.14$ solution by padding with zeros up to $j_{\max} = 200$. As in the case of unpadded QP solution, the fraction of the total energy in the first four modes does not vary



(a) An $\alpha_1 = 0.44$, $j_{max} = 100$ QP solution with $\epsilon = 0.001$.

(b) A $j_{max} = 100$, high-temperature solution is padded with zeros to $j_{max} = 125$ and evolved with $\epsilon = 0.001$.

Figure 3.6: Residuals from evaluating the constraints for QP and high temperature solutions.

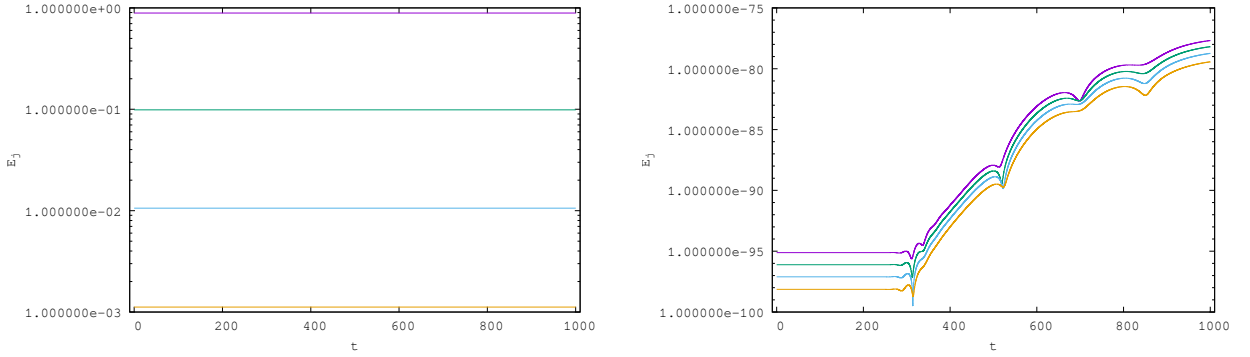
during the evolution and the highest modes accumulate some numerical error before levelling off. In figure 3.10d, we see the accumulation of numerical error in the higher modes as the evolution progresses. Also included is the value of the Ricci scalar at the origin, and the residuals of the QP equation throughout the evolution.

Despite the somewhat normal profile of the spectra of padded QP solution, we see in figure 3.9b that intermediate solutions during the evolution in fact *do not* project back to the QP plane. Rather, as hinted at by the Einstein equation residuals shown in figure 3.10f, the solutions have drifted away from their quasi-periodic initial data. It remains to be seen whether such profiles would be stable in the fully nonlinear system.

Using a known QP solution, we may ask how far away from the solution plane we can move by padding with an incremental number of zeros. In figure 3.11, we show the result of using intermediate solutions from the amplitude/phase evolution of a $j_{max} = 100$ QP solution padded with only five modes (initially set to zero). Despite QP solutions existing for $j_{max} = 105$, no solution was found when using the padded solution – at any point in its evolution – as a seed.

3.5.2 High-Temperature Solutions

High-temperature solutions are those that are found by repeated applications of energy perturbations described in § 3.4.2. These come in several varieties based on the methods used to obtain them; namely, the frequency of projection back to the QP solution plane versus constructing solutions “by hand.” Note that solutions obtained without projecting back to the QP plane, or via the threshold temperature method, *are not* robust in the limit of large j_{max} (see Appendix 3.C for further discussion on the extension of high-temperature solutions to large j_{max}). However, it will be useful nonetheless to contrast their behaviour with other high-temperature solutions.



(a) From top to bottom: $j = 0, 1, 2, 3$ (purple, green, blue, orange). (b) From top to bottom: $j = 96, 97, 98, 99$ (purple, green, blue, orange).

Figure 3.7: Amplitude-phase evolution of an $\alpha_1 = 0.2$, $j_{max} = 100$, QP solution with $\epsilon = 0.01$. Similar behaviour is observed for higher j_{max} solutions and over values of $0.2 \leq \alpha_1 \leq 0.44$.

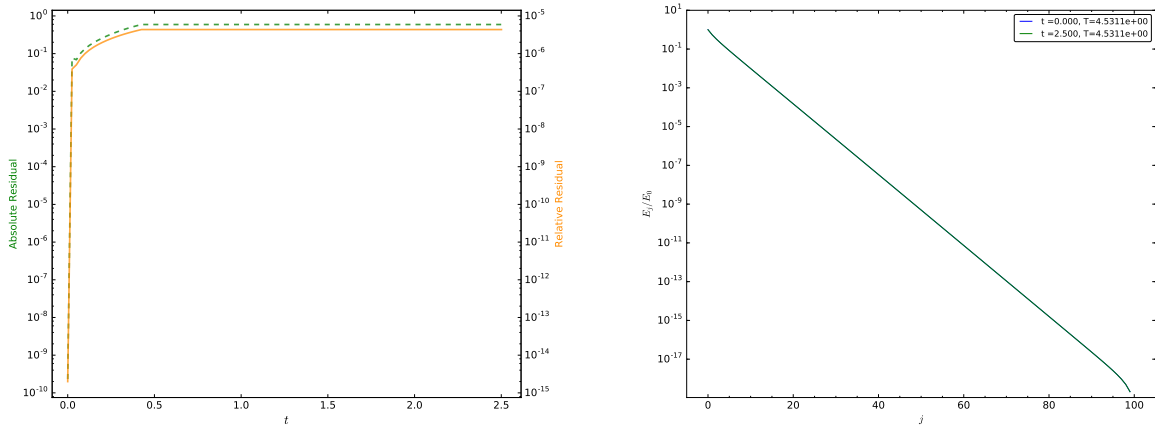
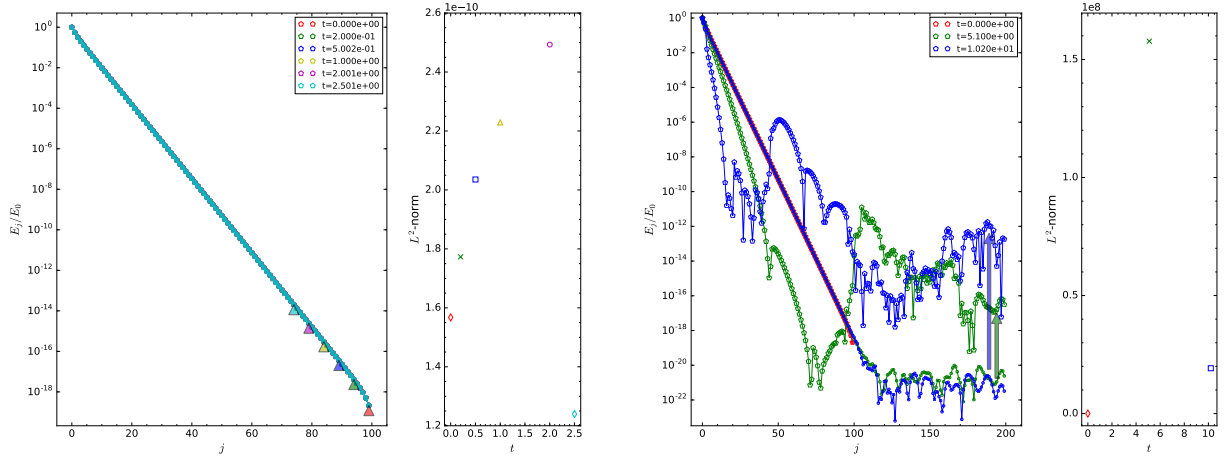


Figure 3.8: Left: L^2 -norm of the residuals of (3.19) evaluated at intervals of 0.025 during the evolution of a $j_{max} = 100$, $\alpha_1 = 0.44$ QP solution with $\epsilon = 0.1$. Right: The spectra of the QP solution at the beginning and end of the evolution.

3.5.2.1 Regular Projections to the QP Plane

Here we examine a high-temperature solution obtained from repeatedly adding small amounts of energy to a $j_{max} = 100$, $\alpha_1 = 0.44$ QP solution. First, we consider threshold temperature solutions discussed in §3.4.2 – those that are on the cusp of quasi-periodic data but cannot be found through solving (3.19) alone. See figure 3.12 for results.

Threshold temperature solutions behave much like low-temperature quasi-periodic solutions: no energy transfer occurs among the leading modes, while very little occurs in the highest modes. Note the scale in figure 3.12b. Unlike other QP solutions with similar total number of modes, the highest modes in threshold temperature solutions contain $\mathcal{O}(10^{-7})E_T$. This relatively high value of the fraction of the total energy means that numerical errors remain suppressed throughout the evolution.



(a) Projected solutions for a low-temperature, QP solution and their L^2 -norms at $t \simeq 0.0, 0.2, 0.5, 1.0, 2.0, 2.5$ (red diamond, green cross, blue square, yellow triangle, magenta circle, blue diamond).

(b) The same QP solution is padded with zeros out to $j_{max} = 200$ and evolved in time. Intermediate solutions are projected back to the QP plane at $t \simeq 0.0, 5.1, 10.2, \dots$ (red diamond, green cross, blue square ...)

Figure 3.9: Intermediate values from the amplitude/phase evolution of a solution are used as seeds for the nonlinear solver at various times. Arrows are oriented from amplitude/phase seed values (circles) to QP plane projections (pentagons).

3.5.2.2 “By Hand” High-Temperature Solutions

Following the method outlined in § 3.4.3, we consider high-temperature solutions constructed by hand out of lower j_{max} solutions. We now examine the behaviour of one such solution under amplitude-phase evolution.

Attempt padding out to $j_{max} = 125$ and run the evolution: see figure 3.14

Finally, consider padding such a solution out to $j_{max} = 200$. See figure 3.15 for results.

The evolved profile of the high-temperature solution can no longer be projected back to the QP solution plane: figure 3.16.

3.5.2.3 Perturbing to an Intermediate Temperature Before Reoptimizing

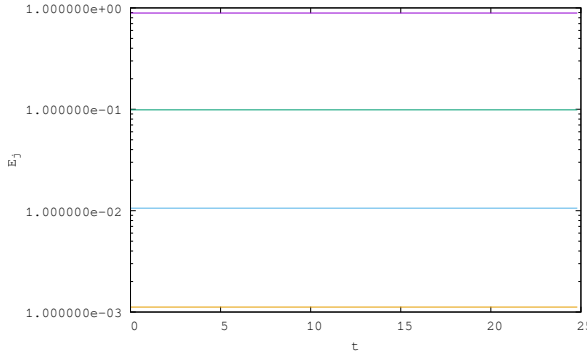
Here, a QP solution is perturbed to a high temperature without regular projections back to the QP plane. At a pre-determined temperature cutoff, $T = 20.0$, the perturbation procedure is halted and the solution is used as a seed for the nonlinear solver. Instead of projecting to a QP solution at a high temperature, the nonlinear solver converges to a solution with only $T \sim 6.71$. We apply the amplitude-phase evolution procedure to the intermediate $T = 20.0$ solution in order to study how a solution far away from the QP plane may behave. See figure 3.17 for results.

3.5.2.4 Padded Threshold Temperature Solutions

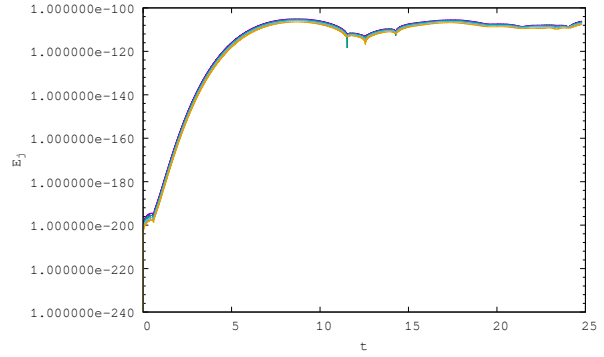
Padding the threshold temperature solution of $T \sim 5.4$ from $j_{max} = 100$ to $j_{max} = 200$ and then evolving in time produces very little change in the spectrum's profile. See figure 3.18 for results. Despite appearing to remain a high-temperature solution, the evolution of this profile renders it non-QP, as shown in figure 3.19. For a more concrete examination, figure 3.20 shows the threshold temperature solution for $j_{max} = 200$ as well as padded threshold solutions during their evolution. Under amplitude/phase evolution, the padded solution *does not* approach the known threshold solution.

3.6 Discussion

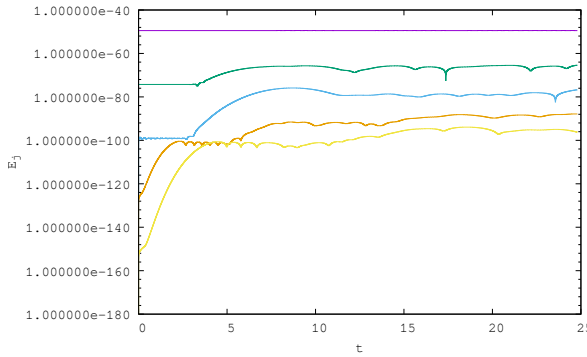
Acknowledgments The work of ND is supported in part by a Natural Sciences and Engineering Research Council of Canada PGS-D grant to ND, NSF Grant PHY-1606654 at Cornell University, and by a grant from the Sherman Fairchild Foundation. The work of BC and AF is supported by the Natural Sciences and Engineering Research Council of Canada Discovery Grant program. This research was enabled in part by support provided by WestGrid (www.westgrid.ca) and Compute Canada Calcul Canada (www.computecanada.ca).



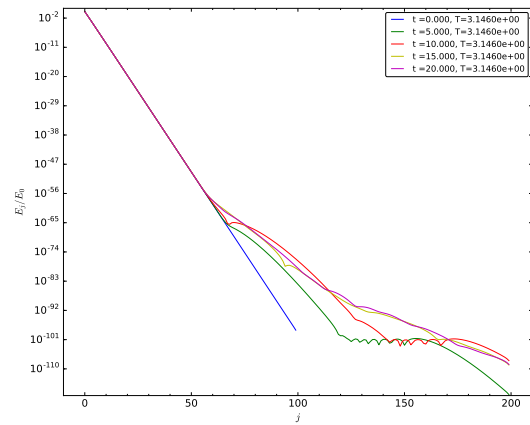
(a) The evolution of the first four modes of the padded QP solution: $j = 0, 1, 2, 3$ (purple, green, blue, orange).



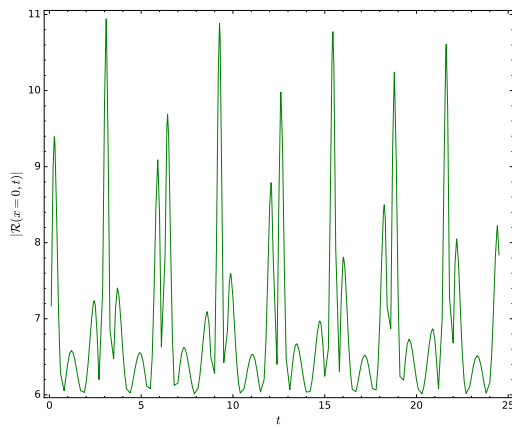
(b) The evolution of the last four modes: $j = 196, 197, 198, 199$ (purple, green, blue, orange).



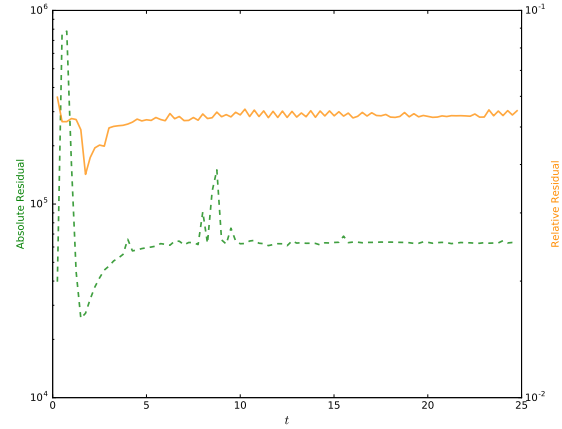
(c) Comparing the evolution of a selection of modes: $j = 50, 75, 100, 125, 150$ (purple, green, blue, orange, yellow).



(d) The total spectrum of the padded QP solution as a function of time.



(e) The Ricci scalar at the origin as a function of time for the padded QP solution.



(f) The residuals of the QP equation (3.19) throughout the amplitude-phase evolution of the padded QP solution.

Figure 3.10: The evolution of the padded QP solution for $\alpha_1 = 0.2$ and $j_{max} = 200$, with amplitude $\epsilon = 0.1$.

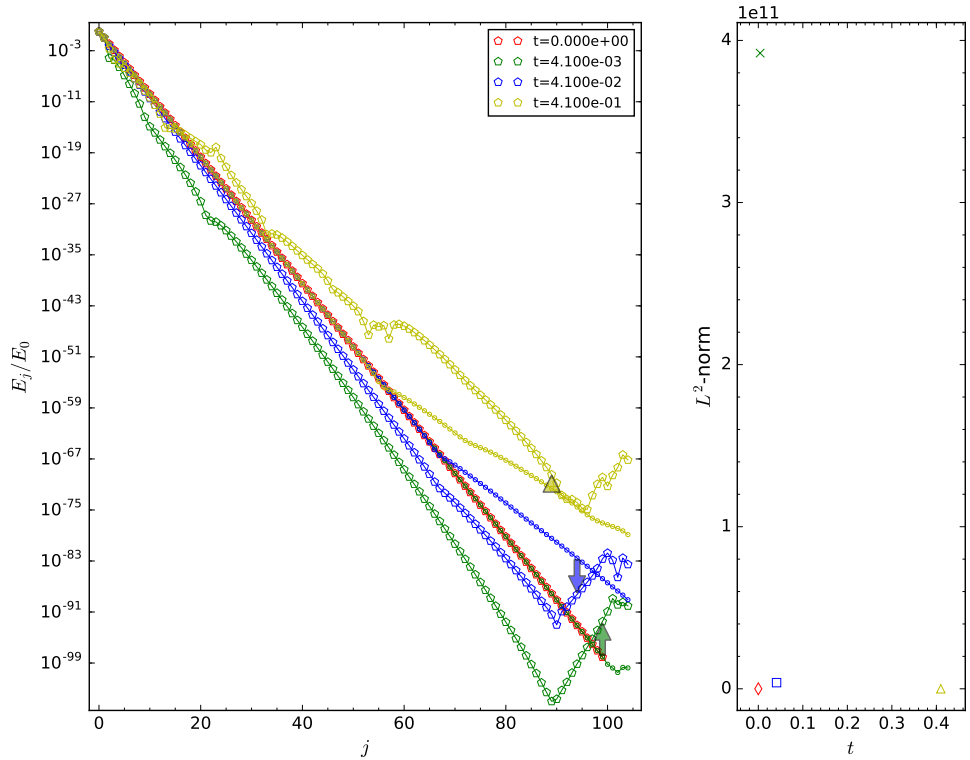


Figure 3.11: *Left:* Normalized spectra for a $j_{max} = 100$, QP solution that has been padded with five extra modes, then evolved in time. Intermediate spectra are used as seeds for projecting back to the QP plane at times $\tau \simeq 4.1 \times 10^{-3}, 4.1 \times 10^{-2}, 4.1 \times 10^{-1}$ (green, blue, yellow). Arrows are oriented from seed spectra to best fit spectra. *Right:* Corresponding L^2 -norms of the error for each solution.

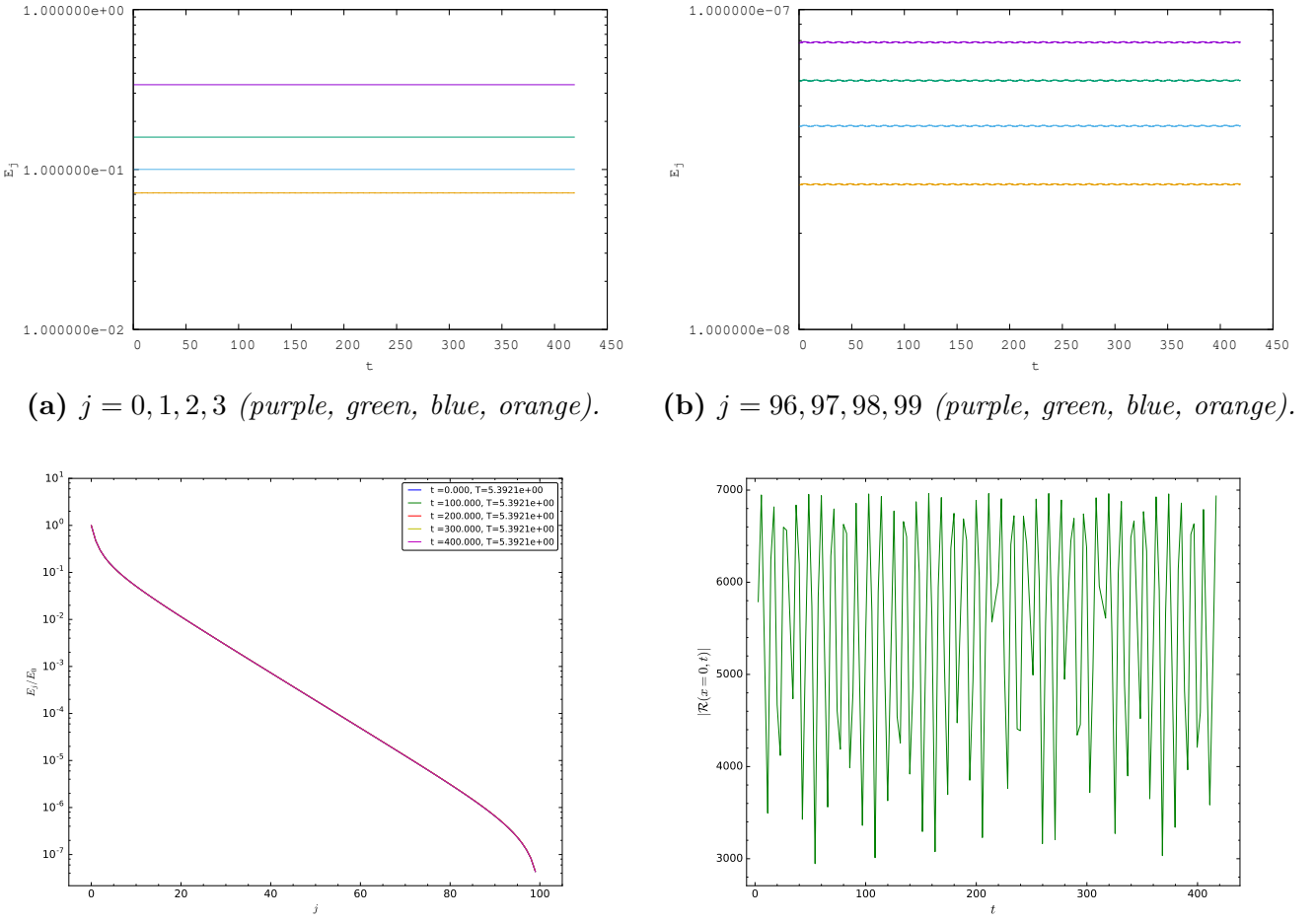


Figure 3.12: Above: The evolution the fraction of the total energy in specific modes for a $T \sim 5.4$, threshold temperature solution for $\tau \in [0, 4.25]$. Below: Snapshots of the full spectrum at various times in its evolution, as well as the upper envelope of $|\mathcal{R}(t, x = 0)|$ when $\epsilon = 0.1$.

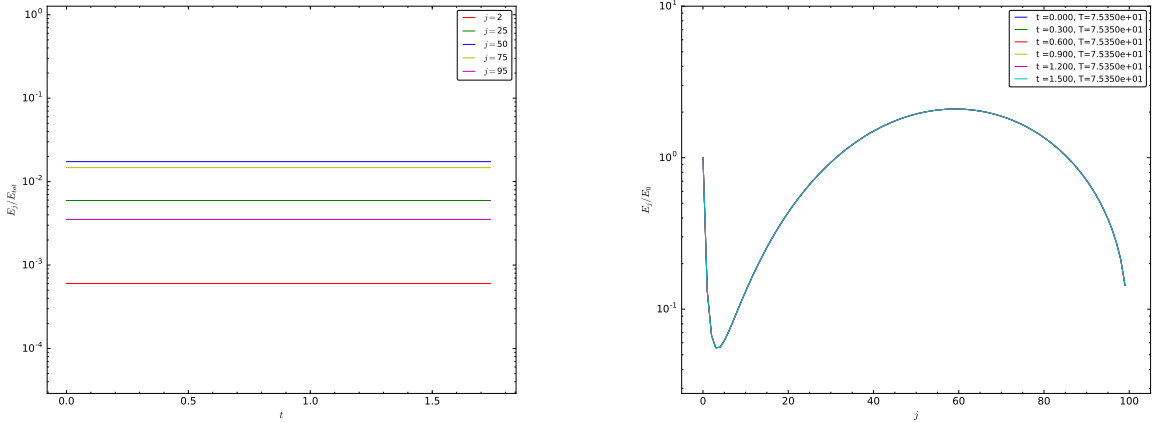


Figure 3.13: The evolution of a high-temperature solution created by hand from lower j_{\max} solutions.

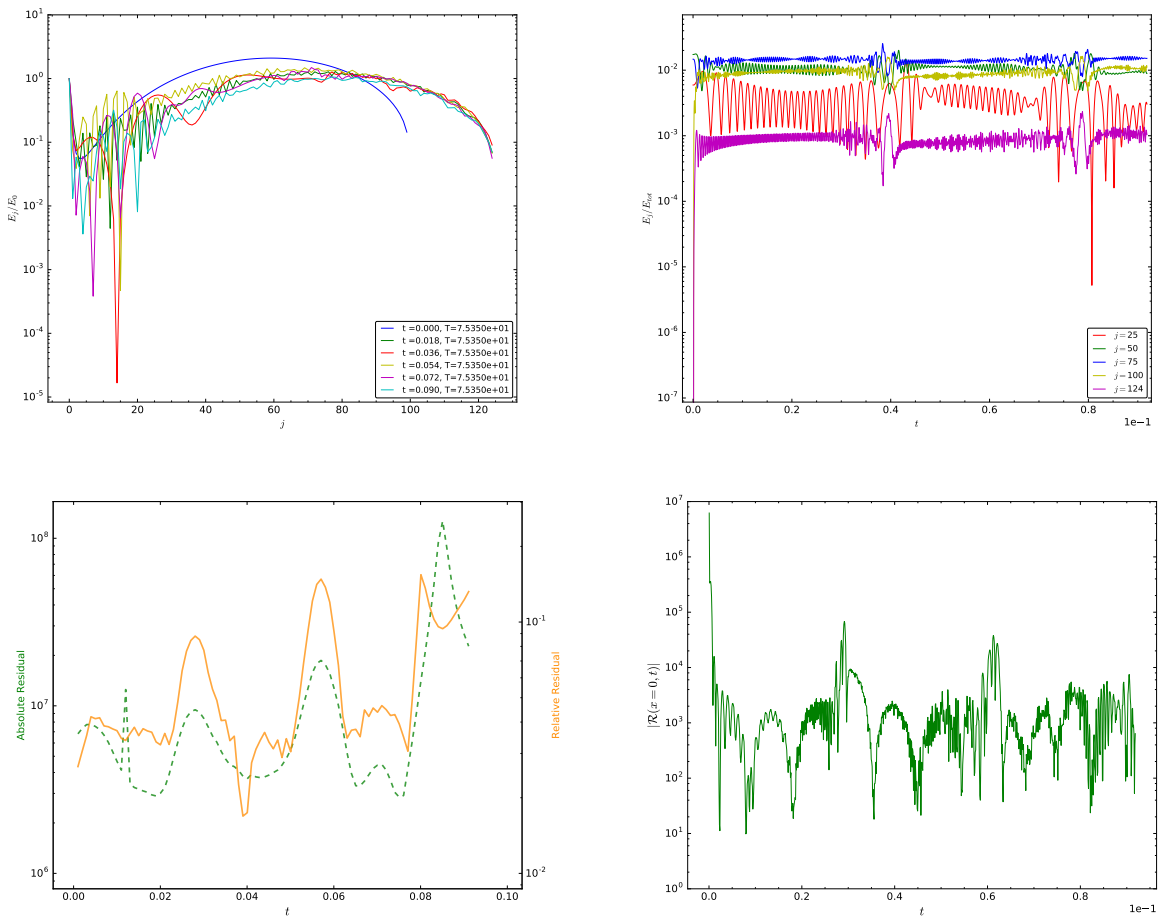


Figure 3.14: Padding the same initial solution from figure 3.4, but with only 25 extra modes.

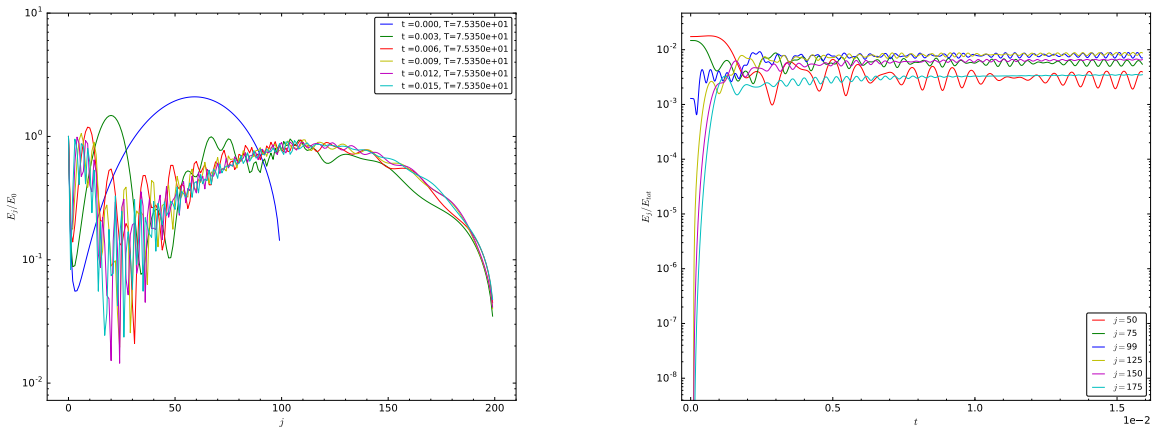


Figure 3.15: Padding a $j_{max} = 100$, high temperature solution to $j_{max} = 200$ and evolving in time. $\epsilon = 0.1$

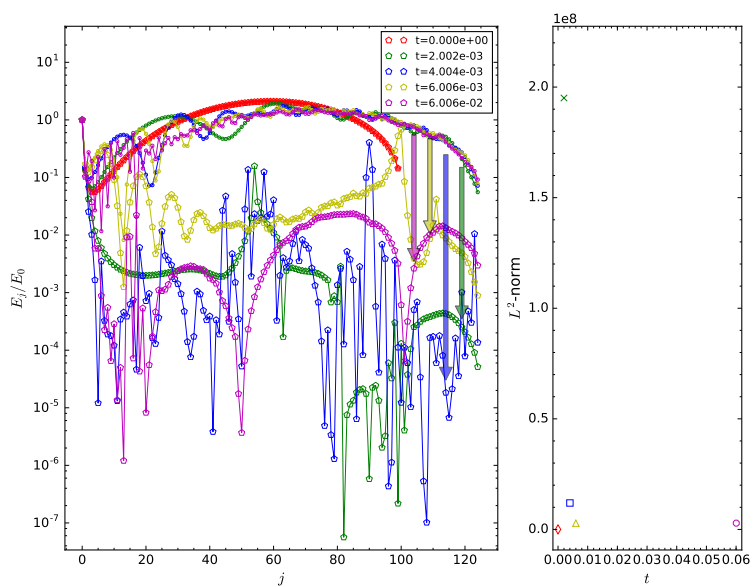


Figure 3.16: A high-temperature solution is padded with 25 extra modes, then evolved in time. Above are the results of projecting back to the QP plane at $t \simeq 0.002, 0.004, 0.006, 0.06$ (red diamond, green cross, blue square, yellow triangle, magenta circle).

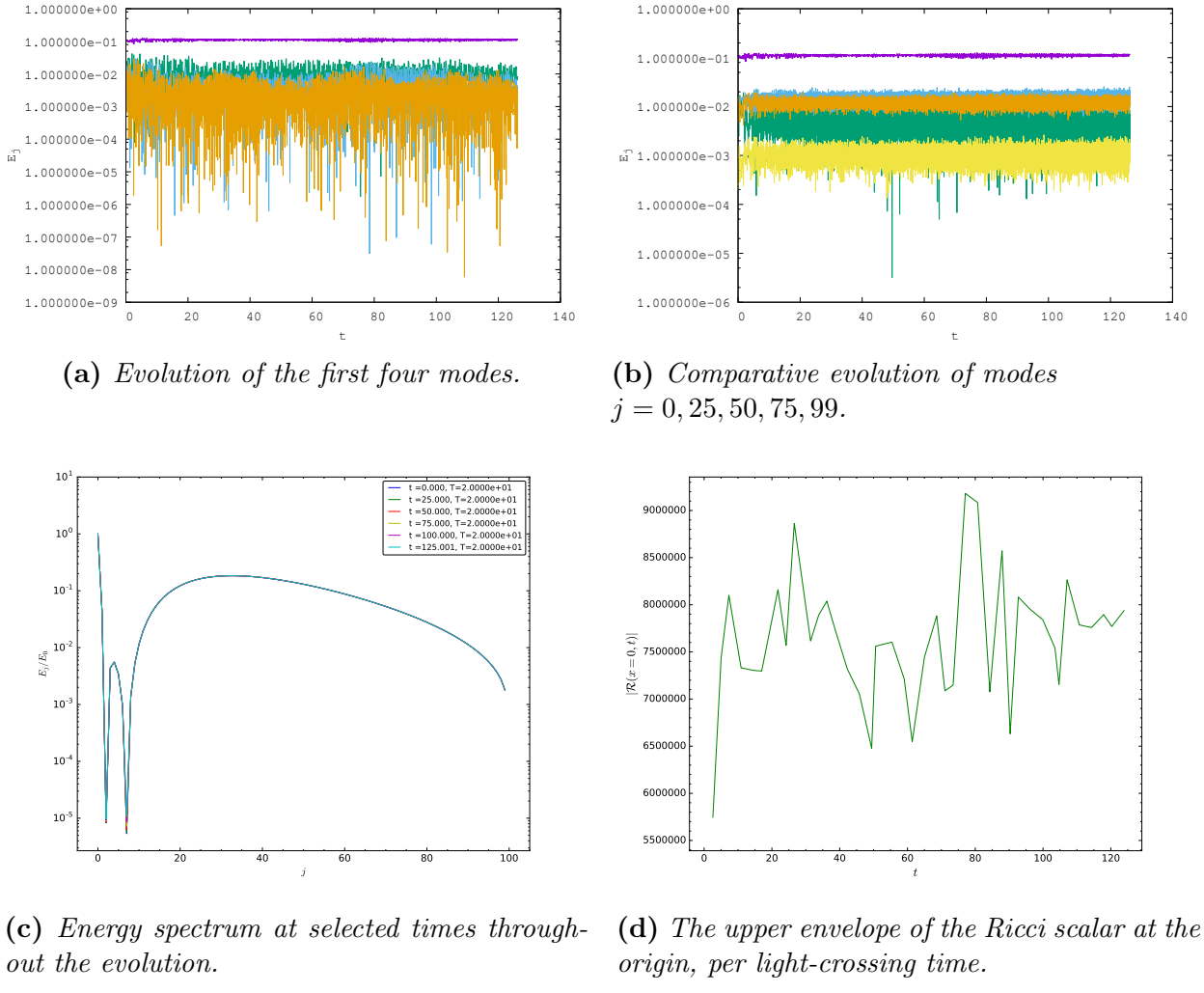


Figure 3.17: The evolution of an intermediate, high-temperature solution that does not correspond to a solution of the QP equations.

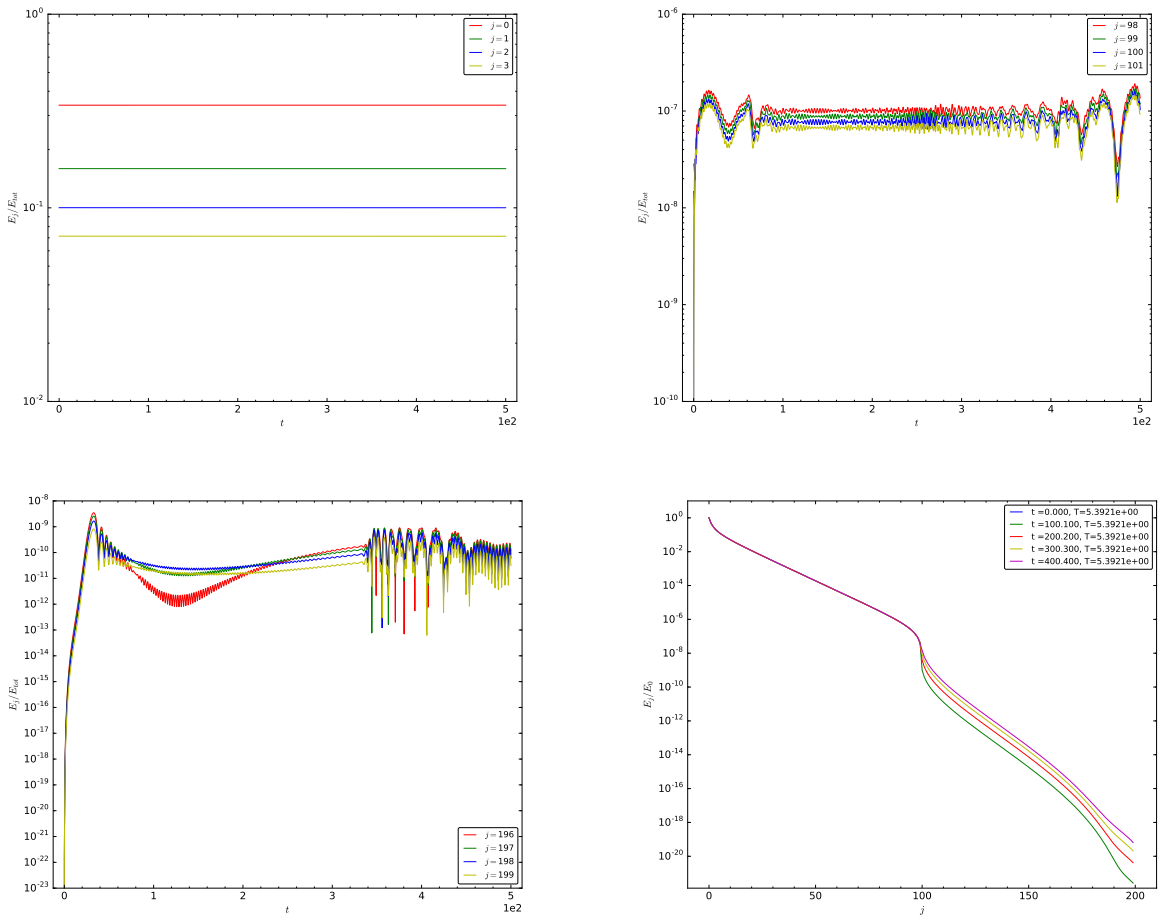
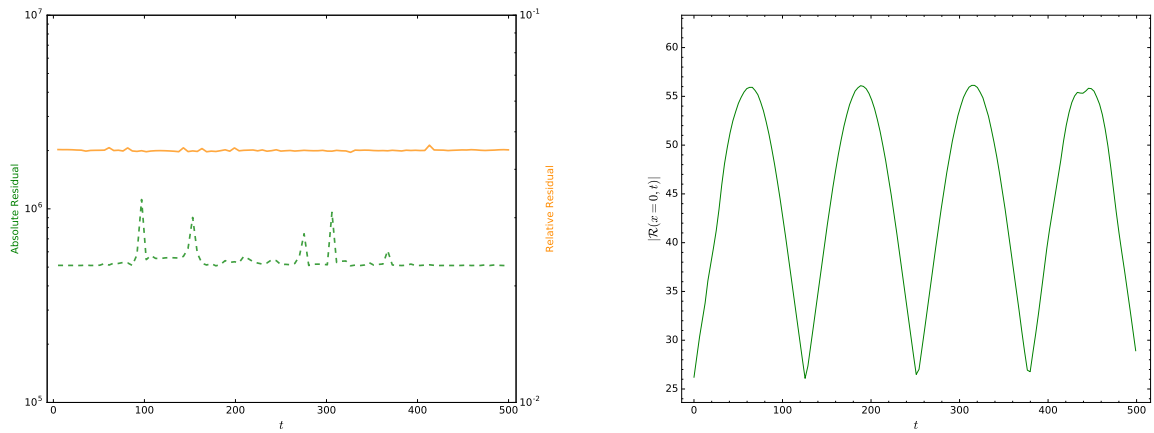


Figure 3.18: Padding a threshold temperature solution



(a) The residuals of (3.19) during the evolution of the padded threshold temperature solutions shown in figure 3.18.

(b) The upper envelope of the Ricci scalar at the origin per light-crossing time for the padded threshold temperature solution.

Figure 3.19: Despite the spectrum of the padded threshold temperature solution (figure 3.18) resembling that of lower-temperature QP solutions, these solutions move away from the QP plane and can no longer be projected back.

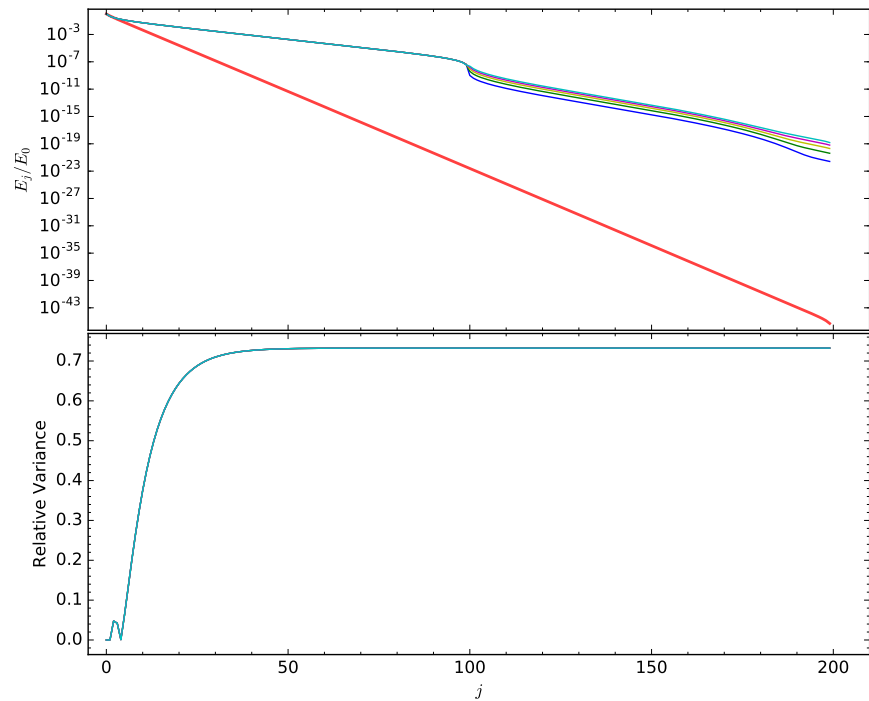


Figure 3.20: Top: Overlay of the known threshold temperature solution for $j_{max} = 200$ (thick red line) with snapshots of the spectra of a $j_{max} = 100$ threshold solution that has been padded with zeros to $j_{max} = 200$ after amplitude/phase evolutions of $\tau = 1, 2, 3, 4, 5 \times 10^{-5}$ (blue, green, yellow, magenta, cyan). Bottom: The absolute value of the difference between the cumulative sums of the $j_{max} = 200$ threshold temperature solution and each snapshot spectrum (same colouring).

Appendix

3.A Seeding Methods For Non-Linear Solvers

While it was originally proposed by [14] that the appropriate seed value for nonlinear solvers be given by the exponential relation ($j > 1$)

$$\alpha_j \sim \frac{3e^{-\mu j}}{2j + 3} \quad (3.27)$$

in AdS₄, where $\mu = \ln(3/5\alpha_1)$, as j_{max} increased, the seed values diverged significantly from the true solutions (see figure 3.A.1 for a comparison between known QP solutions and the seeds generated by (3.27)). Although this profile was sufficient for low j_{max} solutions, above $j_{max} \gtrsim 150$, (3.27) no longer provided an adequate starting guess. To overcome this problem, exponential fitting was applied to the tail values of a known QP solution with lower j_{max} . Using this exponential fit, the data was extrapolated to a higher j_{max} .

Care was taken to avoid edge effects due to truncation when choosing the points that constituted the tail of the data. To illustrate the variance of the solution with truncation, we examine a fixed α_j value over a variety of j_{max} , starting with $\alpha_j = \alpha_{j_{max}}$. In table 3.A.1 we see that the value of α_{50} for QP solutions with $\alpha_1 = 0.2$ becomes impervious to truncation effects once $j_{max} > 55$.

To err on the side of caution, the modes $[j_{max} - 30, j_{max} - 10]$ were used from each QP solution to provide more accurate seed values for $j_{max} + 25$ solutions. See figure 3.A.2a for a comparison of seed values generated by tail fitting to actual QP solutions. The solutions found using this method of seeding versus those found from the seeding given in (3.27) had relative differences on the order of 10^{-14} (see figure 3.A.2b).

3.B Auxiliary Integrals For Calculating the T, R, S Coefficients

The auxiliary coefficients X, Y, W, W^*, A , and V allow the symmetries of the T, R and S coefficients to be more easily recognized and therefore reduce the number of total calculations involved in determining (3.34) - (3.36). These auxiliary coefficients are written simply in terms of the eigenfunctions

j_{max}	α_{50}
50	1.74597252e-26
51	1.82668391e-26
52	1.83346256e-26
53	1.83408260e-26
54	1.83414138e-26
55	1.83414706e-26
60	1.83414768e-26
65	1.83414768e-26
70	1.83414768e-26
75	1.83414768e-26

Table 3.A.1: α_{50} values for various j_{max} QP solutions.

in (3.9) and their derivatives. Explicitly, they are

$$X_{ijkl} = \int_0^{\pi/2} dx e'_i(x) e_j(x) e_k(x) e_l(x) \sin(x) \cos(x) (\tan(x))^{d-1} \quad (3.28)$$

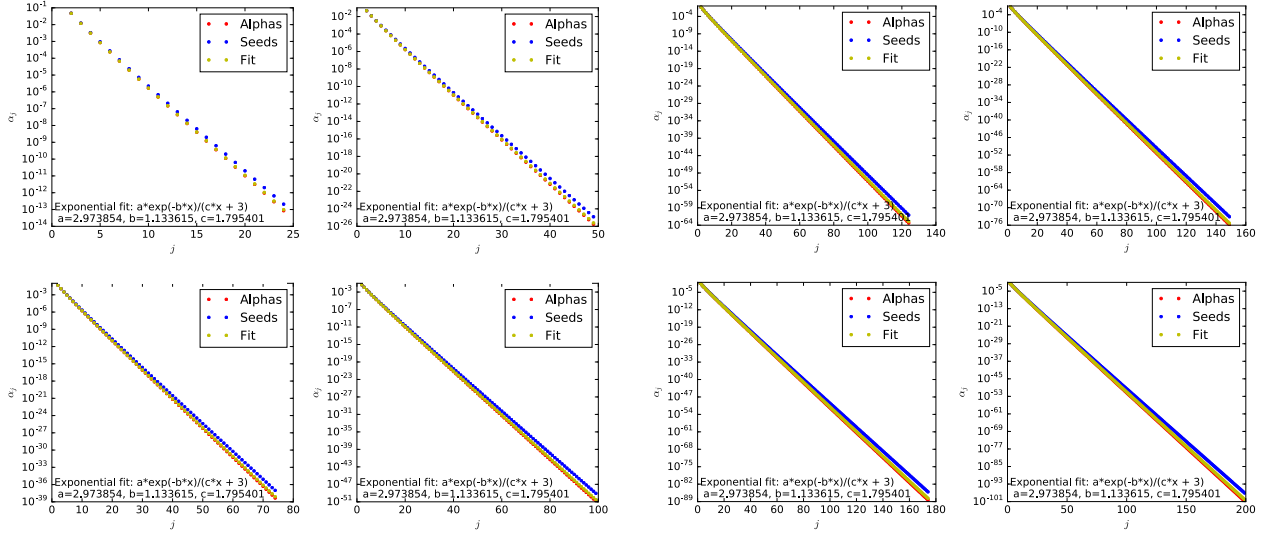
$$Y_{ijkl} = \int_0^{\pi/2} dx e'_i(x) e_j(x) e'_k(x) e'_l(x) \sin(x) \cos(x) (\tan(x))^{d-1} \quad (3.29)$$

$$W_{ijkl} = \int_0^{\pi/2} dx e_i(x) e_j(x) \sin(x) \cos(x) \int_0^x dy e_k(y) e_l(y) (\tan(y))^{d-1} \quad (3.30)$$

$$W_{ijkl}^* = \int_0^{\pi/2} dx e'_i(x) e'_j(x) \sin(x) \cos(x) \int_0^x dy e_k(y) e_l(y) (\tan(y))^{d-1} \quad (3.31)$$

$$A_{ij} = \int_0^{\pi/2} dx e'_i(x) e'_j(x) \sin(x) \cos(x) \quad (3.32)$$

$$V_{ij} = \int_0^{\pi/2} dx e_i(x) e_j(x) \sin(x) \cos(x). \quad (3.33)$$



(a) $\alpha_1 = 0.2$ QP solutions for $j_{max} \in [25, 100]$. (b) $\alpha_1 = 0.2$ QP solutions for $j_{max} \in [140, 200]$.

Figure 3.A.1: A comparison of seeds predicted by (3.27) to known QP solution. Also included for comparison are the results of fitting the QP solutions to a generic exponential fit.

In terms of these coefficients, the TTF source terms are given by

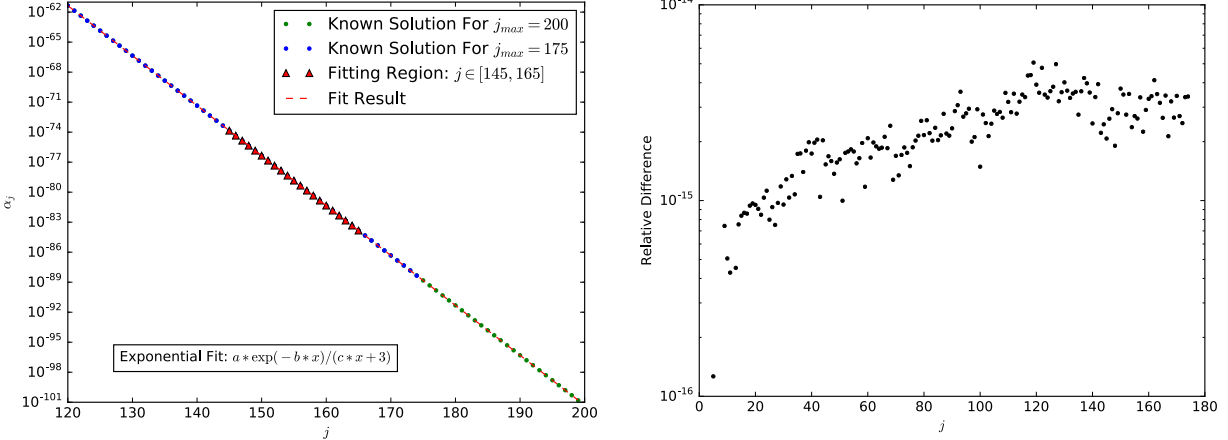
$$T_l = \frac{1}{2}\omega_l^2 X_{lll} + \frac{3}{2}Y_{lll} + 2\omega_l^4 W_{lll} + 2\omega_l^2 W_{lll}^* - \omega_l^2(A_{ll} + \omega_l^2 V_{ll}) \quad (3.34)$$

$$\begin{aligned} R_{il} = & \frac{1}{2} \left(\frac{\omega_i^2 + \omega_l^2}{\omega_l^2 - \omega_i^2} \right) (\omega_l^2 X_{illi} - \omega_i^2 X_{lili}) + 2 \left(\frac{\omega_l^2 Y_{ilil} - \omega_i^2 Y_{lili}}{\omega_l^2 - \omega_i^2} \right) \\ & + \left(\frac{\omega_i^2 \omega_l^2}{\omega_l^2 - \omega_i^2} \right) (X_{illi} - X_{lili}) + \frac{1}{2}(Y_{ill} + Y_{lli}) + \omega_i^2 \omega_l^2 (W_{llii} + W_{iill}) \\ & + \omega_i^2 W_{lli}^* + \omega_l^2 W_{ill}^* - \omega_l^2(A_{ii} + \omega_i^2 V_{ii}) \end{aligned} \quad (3.35)$$

$$\begin{aligned} S_{ijkl} = & -\frac{1}{4} \left(\frac{1}{\omega_i + \omega_j} + \frac{1}{\omega_i - \omega_k} + \frac{1}{\omega_j - \omega_k} \right) (\omega_i \omega_j \omega_k X_{lijk} - \omega_l Y_{lijk}) \\ & - \frac{1}{4} \left(\frac{1}{\omega_i + \omega_j} + \frac{1}{\omega_i - \omega_k} - \frac{1}{\omega_j - \omega_k} \right) (\omega_j \omega_k \omega_l X_{ijkl} - \omega_i Y_{ijkl}) \\ & - \frac{1}{4} \left(\frac{1}{\omega_i + \omega_j} - \frac{1}{\omega_i - \omega_k} + \frac{1}{\omega_j - \omega_k} \right) (\omega_i \omega_k \omega_l X_{jikl} - \omega_j Y_{jikl}) \\ & - \frac{1}{4} \left(\frac{1}{\omega_i + \omega_j} - \frac{1}{\omega_i - \omega_k} - \frac{1}{\omega_j - \omega_k} \right) (\omega_i \omega_j \omega_l X_{kijl} - \omega_k Y_{kijl}). \end{aligned} \quad (3.36)$$

3.C Frequency of Solution Checking

The frequency of applying the nonlinear solver to project back down to the QP solution plane is an important part of ensuring that the perturbative method remains applicable. If QP solutions are perturbed by too large an energy, or for too many iterations, the intermediate solutions may not be



(a) Fitting the tail of the $j_{max} = 175$ spectrum to construct a seed for $j_{max} = 200$ at fixed $\alpha_1 = 0.2$. Also included is actual QP spectrum for $j_{max} = 200$.

(b) Relative difference between $\alpha_1 = 0.2$ QP solutions found using tail-fitting and those from the exponential profile (3.27).

Figure 3.A.2: The process and result of tail fitting the α_j spectra of QP solutions to generate better seed values.

close enough to the solution plane to provide an adequate seed value. Such was the concern when examining the purported high-temperature solutions from existing sources.

For example, consider the process of applying perturbations of $\delta E = 0.01\%$ up to some intermediate temperature without projecting back to the QP plane, then projecting back every 100 iterations until a maximum temperature is reached. Starting with the QP solution corresponding to $\alpha_1 = 0.2$, the lower panel of figure 3.C.1 shows the result of repeated perturbations of $\delta E = 0.01\%$ that are not projected back to the QP plane.

The behaviour of the spectra differ for the low and high j_{max} cases. For the $j_{max} = 50$ solutions, the spectra in the lower panel of the figure can remain smooth through more than 27,000 iterations of δE perturbations. When a temperature of approximately 17 is reached, the spectrum is used as a seed value for the nonlinear solver and a smooth solution is found. Continuing with the same δE , but reapplying the nonlinear solver produces mixed results; the temperatures of increasing iterations do not increase monotonically, but do always project back to a solution with nearly the same temperature. However, the spectra themselves develop kinks by iteration 3,100 that are indicative of a change of sign in the alpha values and a breakdown of the perturbative condition. Because only a small number of modes are considered, numerical solutions are still found by the Newton-Raphson solver but no longer represent physical states. Continuing this procedure, we find that the solver fails to find a solution even at the modest temperature of $T \simeq 38$.

The behaviour of the $j_{max} = 150$ solutions is consistent with their lower-mode number counterparts, albeit more pronounced. We see that kinks in the spectrum develop even when the nonlinear solver has not been applied. The intermediate solution used as a seed for the nonlinear solver did not project back to a nearby temperature, instead falling from $T \simeq 14.2$ to $T \simeq 4.3$. As the perturbative procedure continued, projection back to the QP plane was only possible in for a short time before no solution could be found. Note the numerous spikes in the energy spectrum shown in the upper

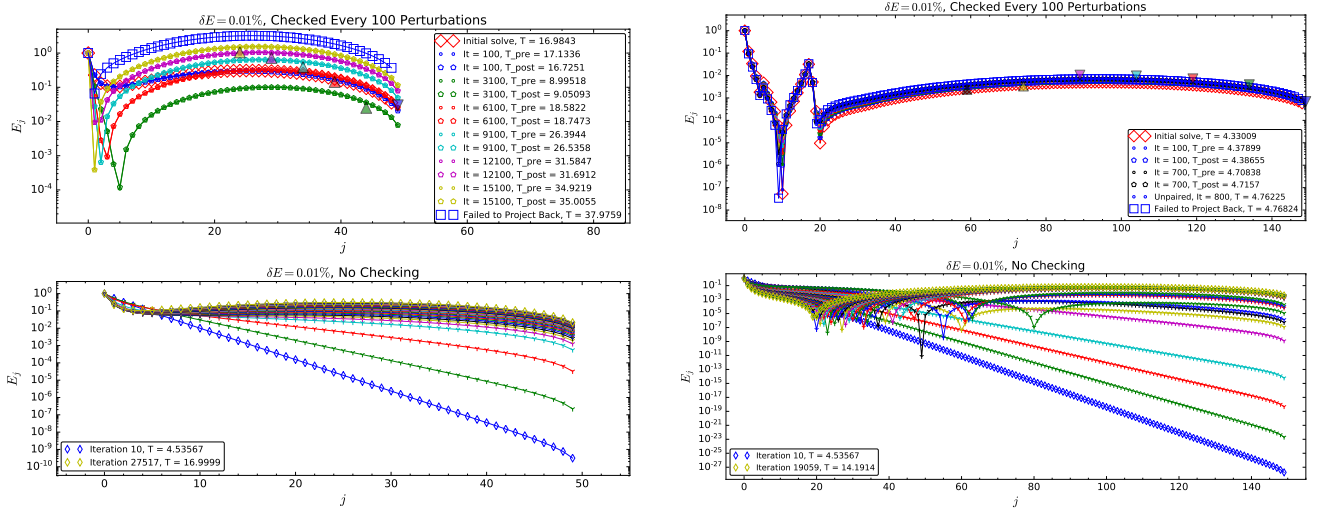


Figure 3.C.1: Left: the result of unchecked perturbations of a $j_{max} = 50$ QP solution up to an intermediate temperature before switching to regular checking. Right: the same procedure is applied to a $j_{max} = 150$ QP solution.

panel. For $j_{max} = 150$, we conclude that no physically relevant high-temperature solutions exist, even as low as $T \simeq 4.76$.

4 Perturbative Descriptions of Driven Instabilities in AdS

Will be published to the arXiv, then submitted to JHEP

4.1 Contributions

All contributions are mine.

Examining Instabilities Due to Driven Scalars in AdS

arXiv:1912.07143

Brad Cownden¹

¹*Department of Physics & Astronomy,
University of Manitoba
Winnipeg, Manitoba R3T 2N2, Canada
cowndenb@myumanitoba.ca*

We extend the study of the non-linear perturbative theory of weakly turbulent energy cascades in AdS_{d+1} to include solutions of driven systems, i.e. those with time-dependent sources on the AdS boundary. This necessitates the activation of non-normalizable modes in the linear solution for the massive bulk scalar field, which couple to the metric and normalizable scalar modes. We determine analytic expressions for secular terms in the renormalization flow equations for any mass, and for various driving functions. Finally, we numerically evaluate these sources for $d = 4$ and discuss what role these driven solutions play in the perturbative stability of AdS.

4.2 Introduction

Nonlinear instabilities in Anti-de Sitter space have been the subject of examinations on several grounds in addition to the holographic description of quantum quenches via the AdS/CFT correspondence [45, 58], including general stability of maximally-symmetric solutions in general relativity [1, 52, 57], and the study of the growth of secular terms in time-dependent perturbation theories [59, 60]. Numerical studies in holographic AdS show that the eventual collapse of a scalar field into a black hole in the bulk (which is dual to the thermalization of the boundary theory) is generic to any finite sized perturbation [1–3], but can be avoided or delayed for certain initial conditions [34, 53, 61, 62]. The mechanism of collapse in such systems is described as a weakly turbulent energy cascade to short length scales. These dynamics can be captured by a non-linear perturbation theory at first non-trivial order through the introduction of a second, “slow time” that describes energy transfer between the fundamental modes. This is known as the Two-Time Formalism (TTF) [6] and yields a renormalization flow equation that allows for the absorption of secular terms into renormalized amplitudes and phases [7, 11, 15, 16]. Therefore, stability against a perturbation of order ϵ is maintained over time scales of $t \sim \epsilon^{-2}$.

Conventional examinations of perturbative stability using TTF have focused on the reaction of the bulk space to some initial energy perturbation, and have aimed to study the balance between direct and inverse energy cascades [14, 24, 25, 63, 64]. Furthermore, numerical examinations of “pumped” scalars and their implications for thermalization of the dual theory have also been examined [65–69]. However, extensions of the perturbative description to include time-dependent sources – corresponding to a driving term on the boundary of the bulk space – remain unaddressed.

With this in mind, we examine the effects that a time-dependent source on the conformal boundary has on the non-linear perturbative theory. The introduction of a driving term on the boundary

means that we must include a second class of fundamental modes with arbitrary frequencies. Since these solutions will have non-finite inner products over the bulk space, they are known as non-normalizable. Non-normalizable modes couple to both the source on the boundary and the regular normalizable modes to bring energy into the system, where direct and inverse energy cascades proceed over perturbative time scales.

To capture these dynamics, we expand the fields in powers of a small perturbation and isolate the secular terms that appear at third order in ϵ . Only modes whose frequencies satisfy certain resonance conditions will contribute terms that cannot be absorbed by simple frequency shifts. The form of the resonant terms depends on the specific physics of the system, as well as possible symmetries between frequencies. Finally, by evaluating the resonant third-order interactions when combinations of normalizable and non-normalizable modes are activated, we can write renormalization flow equations for the slowly varying amplitudes and phases.

This paper is organized as follows: section § 4.3 involves a brief discussion of how we arrive at the third order source term, as well as additional considerations due to the time-dependent boundary condition. As an exercise – and to provide explicit expressions for the resonant contributions when the scalar field has non-zero mass – § 4.4 examines the secular terms in the case of a massive scalar field in AdS_{d+1} with any mass-squared, up to and including the Breitenlohner-Freedman mass [70]: $m_{BF}^2 \leq m^2$. We demonstrate the natural vanishing of two of the three resonances, and then examine the effects of mass-dependence on the non-vanishing channel. Whenever values are calculated, the choice of $d = 4$ is implied as to draw the most direct comparison to existing literature. In section § 4.5, we extend the boundary conditions to include a variety of periodic boundary sources that couple to non-normalizable modes in the bulk. For each choice of boundary condition, we derive analytic expressions for applicable resonances and evaluate these expressions for different ranges of scalar field masses. Finally, in § 4.6 we discuss the implications of non-vanishing resonances on the competing energy cascades, and the implications for the perturbative stability of such systems. For completeness, we include details of our derivation of the general source term in appendix 4.A, as well as a complete list of possible resonance channels and their resulting secular terms in appendix 4.B for the case of two, equal frequency non-normalizable modes.

4.3 Source Terms and Boundary Conditions

Let us first consider a minimally coupled, massive scalar field coupled to a spherically symmetric, asymptotically AdS_{d+1} spacetime in global coordinates, whose metric is given by

$$ds^2 = \frac{L^2}{\cos(x)} (-A(t, x)e^{-2\delta(t, x)} dt^2 + A^{-1}(t, x) dx^2 + \sin^2(x) d\Omega_{d-1}^2), \quad (4.1)$$

where L is the AdS curvature (hereafter set to 1), and the radial coordinate $x \in [0, \pi/2]$. The dynamics of the system come from the Einstein and Klein-Gordon equations:

$$G_{\mu\nu} + \Lambda g_{\mu\nu} = 8\pi \left(\nabla_\mu \phi \nabla_\nu \phi - \frac{1}{2} g_{\mu\nu} (\nabla^\rho \phi \nabla_\rho \phi + m^2 \phi^2) \right) \quad \text{and} \quad \nabla^2 \phi - m^2 \phi = 0, \quad (4.2)$$

with the cosmological constant for AdS given by $\Lambda = -d(d-1)/2$.

Perturbing around static AdS, the scalar field is expanded in odd powers of epsilon

$$\phi(t, x) = \epsilon\phi_1(t, x) + \epsilon^3\phi_3(t, x) + \dots \quad (4.3)$$

and the metric functions A and δ in even powers,

$$A(t, x) = 1 + \epsilon^2 A_2(t, x) + \dots \quad (4.4)$$

$$\delta(t, x) = \epsilon^2 \delta_2(t, x) + \dots \quad (4.5)$$

We choose to work in the boundary gauge, where $\delta(t, \pi/2) = 0$, for reasons that we discuss below.

At linear order, ϕ_1 satisfies

$$\partial_t^2 \phi_1 + \hat{L}\phi_1 = 0 \quad \text{where} \quad \hat{L} \equiv \frac{1}{\mu}(\mu'\partial_x + \mu\partial_x^2) - \frac{m^2}{\cos^2(x)}, \quad (4.6)$$

and $\mu \equiv \tan^{d-1}(x)$. The general solution for (4.6) in the bulk is a linear combination of the eigenfunctions $\Phi_I^\pm(x)$, whose frequencies ω_I are arbitrary. Examining each function's scaling when $x \rightarrow \pi/2$, we see that Φ_I^+ is normalizable and goes as $(\cos x)^{\Delta^+}$ while Φ_I^- is non-normalizable and goes as $(\cos x)^{\Delta^-}$. We denote the positive (negative) root of $\Delta(\Delta - d) = m^2$ as $\Delta^+(\Delta^-)$.

For an arbitrary frequency, requiring regularity at the origin means that we must choose the linear combination [71]

$$E_I(x) = K_I (\cos(x))^{\Delta^+} {}_2F_1\left(\frac{\Delta^+ + \omega_I}{2}, \frac{\Delta^+ - \omega_I}{2}, d/2; \sin^2(x)\right), \quad (4.7)$$

that solves the eigenvalue equation

$$\hat{L}E_I(x) = \omega_I^2 E_I(x). \quad (4.8)$$

For special integer values of the frequencies $\omega_I = \omega_i = 2i + \Delta^+$ with $i \in \mathbb{Z}^+$, the functions $\Phi_i^\pm(x)$ are individually regular at the origin. In this case, the normalizable part of the solution in (4.7) can be written as

$$E_I(x) = e_i(x) = k_i (\cos(x))^{\Delta^+} P_i^{(d/2-1, \Delta^+-d/2)}(\cos(2x)), \quad (4.9)$$

with the Jacobi polynomials $P_n^{(a,b)}(x)$ providing an orthogonal basis so that $\langle e_i(x), e_j(x) \rangle = \delta_{ij}$ when

$$k_i = 2\sqrt{\frac{(i + \Delta^+/2)\Gamma(i + 1)\Gamma(i + \Delta^+)}{\Gamma(i + d/2)\Gamma(i + \Delta^+ - d/2 + 1)}}. \quad (4.10)$$

For consistency with other frequency values, we choose to write the non-normalizable contributions in the general form of (4.7).

The interpretation of the driving term through the AdS/CFT dictionary is the addition of a time-dependent part of the boundary Hamiltonian. Therefore, the presence of non-normalizable modes corresponds to pumping energy in and out of the system. We will find it useful when calculating the third-order source term – which requires a triple sum over first-order modes – to be able to

separate the contributions from either kind of mode. To that end, we write the first-order part of the scalar field as a sum over both normalizable and non-normalizable modes:

$$\begin{aligned}\phi_1(t, x) &= \sum_I c_I(t) E_I(x) \\ &= \sum_j a_j(t) \cos(\omega_i t + b_i(t)) e_j(x) + \sum_\alpha \bar{A}_\alpha \cos(\omega_\alpha t + \bar{B}_\alpha) E_\alpha(x).\end{aligned}\quad (4.11)$$

The values of \bar{A}_α and \bar{B}_α will be set by the driving term. This informs our choice of working in the boundary gauge; the time t is the proper time measured on the boundary, as well as the time scale of oscillations from the driving term. In the simplest example, the driving term on the boundary is a single, periodic function

$$\phi_1(t, \pi/2) = \mathcal{A} \cos \bar{\omega} t. \quad (4.12)$$

In this case, (4.11) collapses into a single term so that

$$\sum_\alpha \bar{A}_\alpha \cos(\omega_\alpha t + \bar{B}_\alpha) E_\alpha(\pi/2) = \mathcal{A} \cos \bar{\omega} t \Rightarrow \bar{A}_{\bar{\omega}} E_{\bar{\omega}}(\pi/2) = \mathcal{A} \quad \text{and} \quad \bar{B}_{\bar{\omega}} = 0. \quad (4.13)$$

Generalizing the boundary condition to a sum over Fourier modes would set further \bar{A}_α and \bar{B}_α to non-zero values.

Without specifying whether frequencies or basis functions have been chosen to be either normalizable or non-normalizable for the time being, we can show that the $\mathcal{O}(\epsilon^3)$ part of the scalar field satisfies the equation

$$\ddot{\phi}_3 + \hat{L}\phi_3 = S = 2(A_2 - \delta_2)\ddot{\phi}_1 + (\dot{A}_2 - \dot{\delta}_2)\dot{\phi}_1 + (A'_2 - \delta'_2)\phi'_1 + m^2 A_2 \phi_1 \sec^2 x. \quad (4.14)$$

Following the steps outlined in appendix 4.A, we project (4.14) onto the basis of normalizable modes since all non-normalizable contributions have been fixed by the $\mathcal{O}(\epsilon)$ boundary condition. Employing a ubiquitous time-dependent solution $c_I(t) = a_I \cos(\omega_I t + b_I) = a_I \cos \theta_I$ with $I \in \{i, \alpha\}$, we find that the source term for the ℓ^{th} mode is

$$\begin{aligned}
S_\ell = & \frac{1}{4} \sum_{\substack{I,J,K \\ K \neq \ell}}^\infty \frac{a_I a_J a_K \omega_K}{\omega_l^2 - \omega_K^2} \left[Z_{IJK\ell}^- (\omega_I + \omega_J - 2\omega_K) \cos(\theta_I + \theta_J - \theta_K) \right. \\
& - Z_{IJK\ell}^- (\omega_I + \omega_J + 2\omega_K) \cos(\theta_I + \theta_J + \theta_K) + Z_{IJK\ell}^+ (\omega_I - \omega_J + 2\omega_K) \cos(\theta_I - \theta_J + \theta_K) \\
& \left. - Z_{IJK\ell}^+ (\omega_I - \omega_J - 2\omega_K) \cos(\theta_I - \theta_J - \theta_K) \right] \\
& + \frac{1}{2} \sum_{\substack{I,J,K \\ I \neq J}}^\infty a_I a_J a_K \omega_J \left(H_{IJK\ell} + m^2 V_{JKI\ell} - 2\omega_K^2 X_{IJK\ell} \right) \left[\frac{1}{\omega_I - \omega_J} (\cos(\theta_I - \theta_J - \theta_K) \right. \\
& + \cos(\theta_I - \theta_J + \theta_K)) - \frac{1}{\omega_I + \omega_J} (\cos(\theta_I + \theta_J - \theta_K) + \cos(\theta_I + \theta_J + \theta_K)) \left. \right] \\
& - \frac{1}{4} \sum_{I,J,K}^\infty a_I a_J a_K \left[(2\omega_J \omega_K X_{IJK\ell} + m^2 V_{IJK\ell}) \cos(\theta_I + \theta_J - \theta_K) \right. \\
& - (2\omega_J \omega_K X_{IJK\ell} - m^2 V_{IJK\ell}) \cos(\theta_I - \theta_J - \theta_K) + (2\omega_J \omega_K X_{IJK\ell} + m^2 V_{IJK\ell}) \cos(\theta_I - \theta_J + \theta_K) \\
& \left. - (2\omega_J \omega_K X_{IJK\ell} - m^2 V_{IJK\ell}) \cos(\theta_I + \theta_J + \theta_K) \right] \\
& + \frac{1}{4} \sum_{I,J}^\infty a_I a_J a_\ell \omega_l \left[\tilde{Z}_{IJ\ell}^- (\omega_I + \omega_J - 2\omega_l) \cos(\theta_I + \theta_J - \theta_\ell) - \tilde{Z}_{IJ\ell}^- (\omega_I + \omega_J + 2\omega_l) \cos(\theta_I + \theta_J + \theta_\ell) \right. \\
& + \tilde{Z}_{IJ\ell}^+ (\omega_I - \omega_J + 2\omega_l) \cos(\theta_I - \theta_J + \theta_\ell) - \tilde{Z}_{IJ\ell}^+ (\omega_I - \omega_J - 2\omega_l) \cos(\theta_I - \theta_J - \theta_\ell) \left. \right] \\
& - \frac{1}{4} \sum_{I,J}^\infty a_I^2 a_J \left[H_{IIJ\ell} + m^2 V_{JII\ell} - 2\omega_J^2 X_{IIJ\ell} \right] (\cos(2\theta_I - \theta_J) + \cos(2\theta_I + \theta_J)) \\
& - \frac{1}{2} \sum_{I,J}^\infty a_I^2 a_J \left[H_{IIJ\ell} + m^2 V_{JII\ell} - 2\omega_J^2 X_{IIJ\ell} + 4\omega_I^2 \omega_J^2 P_{J\ell I} + 2\omega_I^2 (M_{J\ell I} + m^2 Q_{J\ell I}) \right] \cos \theta_J. \quad (4.15)
\end{aligned}$$

Note that sums and restrictions on indices must be interpreted as sums and restrictions on *frequencies* when any of the modes is non-normalizable, since $\omega_\alpha \neq 2\alpha + \Delta^+$ in general.

As mentioned above, the growth of resonant terms with time, i.e. secular growth, at $\mathcal{O}(\epsilon^3)$ can be absorbed into the time-dependent part of the scalar field at that order [59]. Thus, (4.14) tells us that

$$\ddot{c}_\ell^{(3)}(t) + \omega_l^2 c_\ell^{(3)}(t) = S_\ell^{(3)} \cos(\omega_l t + \varphi_\ell), \quad (4.16)$$

where $S_\ell^{(3)}$ is a polynomial in a_I determined by evaluating the resonant contributions from (4.15), and φ_ℓ is some combination of the b_I . To obtain the renormalization flow equations, we can rewrite the amplitudes and phases in terms of renormalized integration constants that exactly cancel the secular terms at each instant. Doing so yields the renormalization flow equations for the

renormalized constants [7]

$$\frac{2\omega_l}{\epsilon^2} \frac{da_\ell}{dt} = -S_\ell^{(3)} \sin(b_\ell - \varphi_\ell) \quad (4.17)$$

$$\frac{2\omega_l a_\ell}{\epsilon^2} \frac{db_\ell}{dt} = -S_\ell^{(3)} \cos(b_\ell - \varphi_\ell) . \quad (4.18)$$

Note that the amplitudes and phases evolve with respect to the “slow time” $\tau = \epsilon^2 t$. In practice, once these flow equations can be written down, the perturbative evolution of the system is determined up to a timescale of $t \sim \epsilon^{-2}$.

To determine the exact form of $S_\ell^{(3)}$, we must consider all combinations of the frequencies $\{\omega_I, \omega_J, \omega_K\}$ that satisfy the resonance condition

$$\omega_I \pm \omega_J \pm \omega_K = \pm \omega_l . \quad (4.19)$$

As an exercise, we first derive the resonant contributions when the boundary source is zero, and therefore only normalizable modes are present. These results agree numerically with previous work on normalizable modes for massless scalars in the interior time gauge ($\delta(t, 0) = 0$) [72]. The definitions of the functions Z , H , X , etc. in (4.15) differ slightly from other works – in part because of the gauge choice, and in part because of a desire to separate out mass-dependent terms – and so are given explicitly in appendix 4.A.

4.4 Resonances From Normalizable Solutions

Consider the case where each of the basis functions are given by normalizable solutions. The possible combinations of frequencies that satisfy (4.19) can be separated into the three distinct cases:

$$\omega_i + \omega_j + \omega_k = \omega_l \quad (+++) \quad (4.20)$$

$$\omega_i - \omega_j - \omega_k = \omega_l \quad (+--) \quad (4.21)$$

$$\omega_i + \omega_j - \omega_k = \omega_l \quad (++-) . \quad (4.22)$$

Note that the $(+++)$ and $(+--)$ resonances produce restrictions on the allowed values of the indices $\{i, j, k\}$, as well as on values of the mass, since $\omega_i = 2i + \Delta^+$. In the first case, the indices are restricted by $i + j + k = \ell - \Delta^+$, and so Δ^+ must be an integer and greater than ℓ for resonance to occur. Similarly, the $(+--)$ resonance condition becomes $i - j - k = \ell + \Delta^+$, which is resonant for any integer value of Δ^+ . We will see that these two resonance channels will non-trivially vanish whenever their respective resonance conditions are satisfied. This is in agreement with the results shown for the massless scalar in the interior time gauge (as they must be, since the choice of time gauge should not change the existence of resonant channels). Here we include the expressions for the naturally vanishing resonances, choosing to explicitly express the mass dependence.

4.4.1 Naturally Vanishing Resonances: (+++) and (+--)

Resonant contributions that come from the condition $\omega_i + \omega_j + \omega_k = \omega_l$ contribute to the total source term via

$$S_\ell = \underbrace{\sum_{i=0}^{\infty} \sum_{j=0}^{\infty} \sum_{k=0}^{\infty}}_{\omega_i + \omega_j + \omega_k = \omega_l} \Omega_{ijkl} a_i a_j a_k \cos(\theta_i + \theta_j + \theta_k) + \dots, \quad (4.23)$$

where the ellipsis denotes other resonances. Ω_{ijkl} is given by

$$\begin{aligned} \Omega_{ijkl} = & -\frac{1}{12} H_{ijkl} \frac{\omega_j(\omega_i + \omega_k + 2\omega_j)}{(\omega_i + \omega_j)(\omega_j + \omega_k)} - \frac{1}{12} H_{ikjl} \frac{\omega_k(\omega_i + \omega_j + 2\omega_k)}{(\omega_i + \omega_k)(\omega_j + \omega_k)} - \frac{1}{12} H_{jikl} \frac{\omega_i(\omega_j + \omega_k + 2\omega_i)}{(\omega_i + \omega_j)(\omega_i + \omega_k)} \\ & - \frac{m^2}{12} V_{ijkl} \left(1 + \frac{\omega_j}{\omega_j + \omega_k} + \frac{\omega_i}{\omega_i + \omega_k} \right) - \frac{m^2}{12} V_{jikl} \left(1 + \frac{\omega_j}{\omega_i + \omega_j} + \frac{\omega_k}{\omega_i + \omega_k} \right) \\ & - \frac{m^2}{12} V_{kijl} \left(1 + \frac{\omega_i}{\omega_i + \omega_j} + \frac{\omega_k}{\omega_j + \omega_k} \right) + \frac{1}{6} \omega_j \omega_k X_{ijkl} \left(1 + \frac{\omega_j}{\omega_i + \omega_k} + \frac{\omega_k}{\omega_i + \omega_j} \right) \\ & + \frac{1}{6} \omega_i \omega_k X_{jkl} \left(1 + \frac{\omega_i}{\omega_j + \omega_k} + \frac{\omega_k}{\omega_i + \omega_j} \right) + \frac{1}{6} \omega_i \omega_j X_{kijl} \left(1 + \frac{\omega_i}{\omega_j + \omega_k} + \frac{\omega_j}{\omega_i + \omega_k} \right) \\ & - \frac{1}{12} Z_{ijkl}^- \left(\frac{\omega_k}{\omega_i + \omega_j} \right) - \frac{1}{12} Z_{ikjl}^- \left(\frac{\omega_j}{\omega_i + \omega_k} \right) - \frac{1}{12} Z_{jikl}^- \left(\frac{\omega_i}{\omega_j + \omega_k} \right). \end{aligned} \quad (4.24)$$

The second naturally vanishing resonance comes from the condition $\omega_i - \omega_j - \omega_k = \omega_l$, and contributes to the total source term via

$$S_\ell = \sum_{j=0}^{\infty} \sum_{k=0}^{\infty} \Gamma_{(j+k+\ell+\Delta^+)jk\ell} a_j a_k a_{(j+k+\ell+\Delta^+)} \cos(\theta_{(j+k+\ell+\Delta^+)} - \theta_j - \theta_k) + \dots, \quad (4.25)$$

where

$$\begin{aligned} \Gamma_{ijkl} = & \frac{1}{4} H_{ijkl} \frac{\omega_j(\omega_k - \omega_i + 2\omega_j)}{(\omega_i - \omega_j)(\omega_j + \omega_k)} + \frac{1}{4} H_{jkl} \frac{\omega_k(\omega_j - \omega_i + 2\omega_k)}{(\omega_i - \omega_k)(\omega_j + \omega_k)} + \frac{1}{4} H_{kijl} \frac{\omega_i(\omega_j + \omega_k - 2\omega_i)}{(\omega_i - \omega_j)(\omega_i - \omega_k)} \\ & - \frac{1}{2} \omega_j \omega_k X_{ijkl} \left(\frac{\omega_k}{\omega_i - \omega_j} + \frac{\omega_j}{\omega_i - \omega_k} - 1 \right) + \frac{1}{2} \omega_i \omega_k X_{jkl} \left(\frac{\omega_k}{\omega_i - \omega_j} + \frac{\omega_i}{\omega_j + \omega_k} - 1 \right) \\ & + \frac{1}{2} \omega_i \omega_j X_{kijl} \left(\frac{\omega_j}{\omega_i - \omega_k} + \frac{\omega_i}{\omega_j + \omega_k} - 1 \right) + \frac{m^2}{4} V_{jkl} \left(\frac{\omega_j}{\omega_i - \omega_j} + \frac{\omega_k}{\omega_i - \omega_k} - 1 \right) \\ & - \frac{m^2}{4} V_{kijl} \left(\frac{\omega_i}{\omega_i - \omega_j} + \frac{\omega_k}{\omega_j + \omega_k} + 1 \right) - \frac{m^2}{4} V_{ijkl} \left(\frac{\omega_i}{\omega_i - \omega_k} + \frac{\omega_j}{\omega_j + \omega_k} + 1 \right) \\ & + \frac{1}{4} Z_{kijl}^- \left(\frac{\omega_i}{\omega_j + \omega_k} \right) - \frac{1}{4} Z_{ijkl}^+ \left(\frac{\omega_k}{\omega_i - \omega_j} \right) - \frac{1}{4} Z_{jkl}^+ \left(\frac{\omega_j}{\omega_i - \omega_k} \right). \end{aligned} \quad (4.26)$$

Building on the work done with massless scalars, we are able to show numerically that (4.24) and (4.26) continue to vanish for massive scalars ($m^2 \geq m_{BF}^2$) in the boundary gauge; thus, the dynamics governing the weakly turbulent transfer of energy are determined only from the remaining resonance channel. When non-normalizable modes are introduced, we will see that naturally vanishing resonances are not present and so the total third-order source term is the sum over all resonant channels.

4.4.2 Non-vanishing Resonance: (+ + -)

The first non-vanishing contributions arise when $\omega_i + \omega_j = \omega_k + \omega_l$. This contribution can be split into three coefficients that are evaluated for certain subsets of the allowed values for the indices, namely

$$S_\ell = T_\ell a_\ell^3 \cos(\theta_\ell + \theta_\ell - \theta_\ell) + \sum_{i \neq \ell}^{\infty} R_{i\ell} a_i^2 a_\ell \cos(\theta_i + \theta_\ell - \theta_i) \\ + \sum_{i \neq \ell}^{\infty} \sum_{j \neq \ell}^{\infty} S_{ij(i+j-\ell)\ell} a_i a_j a_{(i+j-\ell)} \cos(\theta_i + \theta_j - \theta_{i+j-\ell}), \quad (4.27)$$

where the coefficients are given by

$$S_{ijk\ell} = -\frac{1}{4} H_{kij\ell} \frac{\omega_i(\omega_j - \omega_k + 2\omega_i)}{(\omega_i - \omega_k)(\omega_i + \omega_j)} - \frac{1}{4} H_{ijk\ell} \frac{\omega_j(\omega_i - \omega_k + 2\omega_j)}{(\omega_j - \omega_k)(\omega_i + \omega_j)} - \frac{1}{4} H_{jki\ell} \frac{\omega_k(\omega_i + \omega_j - 2\omega_k)}{(\omega_i - \omega_k)(\omega_j - \omega_k)} \\ - \frac{1}{2} \omega_j \omega_k X_{ijk\ell} \left(\frac{\omega_j}{\omega_i - \omega_k} - \frac{\omega_k}{\omega_i + \omega_j} + 1 \right) - \frac{1}{2} \omega_i \omega_k X_{jki\ell} \left(\frac{\omega_i}{\omega_j - \omega_k} - \frac{\omega_k}{\omega_i + \omega_j} + 1 \right) \\ + \frac{1}{2} \omega_i \omega_j X_{kij\ell} \left(\frac{\omega_i}{\omega_j - \omega_k} + \frac{\omega_j}{\omega_i - \omega_k} + 1 \right) - \frac{m^2}{4} V_{ijk\ell} \left(\frac{\omega_i}{\omega_i - \omega_k} + \frac{\omega_j}{\omega_j - \omega_k} + 1 \right) \\ + \frac{m^2}{4} V_{jki\ell} \left(\frac{\omega_k}{\omega_i - \omega_k} - \frac{\omega_j}{\omega_i + \omega_j} - 1 \right) + \frac{m^2}{4} V_{kij\ell} \left(\frac{\omega_k}{\omega_j - \omega_k} - \frac{\omega_i}{\omega_i + \omega_j} - 1 \right) \\ + \frac{1}{4} Z_{ijk\ell}^- \left(\frac{\omega_k}{\omega_i + \omega_j} \right) + \frac{1}{4} Z_{ikj\ell}^+ \left(\frac{\omega_j}{\omega_i - \omega_k} \right) + \frac{1}{4} Z_{jki\ell}^+ \left(\frac{\omega_i}{\omega_j - \omega_k} \right), \quad (4.28)$$

$$R_{i\ell} = \left(\frac{\omega_i^2}{\omega_l^2 - \omega_i^2} \right) (Y_{i\ell\ell i} - Y_{i\ell i\ell} + \omega_l^2 (X_{i\ell i\ell} - X_{\ell i\ell i})) + \left(\frac{\omega_i^2}{\omega_l^2 - \omega_i^2} \right) (H_{\ell i\ell i} + m^2 V_{i\ell\ell\ell} - 2\omega_i^2 X_{\ell i\ell i}) \\ - \left(\frac{\omega_l^2}{\omega_l^2 - \omega_i^2} \right) (H_{i\ell i\ell} + m^2 V_{\ell i\ell i} - 2\omega_i^2 X_{i\ell i\ell}) - \frac{m^2}{4} (V_{i\ell i\ell} + V_{i\ell\ell\ell}) + \omega_i^2 \omega_l^2 (P_{i\ell i\ell} - 2P_{\ell i\ell i}) \\ - \omega_i \omega_l X_{i\ell i\ell} - \frac{3m^2}{2} V_{\ell i\ell i} - \frac{1}{2} H_{i\ell\ell\ell} + \omega_l^2 B_{i\ell i\ell} - \omega_i^2 M_{\ell i\ell i} - m^2 \omega_i^2 Q_{\ell i\ell i}, \quad (4.29)$$

and

$$T_\ell = \frac{1}{2} \omega_l^2 (X_{\ell\ell\ell\ell} + 4B_{\ell\ell\ell\ell} - 2M_{\ell\ell\ell\ell} - 2m^2 Q_{\ell\ell\ell\ell}) - \frac{3}{4} (H_{\ell\ell\ell\ell} + 3m^2 V_{\ell\ell\ell\ell}). \quad (4.30)$$

Following the form of (4.17) - (4.18), these resonant terms set the evolution of the renormalized integration coefficients to be [11]

$$\frac{2\omega_l}{\epsilon^2} \frac{da_\ell}{dt} = - \sum_{i \neq \ell}^{\infty} \sum_{j \neq \ell}^{\infty} S_{ij(i+j-\ell)\ell} a_i a_j a_{(i+j-\ell)} \sin(b_\ell + b_{(i+j-\ell)} - b_i - b_j), \quad (4.31)$$

$$\frac{2\omega_l a_\ell}{\epsilon^2} \frac{db_\ell}{dt} = -T_\ell a_\ell^3 - \sum_{i \neq \ell}^{\infty} R_{i\ell} a_i^2 a_\ell \\ - \sum_{i \neq \ell}^{\infty} \sum_{j \neq \ell}^{\infty} S_{ij(i+j-\ell)\ell} a_i a_j a_{(i+j-\ell)} \cos(b_\ell + b_{(i+j-\ell)} - b_i - b_j). \quad (4.32)$$

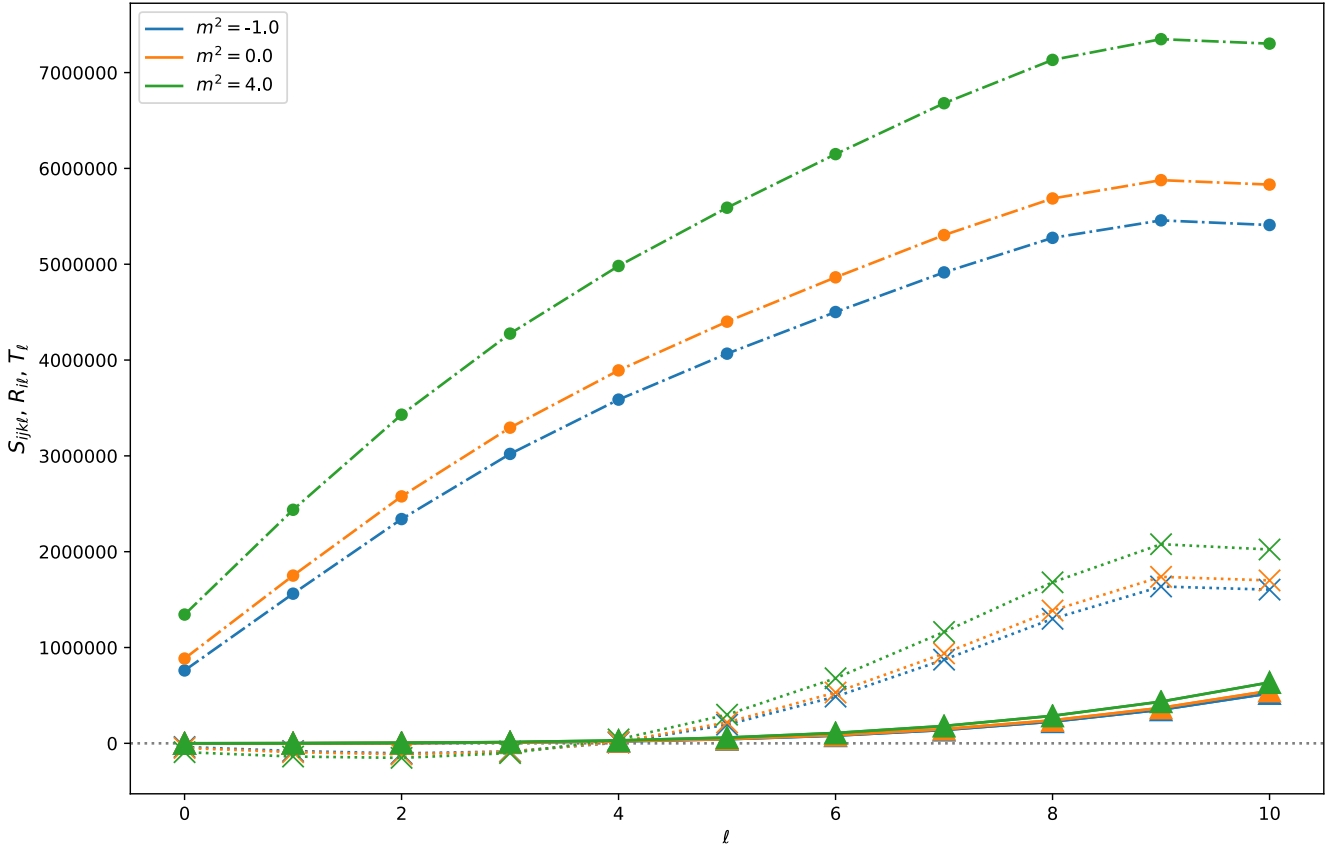


Figure 4.1: Evaluating (4.28)-(4.30) over different values of m^2 for $\ell \leq 10$. $S_{ij(i+j-\ell)\ell}$ is denoted by filled circles connected by dash-dotted lines; $R_{i\ell}$ is denoted by filled triangles connected by solid lines; T_ℓ is denoted by large Xs connected by dotted lines. Different values of m^2 are denoted by the colour of each series.

To examine the effects of non-zero masses on R , S , and T , we evaluate (4.28)-(4.30) for tachyonic, massless, and massive scalars in figure 4.1. The result is a vertical shift in the coefficient value that is proportional to the choice of mass-squared. By inspection, there is an indication that this shift increases with increasing ℓ values; however, a numerical fit of the data would be needed to claim this definitively.

4.5 Resonances From Non-normalizable Modes

Now let us consider the excitation of non-normalizable modes by a driving term on the boundary of AdS. Having set ω_l to be a normalizable mode, we may ask what restrictions exist on our choices for the other frequencies, $\{\omega_i, \omega_j, \omega_k\}$. Aside from the trivial case where all modes are normalizable, we could imagine that one of the modes is non-normalizable. However, this would violate the resonance condition (4.19); thus, at least two modes must be non-normalizable. When three non-normalizable modes exist, there are two possibilities: first, that any combination of generically non-integer frequencies gives a non-integer value and so does not contribute a secular term when

projected onto the ω_ℓ basis; second, some particular combination of the non-normalizable frequencies gives an integer frequency, in which case there are resonant contributions to $S_\ell^{(3)}$. Therefore, the pertinent question is what resonances are possible when two of $\{\omega_i, \omega_j, \omega_k\}$ are non-normalizable? Because this choice breaks some of the symmetries that contributed to the previous expressions for resonance channels, the resonance conditions must be re-examined starting from the source expression (4.15).

Before proceeding further, an important consideration is what the effect of non-normalizable modes are on the perturbative expansion that leads to the source equations. Since non-normalizable solutions do not have well-defined norms, we do not know *a priori* that the inner products described in appendix 4.A are still finite. To investigate this, consider the generic expression for the second-order metric function

$$A_2 = -\nu \int_0^x dy \mu \left((\dot{\phi}_1)^2 + (\phi'_1)^2 + m^2 \phi_1^2 \sec^2 x \right), \quad (4.33)$$

in the limit of $x \rightarrow \pi/2$, and let the scalar field ϕ_1 be given by a generic superposition of normalizable and non-normalizable eigenfunctions as in (4.11). Ignoring the time-dependent contributions, we find that

$$\lim_{\tilde{x} \rightarrow 0} A_2(\tilde{x} \equiv \pi/2 - x) = \tilde{x}^{-\xi} \left(\frac{2\tilde{x}^{2+d}}{2-\xi} - \frac{\tilde{x}^d (1 + (\Delta^-)^2)}{\xi} \right), \quad (4.34)$$

where we have defined $\xi = \sqrt{d^2 + 4m^2}$. In the massless case, $\xi = d$ and all powers of \tilde{x} are non-negative; thus, the limit is finite. For tachyonic masses, $m_{BF}^2 < m^2 < 0$ so that $0 < \xi < d$ and the limit is again finite. However, when $m^2 > 0$, part of the limit diverges. In order for the boundary to remain asymptotically AdS, counter-terms in the bulk action would be required to cancel such divergences – a case we will not address presently. Furthermore, for masses that saturate the Breitenlohner-Freedman bound, the limit would have to be re-evaluated. We will therefore restrict our discussion to $m_{BF}^2 < m^2 \leq 0$ to avoid these issues. A similar check on the near-boundary behaviour of δ_2 shows that the gauge condition $\delta_2(t, \pi/2) = 0$ remains unchanged by the addition of non-normalizable modes given the same restrictions on the mass of the scalar field. With these restrictions in mind, let us now examine the resonances produced by the activation of non-normalizable modes.

4.5.1 Two Non-normalizable Modes with Equal Frequencies

As a first case, let us assume that the two non-normalizable modes have equal, constant, and arbitrary frequencies, $\bar{\omega}$ (and therefore amplitudes $\bar{A}_{\bar{\omega}}$). The resonance condition (4.19) will only be satisfied when one of $\{\omega_I, \omega_J, \omega_K\}$ are normalizable. In particular, we find that the following combinations are resonant:

$$\omega_i - \omega_j + \omega_k - \omega_l = 0 \quad \Rightarrow \quad \text{either } \omega_i \text{ or } \omega_k \text{ is normalizable} \quad (4.35)$$

$$\omega_i + \omega_j - \omega_k - \omega_l = 0 \quad \Rightarrow \quad \text{either } \omega_i \text{ or } \omega_j \text{ is normalizable} \quad (4.36)$$

$$\omega_i - \omega_j - \omega_k + \omega_l = 0 \quad \Rightarrow \quad \text{either } \omega_j \text{ or } \omega_k \text{ is normalizable.} \quad (4.37)$$

When any of these resonance conditions is met, the remaining normalizable mode will have a frequency equal to ω_l , collapsing all sums over frequencies so that

$$S_\ell = \bar{T}_\ell a_\ell \bar{A}_{\bar{\omega}}^2 \cos(\theta_\ell) + \dots , \quad (4.38)$$

where the amplitudes of the non-normalizable modes $\bar{A}_{\bar{\omega}}$ are set by the choice of boundary condition. Collecting the appropriate terms in (4.15) and evaluating each possible resonance, we find that

$$\begin{aligned} \bar{T}_\ell = & \left[\frac{1}{2} Z_{\ell\bar{\omega}\omega\ell}^- \left(\frac{\bar{\omega}}{\omega_l + \bar{\omega}} \right) + \frac{1}{2} Z_{\ell\bar{\omega}\omega\ell}^+ \left(\frac{\bar{\omega}}{\omega_l - \bar{\omega}} \right) + H_{\ell\bar{\omega}\omega\ell} \left(\frac{\bar{\omega}^2}{\omega_l^2 - \bar{\omega}^2} \right) - H_{\bar{\omega}\ell\omega\ell} \left(\frac{\omega_l^2}{\omega_l^2 - \bar{\omega}^2} \right) \right. \\ & - m^2 V_{\ell\bar{\omega}\omega\ell} \left(\frac{\omega_l^2}{\omega_l^2 - \bar{\omega}^2} \right) + m^2 V_{\bar{\omega}\omega\ell\ell} \left(\frac{\bar{\omega}^2}{\omega_l^2 - \bar{\omega}^2} \right) + 2X_{\omega\omega\ell\ell} \left(\frac{\bar{\omega}^2 \omega_l^2}{\omega_l^2 - \bar{\omega}^2} \right) - 2X_{\ell\ell\bar{\omega}\bar{\omega}} \left(\frac{\bar{\omega}^4}{\omega_l^2 - \bar{\omega}^2} \right) \Big]_{\bar{\omega} \neq \omega_l} \\ & + \omega_l^2 X_{\bar{\omega}\omega\ell\ell} - \bar{\omega}^2 X_{\ell\ell\bar{\omega}\bar{\omega}} - \frac{3}{2} m^2 V_{\ell\ell\bar{\omega}\bar{\omega}} - \frac{1}{2} m^2 V_{\bar{\omega}\omega\ell\ell} - \frac{1}{2} H_{\bar{\omega}\omega\ell\ell} + \omega_l^2 \tilde{Z}_{\bar{\omega}\omega\ell}^+ - 2\bar{\omega}^2 \omega_l^2 P_{\ell\ell\bar{\omega}} \\ & - \bar{\omega}^2 (\omega_l^2 P_{\ell\ell\bar{\omega}} - B_{\ell\ell\bar{\omega}}) . \end{aligned} \quad (4.39)$$

Notice that the terms in the square braces only contribute when $\bar{\omega} \neq \omega_l$. Beginning from (4.15), only terms in the square braces that are proportional to Z^\pm are limited in this way; the remaining terms have no such restriction. However, it can be shown that integral functions with permuted indices are equal when the non-normalizable frequency equals the normalizable frequency. Upon simplification, factors of $\omega_l^2 - \bar{\omega}^2$ are cancelled, and the overall contribution to T_ℓ from the terms in the braces is zero. Thus, these terms are grouped with those that have natural restrictions on the indices.

With the resonant contributions determined, the renormalization flow equations for two equal, constant, non-normalizable frequencies follow from (4.17) - (4.18) and are

$$\frac{2\omega_l}{\epsilon^2} \frac{da_\ell}{dt} = 0 \quad \text{and} \quad \frac{2\omega_l a_\ell}{\epsilon^2} \frac{db_\ell}{dt} = -\bar{T}_\ell a_\ell \bar{A}_{\bar{\omega}}^2 . \quad (4.40)$$

Qualitatively, we see that instead of both the amplitude and the phase running with respect to τ , only the phase changes in time. Indeed, (4.40) tells us that b_ℓ is a linear function of τ with a slope that is determined by the $\mathcal{O}(\epsilon^3)$ physics encapsulated by \bar{T}_ℓ .

Other resonant contributions become possible for more restrictive values of the non-normalizable frequency, such as if $\bar{\omega}$ is allowed to be an integer. These contributions are denoted by the ellipsis in (4.38) and are listed in appendix 4.B. In figures 4.2 and 4.3, we evaluate (4.39) for $\ell < 10$ over a variety of $\bar{\omega}$ values first for a massless scalar, then for a tachyonic scalar. For both values of mass-squared, T_ℓ demonstrates power law-type behaviour as a function of ℓ with a leading coefficient that is proportional to the non-normalizable frequency $\bar{\omega}$. We also see that the limit of (4.39) as $\bar{\omega} \rightarrow \omega_0$ is well-defined in both cases.

4.5.2 Special Values of Non-normalizable Frequencies

Let us now consider special values of non-normalizable frequencies that will lead to a greater number of resonance channels. While general non-normalizable frequencies do not require any such restrictions, we will find it informative to examine these special cases as they possess more symmetry in index/frequency values than the case of equal non-normalizable frequencies, but less than all-normalizable modes.

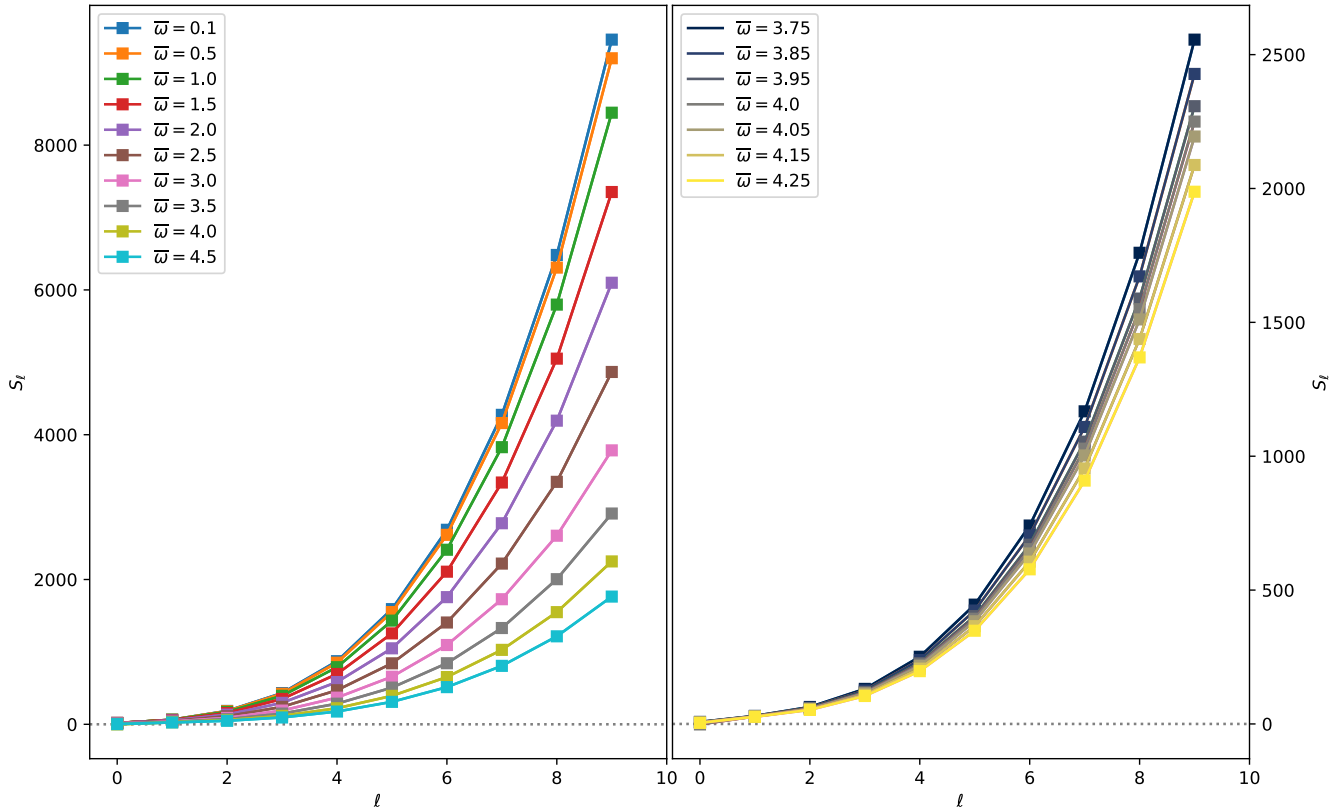


Figure 4.2: Left: Evaluating (4.39) when $m^2 = 0$ for various choices of $\bar{\omega}$. Right: The behaviour of S_ℓ for $\bar{\omega}$ values near ω_0 .

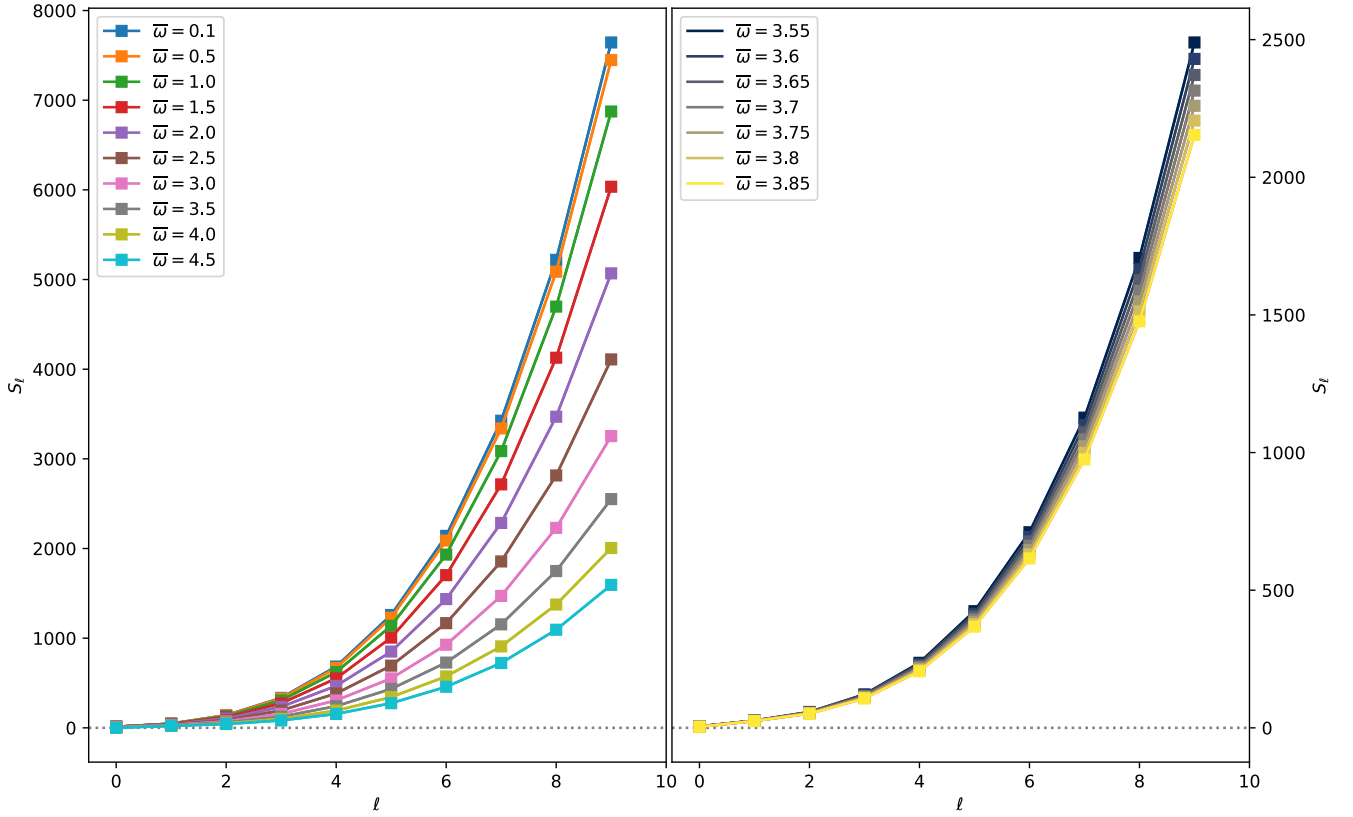


Figure 4.3: Left: Evaluating \bar{T}_ℓ for a tachyon with $m^2 = -1.0$. Right: The behaviour of S_ℓ near $\omega_0 = \Delta^+ \approx 3.7$.

4.5.2.1 Add to an integer

First, we choose two of the modes to be non-normalizable with frequencies $\bar{\omega}_1$ and $\bar{\omega}_2$ that add to give an integer: $\bar{\omega}_1 + \bar{\omega}_2 = 2n$ where $n = 1, 2, 3, \dots$ (note that the $n = 0$ case means that both $\bar{\omega}_1$ and $\bar{\omega}_2$ would need to be zero by the positive-frequency requirement and so would not contribute). Furthermore, either frequency need not be an integer and therefore the difference $|\bar{\omega}_1 - \bar{\omega}_2|$ will, in general, not be an integer. In § 4.5.3, we examine the case when the difference of non-normalizable frequencies is an integer.

When we consider possible resonance channels, we see that resonances can be grouped into

$$(++) : \omega_i + 2n = \omega_\ell \quad \forall \ell \geq n \quad (4.41)$$

$$(+-) : \omega_i - 2n = \omega_\ell \quad \forall n \quad (4.42)$$

for any $m_{BF}^2 < m^2 < 0$. However, for a massless scalar, we have an additional channel

$$(-+) : -\omega_i + 2n = \omega_\ell \quad \forall n \geq \ell + d. \quad (4.43)$$

Adding the channels together, the total source term is

$$\begin{aligned}
S_\ell = & \sum_{\bar{\omega}_1 + \bar{\omega}_2 = 2n} \left[\Theta(n - \ell - d) \bar{R}_{(n-\ell-d)\ell}^{(-+)} \bar{A}_1 \bar{A}_2 a_{(n-\ell-d)} \cos(\theta_{(n-\ell-d)} - \theta_1 - \theta_2) \right]_{m^2=0} \\
& + \sum_{\bar{\omega}_1 + \bar{\omega}_2 = 2n} \Theta(\ell - n) \bar{R}_{(\ell-n)\ell}^{(++)} \bar{A}_1 \bar{A}_2 a_{(\ell-n)} \cos(\theta_{(\ell-n)} + \theta_1 + \theta_2) \\
& + \sum_{\bar{\omega}_1 + \bar{\omega}_2 = 2n} \bar{R}_{(\ell+n)\ell}^{(+)} \bar{A}_1 \bar{A}_2 a_{(\ell+n)} \cos(\theta_{(\ell+n)} - \theta_1 - \theta_2) \\
& + \bar{T}_\ell \bar{A}_1 \bar{A}_2 a_\ell \cos(\theta_\ell)
\end{aligned} \tag{4.44}$$

where the Heaviside step function $\Theta(x)$ enforces the restrictions on the indices in (4.41) and (4.43) and $\theta_1 = \bar{\omega}_1 t + \bar{B}_1$, etc.

In the following expressions, the sum over all $\bar{\omega}_1, \bar{\omega}_2$ such that $\bar{\omega}_1 + \bar{\omega}_2 = 2n$ is implied, and only the restrictions on individual frequencies are included. Examining each channel in (4.44) individually, we find

$$\begin{aligned}
\bar{R}_{i\ell}^{(++)} = & -\frac{1}{4} \sum_{\bar{\omega}_2 \neq \omega_l} \frac{\bar{\omega}_2}{\omega_l - \bar{\omega}_2} Z_{i12\ell}^- - \frac{1}{4} \sum_{\bar{\omega}_1 \neq \omega_l} \frac{\bar{\omega}_1}{\omega_l - \bar{\omega}_1} Z_{i21\ell}^- - \frac{1}{8n} (\omega_l - 2n) Z_{12i\ell}^- \\
& - \frac{1}{4} \sum_{\omega_i \neq \bar{\omega}_1} \frac{1}{\omega_l - \bar{\omega}_2} \left[\bar{\omega}_1 (H_{i12\ell} + m^2 V_{12i\ell} - 2\bar{\omega}_2^2 X_{i12\ell}) + (\omega_l - 2n) (H_{1i2\ell} + m^2 V_{i21\ell} - 2\bar{\omega}_2^2 X_{1i2\ell}) \right] \\
& - \frac{1}{4} \sum_{\omega_i \neq \bar{\omega}_2} \frac{1}{\omega_l - \bar{\omega}_1} \left[\bar{\omega}_2 (H_{i21\ell} + m^2 V_{21i\ell} - 2\bar{\omega}_1^2 X_{i21\ell}) + (\omega_l - 2n) (H_{2i1\ell} + m^2 V_{i12\ell} - 2\bar{\omega}_1^2 X_{2i1\ell}) \right] \\
& - \frac{1}{8n} \sum_{\bar{\omega}_1 \neq \bar{\omega}_2} \left[\bar{\omega}_1 H_{21i\ell} + \bar{\omega}_2 H_{12i\ell} + m^2 (\bar{\omega}_1 V_{1i2\ell} + \bar{\omega}_2 V_{2i1\ell}) - (\omega_l - 2n)^2 (\bar{\omega}_1 X_{21i\ell} + \bar{\omega}_2 X_{12i\ell}) \right] \\
& + \frac{1}{2} \left[\bar{\omega}_1 \bar{\omega}_2 X_{i12\ell} + (\omega_l - 2n) (\bar{\omega}_1 X_{21i\ell} + \bar{\omega}_2 X_{12i\ell}) - \frac{m^2}{2} (V_{i12\ell} + V_{i21\ell} + V_{12i\ell}) \right]. \tag{4.45}
\end{aligned}$$

The notation $X_{i12\ell}$ corresponds to evaluating X_{ijkl} with $\omega_j = \bar{\omega}_1$ and $\omega_k = \bar{\omega}_2$. Next, we find that

$$\begin{aligned}
\bar{R}_{i\ell}^{(+)} = & -\frac{1}{4} \left[\frac{(\omega_l + 2n)}{2n} Z_{12i\ell}^- + 2(\omega_l + 2n) (\bar{\omega}_1 X_{21i\ell} + \bar{\omega}_2 X_{12i\ell}) \right. \\
& - \frac{\bar{\omega}_1}{(\omega_l + \bar{\omega}_2)} (H_{i12\ell} + m^2 V_{12i\ell} - 2\bar{\omega}_2^2 X_{i12\ell}) + \frac{(\omega_l + 2n)}{(\omega_l + \bar{\omega}_2)} (H_{1i2\ell} + m^2 V_{i21\ell} - 2\bar{\omega}_2^2 X_{1i2\ell}) \\
& - \frac{\bar{\omega}_2}{(\omega_l + \bar{\omega}_1)} (H_{i21\ell} + m^2 V_{21i\ell} - 2\bar{\omega}_1^2 X_{i21\ell}) + \frac{(\omega_l + 2n)}{(\omega_l + \bar{\omega}_1)} (H_{2i1\ell} + m^2 V_{i12\ell} - 2\bar{\omega}_1^2 X_{2i1\ell}) \\
& \left. - 2\bar{\omega}_1 \bar{\omega}_2 X_{i12\ell} + m^2 (V_{12i\ell} + V_{i12\ell} + V_{i21\ell}) \right] + \frac{1}{4} \sum_{\bar{\omega}_2 \neq \omega_l} \frac{\bar{\omega}_1 \bar{\omega}_2 (\omega_l + 2n)}{\omega_l + \bar{\omega}_2} (X_{21i\ell} - X_{\ell i12}) \\
& + \frac{1}{4} \sum_{\bar{\omega}_1 \neq \omega_l} \frac{\bar{\omega}_1 \bar{\omega}_2 (\omega_l + 2n)}{\omega_l + \bar{\omega}_1} (X_{12i\ell} - X_{\ell i12}). \tag{4.46}
\end{aligned}$$

When $m^2 = 0$, we have contributions from

$$\begin{aligned}
\bar{R}_{i\ell}^{(-+)} &= \frac{1}{4} \sum_{\bar{\omega}_2 \neq \omega_l} \frac{\bar{\omega}_2}{\omega_l - \bar{\omega}_2} Z_{i12\ell}^+ + \frac{1}{4} \sum_{\bar{\omega}_1 \neq \omega_l} \frac{\bar{\omega}_1}{\omega_l - \bar{\omega}_1} Z_{i21\ell}^+ + \frac{1}{4} \sum_{i \neq \ell} \left(\frac{2n - \omega_l}{2n} \right) Z_{12i\ell}^- \\
&+ \frac{1}{4} \sum_{\bar{\omega}_1 \neq \omega_i} \frac{1}{\omega_i - \bar{\omega}_1} \left[\bar{\omega}_1 (H_{i12\ell} - 2\bar{\omega}_2^2 X_{i12\ell}) - (2n - \omega_l) (H_{1i2\ell} - 2\bar{\omega}_2^2 X_{1i2\ell}) \right] \\
&+ \frac{1}{4} \sum_{\bar{\omega}_2 \neq \omega_i} \frac{1}{\omega_i - \bar{\omega}_2} \left[\bar{\omega}_2 (H_{i21\ell} - 2\bar{\omega}_1^2 X_{i21\ell}) - (2n - \omega_l) (H_{2i1\ell} - 2\bar{\omega}_1^2 X_{2i1\ell}) \right] \\
&- \frac{1}{8n} \sum_{\bar{\omega}_1 \neq \bar{\omega}_2} \left[\bar{\omega}_1 H_{21i\ell} + \bar{\omega}_2 H_{12i\ell} - 2(2n - \omega_l)^2 (\bar{\omega}_1 X_{21i\ell} + \bar{\omega}_2 X_{12i\ell}) \right] \\
&- \frac{1}{2} \left[(2n - \omega_l) (\bar{\omega}_1 X_{21i\ell} + \bar{\omega}_2 X_{12i\ell}) - \bar{\omega}_1 \bar{\omega}_2 X_{i12\ell} \right]. \tag{4.47}
\end{aligned}$$

NB. In (4.47) only, $\omega_i = 2i + \Delta^+ = 2i + d$ since this term requires that $m^2 = 0$ to contribute. We maintain the same notation out of convenience, despite the special case. Finally,

$$\begin{aligned}
\bar{T}_\ell &= \frac{1}{2} \omega_l^2 \left(\tilde{Z}_{11\ell}^+ + \tilde{Z}_{22\ell}^+ \right) - \frac{1}{2} \left[H_{11\ell\ell} + H_{22\ell\ell} + m^2 (V_{\ell11\ell} + V_{\ell22\ell}) - 2\omega_l^2 (X_{11\ell\ell} + X_{22\ell\ell}) \right. \\
&\quad \left. + 4\omega_l^2 (\bar{\omega}_1^2 P_{\ell\ell 1} + \bar{\omega}_2^2 P_{\ell\ell 2}) + 2\bar{\omega}_1^2 M_{\ell\ell 1} + 2\bar{\omega}_2^2 M_{\ell\ell 2} + 2m^2 (\bar{\omega}_1^2 Q_{\ell\ell 1} + \bar{\omega}_2^2 Q_{\ell\ell 2}) \right]. \tag{4.48}
\end{aligned}$$

In figure 4.4, we compute the total source term (modulo the amplitudes a_i and \bar{A}_α) for a tachyonic scalar with $n = 2$. Figure 4.5 provides a comparison between the value of the source term for a massless scalar between two choices of n : one that includes contributions from $\bar{R}_{i\ell}^{(-+)}$ and one that does not. As expected, the source terms are symmetric in $\bar{\omega}_1 \leftrightarrow \bar{\omega}_2$, hence only $\bar{\omega}_1 \leq n$ data are shown. As a function of ℓ , (4.44) starts near zero before becoming increasingly negative as ℓ becomes large. As a check for naturally vanishing channels, the absolute value of the sum of S_ℓ is also plotted; however, there is no indication that any channel vanishes for any of the $\bar{\omega}_1, \bar{\omega}_2$ values considered.

The renormalization flow equations include the sum of all the channels (none of which vanish naturally), and are

$$\begin{aligned}
\frac{2\omega_l}{\epsilon^2} \frac{da_\ell}{dt} &= - \sum_{\bar{\omega}_1 + \bar{\omega}_2 = 2n} \left[\Theta(n - \ell - d) \bar{R}_{(n-\ell-d)\ell}^{(-+)} \bar{A}_1 \bar{A}_2 a_{(n-\ell-d)} \sin(b_{(n-\ell-d)} - \bar{B}_1 - \bar{B}_2) \right]_{m^2=0} \\
&- \sum_{\bar{\omega}_1 + \bar{\omega}_2 = 2n} \Theta(\ell - n) \bar{R}_{(\ell-n)\ell}^{(++)} \bar{A}_1 \bar{A}_2 a_{(\ell-n)} \sin(b_{(\ell-n)} + \bar{B}_1 + \bar{B}_2) \\
&- \sum_{\bar{\omega}_1 + \bar{\omega}_2 = 2n} \bar{R}_{(\ell+n)\ell}^{(+-)} \bar{A}_1 \bar{A}_2 a_{(\ell+n)} \sin(b_{(\ell+n)} - \bar{B}_1 - \bar{B}_2), \tag{4.49}
\end{aligned}$$

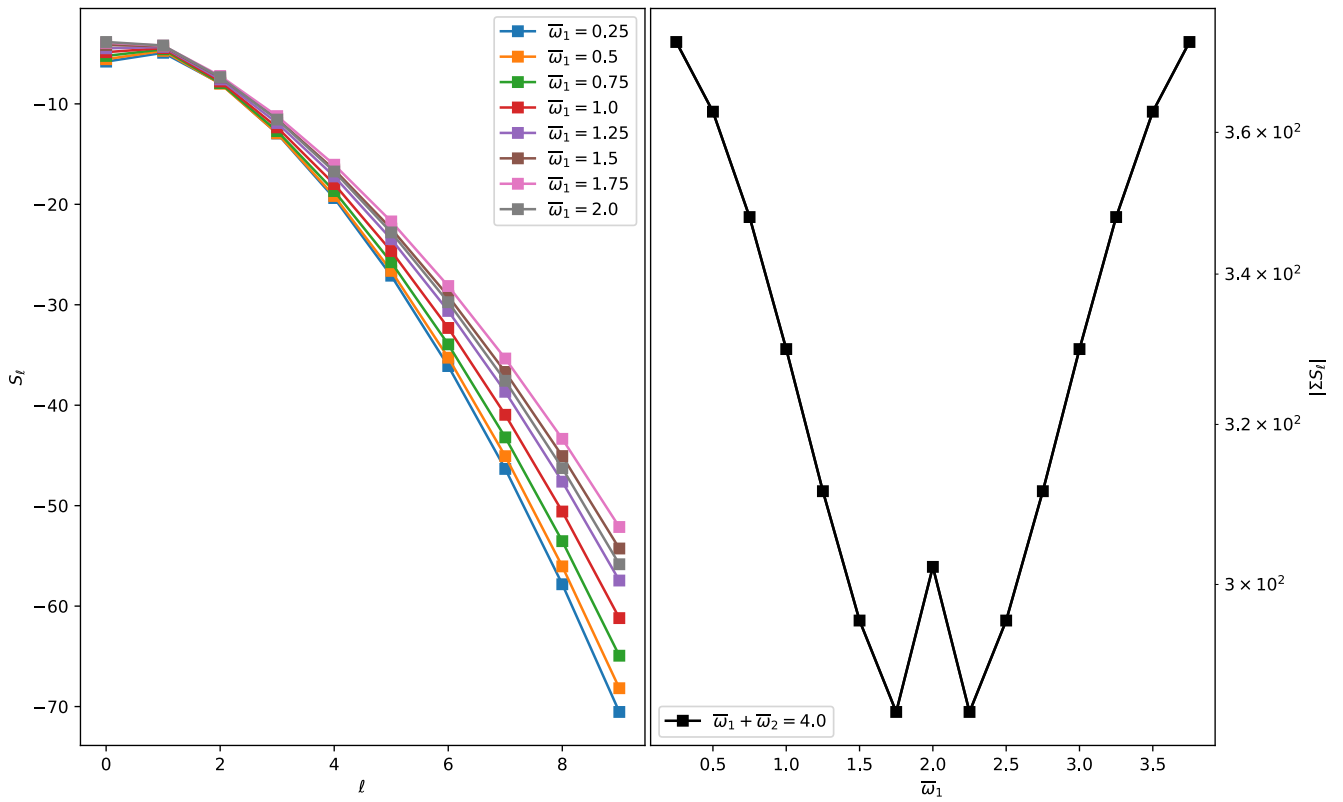


Figure 4.4: Left: Source term values for a tachyonic scalar with $m^2 = -1.0$ when the frequencies of non-normalizable modes sum to 4.0. Right: The absolute value of the sum of the source terms for each choice of $\bar{\omega}_1$, $\bar{\omega}_2$.

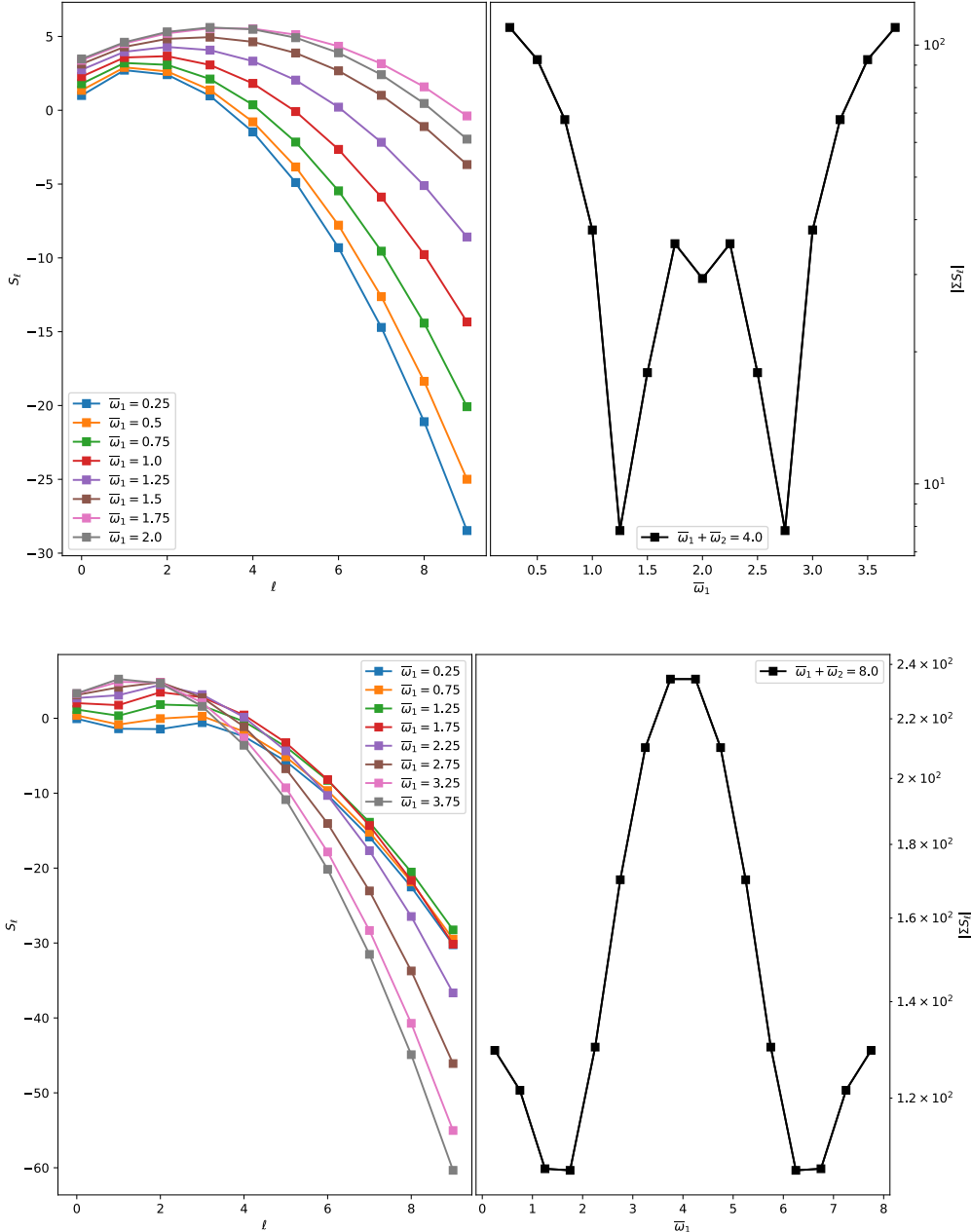


Figure 4.5: Above: The value of (4.44) as a function of ℓ for a massless scalar with values of $\bar{\omega}_1$ and $\bar{\omega}_2$ chosen so that $\bar{\omega}_1 + \bar{\omega}_2 = 4$. Below: The same plot but with values chosen to satisfy $\bar{\omega}_1 + \bar{\omega}_2 = 8$.

and

$$\begin{aligned} \frac{2\omega_l a_\ell}{\epsilon^2} \frac{db_\ell}{dt} = & - \sum_{\bar{\omega}_1 + \bar{\omega}_2 = 2n} \left[\Theta(n - \ell - d) \bar{R}_{(n-\ell-d)\ell}^{(-+)} \bar{A}_1 \bar{A}_2 a_{(n-\ell-d)} \cos(b_{(n-\ell-d)} - \bar{B}_1 - \bar{B}_2) \right]_{m^2=0} \\ & - \sum_{\bar{\omega}_1 + \bar{\omega}_2 = 2n} \Theta(\ell - n) \bar{R}_{(\ell-n)\ell}^{(++)} \bar{A}_1 \bar{A}_2 a_{(\ell-n)} \cos(b_{(\ell-n)} + \bar{B}_1 + \bar{B}_2) \\ & - \sum_{\bar{\omega}_1 + \bar{\omega}_2 = 2n} \bar{R}_{(\ell+n)\ell}^{(+-)} \bar{A}_1 \bar{A}_2 a_{(\ell+n)} \cos(b_{(\ell+n)} - \bar{B}_1 - \bar{B}_2) - \bar{T}_\ell \bar{A}_1 \bar{A}_2 a_\ell. \end{aligned} \quad (4.50)$$

4.5.3 Integer Plus χ

Finally, let us consider the case where the non-normalizable frequencies are non-integer, but differ from integer values by a set amount. In analogue to the case where all modes are normalizable, we consider the non-normalizable frequencies to be shifted away from integer values by

$$\omega_\gamma = 2\gamma + \chi, \quad (4.51)$$

where $\gamma \in \mathbb{Z}^+$ (greek letters are chosen to differentiate these non-normalizable modes from normalizable modes with integer frequencies, which use roman letters). We furthermore limit χ to be non-integer¹ and set $m^2 = 0$ throughout. For this choice of non-normalizable frequencies there are no resonant contributions from the all-plus channel, unlike the naturally vanishing resonance found in § 4.4.1. Only when either $\omega_i + \omega_\gamma = \omega_\beta - \omega_l$, or $\omega_i + \omega_\gamma = \omega_\beta + \omega_l$ with $i + \gamma \geq \ell$, are resonant terms present. Let us examine each case separately.

4.5.3.1 $\omega_i + \omega_\gamma = \omega_\beta - \omega_l$

When the resonance condition $\omega_i + \omega_\gamma = \omega_\beta - \omega_l$ is met, the contribution to the source term is of the form

$$S_\ell = \sum_{i \neq \ell} \sum_{\gamma \neq \beta} \bar{S}_{i(i+\gamma+\ell)\gamma\ell}^{(1)} a_i \bar{A}_{(i+\gamma+\ell)} \bar{A}_\gamma \cos(\theta_i - \theta_{(i+\gamma+\ell)} + \theta_\gamma) \\ + \sum_{\beta} \bar{R}_{\beta\ell}^{(1)} a_\ell \bar{A}_\beta^2 \cos(\theta_\ell + \theta_\beta - \theta_\beta) + \dots, \quad (4.52)$$

where

$$\bar{S}_{i\beta\gamma\ell}^{(1)} = \frac{1}{4} H_{\beta\gamma i\ell} \frac{\omega_\gamma(\omega_i - \omega_\beta + 2\omega_\gamma)}{(\omega_\beta - \omega_\gamma)(\omega_i + \omega_\gamma)} - \frac{1}{4} H_{\gamma\beta i\ell} \frac{\omega_\beta(\omega_i + \omega_\gamma - 2\omega_\beta)}{(\omega_i - \omega_\beta)(\omega_\beta - \omega_\gamma)} - \frac{1}{4} H_{\gamma i\beta\ell} \frac{\omega_i(\omega_\gamma - \omega_\beta + 2\omega_i)}{(\omega_i - \omega_\beta)(\omega_i + \omega_\gamma)} \\ + \frac{1}{2} \omega_i \omega_\gamma X_{\beta\gamma i\ell} \left(\frac{\omega_\gamma}{\omega_i - \omega_\beta} - \frac{\omega_i}{\omega_\beta + \omega_\gamma} + 1 \right) + \frac{1}{2} \omega_i \omega_\beta X_{\gamma\beta i\ell} \left(\frac{\omega_i}{\omega_\beta - \omega_\gamma} + \frac{\omega_\beta}{\omega_i + \omega_\gamma} - 1 \right) \\ + \frac{1}{2} \omega_\beta \omega_\gamma X_{i\beta\gamma\ell} \left(\frac{\omega_\beta}{\omega_i + \omega_\gamma} - \frac{\omega_\gamma}{\omega_i - \omega_\beta} - 1 \right) - \frac{1}{4} Z_{\beta\gamma i\ell}^+ \left(\frac{\omega_i}{\omega_i + \omega_l} \right) \\ + \frac{1}{4} Z_{i\gamma\beta\ell}^- \left(\frac{\omega_\beta}{\omega_l - \omega_\beta} \right) + \frac{1}{4} Z_{i\beta\gamma\ell}^+ \left(\frac{\omega_\gamma}{\omega_l + \omega_\gamma} \right), \quad (4.53)$$

and

$$\bar{R}_{\beta\ell}^{(1)} = \frac{1}{4} Z_{\ell\beta\beta\ell}^- \left(\frac{\omega_\beta}{\omega_l + \omega_\beta} \right) + \frac{1}{4} Z_{\ell\beta\beta\ell}^+ \left(\frac{\omega_\beta}{\omega_l - \omega_\beta} \right) + \frac{1}{2} H_{\ell\beta\beta\ell} \left(\frac{\omega_\beta^2}{\omega_l^2 - \omega_\beta^2} \right) - \frac{1}{2} H_{\beta\ell\beta\ell} \left(\frac{\omega_l^2}{\omega_l^2 - \omega_\beta^2} \right) \\ + X_{\beta\ell\beta\ell} \left(\frac{\omega_l^4}{\omega_l^2 - \omega_\beta^2} \right) - \frac{1}{2} \omega_\beta^2 X_{\ell\beta\beta\ell} \left(\frac{\omega_l^2 + \omega_\beta^2}{\omega_l^2 - \omega_\beta^2} \right) - \frac{1}{2} H_{\ell\beta\beta\ell} + \omega_l^2 \tilde{Z}_{\beta\beta\ell}^+ - 2\omega_\beta^2 \omega_l^2 P_{\ell\ell\beta} - \omega_\beta^2 M_{\ell\ell\beta}. \quad (4.54)$$

¹Indeed, for integer values of χ , the sum or difference of two non-normalizable modes could be an integer. This would either be covered by the work in § 4.5.2.1, or be a slight variation of it.

4.5.3.2 $\omega_i + \omega_\gamma = \omega_\beta + \omega_l$

Similarly, when the resonance condition $\omega_i + \omega_\gamma = \omega_\beta + \omega_l$ is met, the contribution to the source term is

$$S_\ell = \underbrace{\sum_{i \neq \ell} \sum_{\gamma \neq \beta} \overline{S}_{i(i+\gamma-\ell)\gamma\ell}^{(2)} a_i \bar{A}_{(i+\gamma-\ell)} \bar{A}_\gamma \cos(\theta_i - \theta_{(i+\gamma-\ell)} + \theta_\gamma)}_{i+\gamma \geq \ell} + \sum_\beta \overline{R}_{\beta\ell}^{(2)} a_\ell \bar{A}_\beta^2 \cos(\theta_\ell + \theta_\beta - \theta_\beta) + \dots, \quad (4.55)$$

where

$$\begin{aligned} \overline{S}_{i\beta\gamma\ell}^{(2)} &= \frac{1}{4} H_{\beta\gamma i\ell} \frac{\omega_\gamma(\omega_i - \omega_\beta)}{(\omega_\beta - \omega_\gamma)(\omega_i - \omega_\gamma)} - \frac{1}{4} H_{\gamma\beta i\ell} \frac{\omega_\beta(\omega_l - \omega_\beta)}{(\omega_\beta - \omega_\gamma)(\omega_i - \omega_\beta)} + \frac{1}{4} H_{\beta i\gamma\ell} \frac{\omega_i(\omega_\gamma - \omega_\beta)}{(\omega_i - \omega_\beta)(\omega_i - \omega_\gamma)} \\ &+ \frac{1}{2} \omega_i \omega_\gamma X_{\beta\gamma i\ell} \left(\frac{\omega_\gamma}{\omega_i - \omega_\beta} - \frac{\omega_i}{\omega_\beta - \omega_\gamma} + 1 \right) + \frac{1}{2} \omega_i \omega_\beta X_{\gamma\beta i\ell} \left(\frac{\omega_i}{\omega_\beta - \omega_\gamma} - \frac{\omega_\beta}{\omega_i - \omega_\gamma} - 1 \right) \\ &+ \frac{1}{2} \omega_\beta \omega_\gamma X_{i\beta\gamma\ell} \left(\frac{\omega_\beta}{\omega_i - \omega_\gamma} - \frac{\omega_\gamma}{\omega_i - \omega_\beta} - 1 \right) + \frac{1}{4} Z_{i\gamma\beta\ell}^- \left(\frac{\omega_\beta}{\omega_l + \omega_\beta} \right) \\ &+ \frac{1}{4} Z_{i\beta\gamma\ell}^+ \left(\frac{\omega_\gamma}{\omega_l - \omega_\gamma} \right) - \frac{1}{4} Z_{\beta\gamma i\ell}^+ \left(\frac{\omega_i}{\omega_i - \omega_l} \right), \end{aligned} \quad (4.56)$$

and

$$\begin{aligned} \overline{R}_{\beta\ell}^{(2)} &= \frac{1}{4} Z_{\ell\beta\beta\ell}^- \left(\frac{\omega_\beta}{\omega_l + \omega_\beta} \right) + \frac{1}{4} Z_{\ell\beta\beta\ell}^+ \left(\frac{\omega_\beta}{\omega_l - \omega_\beta} \right) + \frac{1}{2} H_{\ell\beta\beta\ell} \left(\frac{\omega_\beta^2}{\omega_l^2 - \omega_\beta^2} \right) - \frac{1}{2} H_{\beta\ell\beta\ell} \left(\frac{\omega_l^2}{\omega_l^2 - \omega_\beta^2} \right) \\ &+ X_{\beta\beta\ell\ell} \left(\frac{\omega_l^2}{\omega_l^2 - \omega_\beta^2} \right) + \frac{1}{2} \omega_\beta^2 X_{\ell\beta\beta\ell} \left(\frac{\omega_l^2 + \omega_\beta^2}{\omega_l^2 - \omega_\beta^2} \right) - \frac{1}{2} H_{\beta\beta\ell\ell} + \omega_l^2 \tilde{Z}_{\beta\beta\ell}^+ - 2\omega_\beta^2 \omega_l^2 P_{\ell\ell\beta} - \omega_\beta^2 M_{\ell\ell\beta}. \end{aligned} \quad (4.57)$$

Unlike the case with all normalizable modes where two of the three resonance channels naturally vanished, both of the resonant channels contribute when the non-normalizable modes have frequencies given by (4.51). Therefore, the renormalization flow equations will contain contributions from both channels:

$$\begin{aligned} \frac{2\omega_l}{\epsilon^2} \frac{da_\ell}{dt} &= - \sum_{i \neq \ell} \sum_{\gamma \neq \beta} \overline{S}_{i(i+\gamma+\ell)\gamma\ell}^{(1)} a_i \bar{A}_{(i+\gamma+\ell)} \bar{A}_\gamma \sin(b_\ell + \bar{B}_{(i+\gamma+\ell)} - b_i - \bar{B}_\gamma) \\ &- \underbrace{\sum_{i \neq \ell} \sum_{\gamma \neq \beta} \overline{S}_{i(i+\gamma-\ell)\gamma\ell}^{(2)} a_i \bar{A}_{(i+\gamma-\ell)} \bar{A}_\gamma \sin(b_\ell + \bar{B}_{(i+\gamma-\ell)} - b_i - \bar{B}_\gamma)}_{i+\gamma \geq \ell}, \end{aligned} \quad (4.58)$$

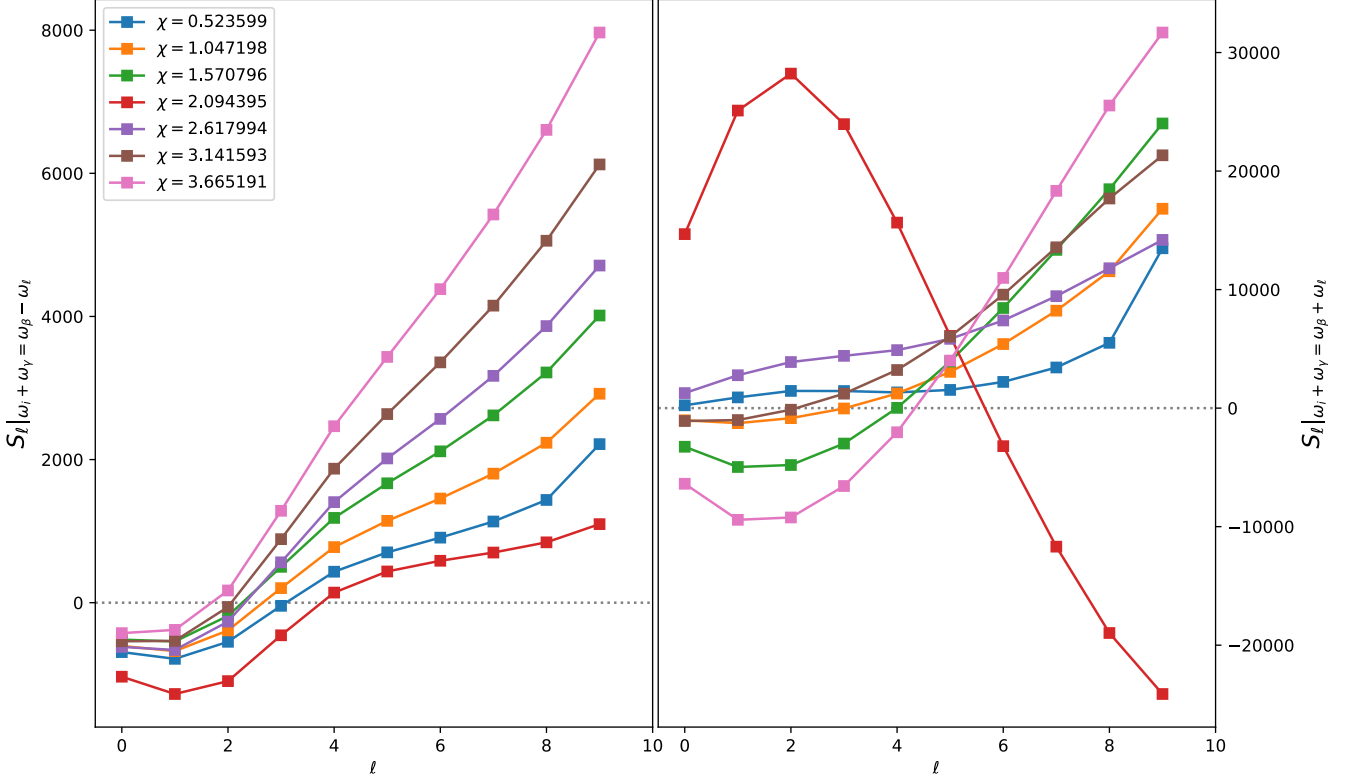


Figure 4.6: Left: Evaluating the source term (4.52) for various values of χ for $\ell < 10$. Right: Evaluating the source term (4.55) subject to $i + \gamma \geq \ell$ for the same values of χ and the same range of ℓ .

$$\begin{aligned} \frac{2\omega_l a_\ell}{\epsilon^2} \frac{db_\ell}{dt} = & - \sum_{\beta} \bar{R}_{\beta\ell}^{(1)} a_\ell \bar{A}_\beta^2 - \sum_{\beta} \bar{R}_{\beta\ell}^{(2)} a_\ell \bar{A}_\beta^2 \\ & - \sum_{i \neq \ell} \sum_{\gamma \neq \beta} \bar{S}_{i(i+\gamma+\ell)\gamma\ell}^{(1)} a_i \bar{A}_{(i+\gamma+\ell)} \bar{A}_\gamma \cos(b_\ell + \bar{B}_{(i+\gamma+\ell)} - b_i - \bar{B}_\gamma) \\ & - \underbrace{\sum_{i \neq \ell} \sum_{\gamma \neq \beta} \bar{S}_{i(i+\gamma-\ell)\gamma\ell}^{(2)} a_i \bar{A}_{(i+\gamma-\ell)} \bar{A}_\gamma \cos(b_\ell + \bar{B}_{(i+\gamma-\ell)} - b_i - \bar{B}_\gamma)}_{i+\gamma \geq \ell}. \end{aligned} \quad (4.59)$$

In figure 4.6, we evaluate both resonant contributions channels' and plot their contributions for various values of χ . In particular, we examine the values $\chi \in \{\pi/6, \dots, 7\pi/6\}$. Again, there is no indication of any channel vanishing naturally. Interestingly, both sources demonstrate anomalous behaviour when $\chi \sim 2$ for reasons that are not immediately clear. The source term (4.52) is generally more positive for larger χ except for $\chi = 2\pi/3$, which is translated negatively with respect to the source terms produced by other χ values. Again, when (4.55) is evaluated for $\chi = 2\pi/3$, the result differs significantly from other choices of χ : seemingly reflected through the x axis with respect to other results. The significance of the choice $\chi = 2\pi/3 \sim d/2$ is possibly explained by the non-normalizable modes being *nearly* equal to the normalizable ones. In this event, S_ℓ would contain additional terms, such as those present in § 4.4. The departure of the $\chi = 2\pi/3$ data from other data sets is perhaps a signal of these missing resonances.

4.6 Discussion

We have seen that the inclusion of a time-dependent boundary term in the holographic dual of a quantum quench allows energy to enter the bulk spacetime through coupling with non-normalizable modes. The dynamics of the weakly turbulent energy cascades that trigger instability were captured by secular terms at third-order that could not be removed by frequency shifts alone. Using the Two-Time Formalism, we have determined the renormalization group flow equations for the slowly varying amplitudes and phases that are tuned to cancel the secular terms that give rise to instability.

Unlike when only normalizable modes are considered, the introduction of non-normalizable modes results in no naturally vanishing resonance channels for the frequencies considered. The flow equations for a_ℓ and b_ℓ are now linear, since the non-normalizable amplitudes and phases are set by the first-order boundary condition and thus remain constant. In practice, this means the evolution of the system will be different than in the case where only normalizable modes are activated. Furthermore, periodic pumping of energy into and out of the bulk theory will undoubtably add interesting dynamics to the evolution already observed for quasi-periodic solutions with static boundary conditions [73].

With the renormalization flow equations established, future work will examine whether equilibrium solutions can be derived. Then, general non-collapsing solutions will be constructed out of perturbations of the equilibrium solutions and their numerical evolution will be examined. Comparisons to established numerical pumped solutions in the full theory may be instructive in understanding the space of stable and nearly-stable data.

Properties of the boundary CFT can also be determined from the perturbative theory in the bulk. For instance, the AdS/CFT dictionary relates the leading coefficient of the normalizable modes of the scalar field at the boundary to the expectation value of an operator $\langle \mathcal{O}_\phi \rangle$; the leading part of the non-normalizable modes are related to a time-dependent driving term in the boundary Hamiltonian $s(t)$. The Ward identity for time translations gives the time dependence of the energy density in the CFT in terms of these quantities

$$\partial_t \langle T_{tt} \rangle = -\partial_t s(t) \langle \mathcal{O}_\phi \rangle. \quad (4.60)$$

The evolution of the energy density can then be examined via the slowly varying amplitude and phase variables and compared with fully numeric results.

Acknowledgments The author would like to thank A. R. Frey for their guidance and insight with this project. This work is supported by the Natural Sciences and Engineering Research Council of Canada's Discovery Grant program.

Appendix

4.A Derivation of Source Terms For Massive Scalars

The derivation of the general expression for the $\mathcal{O}(\epsilon^3)$ source term for massive scalars closely follows the massless case, particularly if one chooses not to write out the explicit mass dependence as was done in [72]. However, since we have chosen to write our equations in a slightly different way – and in a different gauge – than previous authors, one may find it instructive to see the differences in the derivations. Below we have included the intermediate steps involved in deriving the third-order source term S_ℓ .

Continuing the expansion of the equations of motion in powers of ϵ , we see that the backreaction between the metric and the scalar field appears at second order in the perturbation,

$$A'_2 = -\mu\nu \left[(\dot{\phi}_1)^2 + (\phi'_1)^2 + m^2 \phi_1^2 \sec^2 x \right] + \nu' A_2 / \nu, \quad (4.61)$$

which can be directly integrated to give

$$A_2 = -\nu \int_0^x dy \mu \left((\dot{\phi}_1)^2 + (\phi'_1)^2 + m^2 \phi_1^2 \sec^2 x \right). \quad (4.62)$$

For convenience, we have also defined the functions

$$\mu(x) = (\tan x)^{d-1} \quad \text{and} \quad \nu(x) = (d-1)/\mu'. \quad (4.63)$$

Similarly, the first non-trivial contribution to the lapse (in the boundary time gauge) is

$$\delta_2 = \int_x^{\pi/2} dy \mu \nu \left((\dot{\phi}_1)^2 + (\phi'_1)^2 \right). \quad (4.64)$$

Projecting each of the terms in (4.14) individually onto the eigenbasis $\{e_\ell\}$ will involve evaluating inner products involving multiple integrals. To aide in evaluating these expressions, it is useful to derive several identities. First, from the equation for the scalar field's time-dependent coefficients c_i ,

$$\ddot{c}_i + \omega_i^2 c_i = 0 \quad \Rightarrow \quad \partial_t (\dot{c}_i^2 + \omega_i^2 c_i^2) = \partial_t \mathbb{C}_i = 0. \quad (4.65)$$

Next, from the definition of \hat{L} ,

$$\hat{L} e_j = -\frac{1}{\mu} (\mu e'_j)' + m^2 \sec^2 x e_j \quad \Rightarrow \quad (\mu e'_j)' = \mu (m^2 \sec^2 x - \omega_j^2) e_j. \quad (4.66)$$

By considering the expression $(\mu e'_i e_j)'$, we see that

$$(\mu e'_i e_j)' = (m^2 \sec^2 x - \omega_i^2) \mu e_i e_j + \mu e'_i e'_j, \quad (4.67)$$

which, after permuting i, j and subtracting from above, gives

$$\frac{[\mu(e'_i e_j \omega_j^2 - e_i e'_j \omega_i^2)]'}{(\omega_j^2 - \omega_i^2)} = \mu m^2 \sec^2 x e_i e_j + \mu e'_i e'_j. \quad (4.68)$$

Using these identities, we evaluate each of the inner products and find that

$$\begin{aligned} \langle \delta_2 \ddot{\phi}_1, e_\ell \rangle &= - \sum_{i=0}^{\infty} \sum_{j=0}^{\infty} \sum_{\substack{k=0 \\ k \neq \ell}}^{\infty} \frac{\omega_k^2 c_k}{\omega_l^2 - \omega_k^2} [\dot{c}_i \dot{c}_j (X_{k\ell ij} - X_{\ell kij}) + c_i c_j (Y_{ij\ell k} - Y_{ijk\ell})] \\ &\quad - \sum_{i=0}^{\infty} \sum_{j=0}^{\infty} \omega_j^2 c_\ell [\dot{c}_i \dot{c}_j P_{ij\ell} + c_i c_j B_{ij\ell}], \end{aligned} \quad (4.69)$$

$$\begin{aligned} \langle A_2 \ddot{\phi}_1, e_\ell \rangle &= 2 \sum_{i=0}^{\infty} \sum_{\substack{j=0 \\ i \neq j}}^{\infty} \sum_{k=0}^{\infty} \frac{\omega_k^2 c_k}{\omega_j^2 - \omega_i^2} X_{ijk\ell} (\dot{c}_i \dot{c}_j + \omega_j^2 c_i c_j) \\ &\quad + \sum_{i=0}^{\infty} \sum_{j=0}^{\infty} \omega_j^2 c_j (\mathbb{C}_i P_{j\ell i} + c_i^2 X_{iij\ell}), \end{aligned} \quad (4.70)$$

$$\begin{aligned} \langle \dot{\delta}_2 \dot{\phi}_1, e_\ell \rangle &= \sum_{i=0}^{\infty} \sum_{j=0}^{\infty} \sum_{\substack{k=0 \\ k \neq \ell}}^{\infty} \frac{\dot{c}_k}{\omega_l^2 - \omega_k^2} [\partial_t (\dot{c}_i \dot{c}_j) (X_{k\ell ij} - X_{\ell kij}) + \partial_t (c_i c_j) (Y_{ij\ell k} - Y_{ijk\ell})] \\ &\quad + \sum_{i=0}^{\infty} \sum_{j=0}^{\infty} \dot{c}_\ell [\partial_t (\dot{c}_i \dot{c}_j) P_{ij\ell} + \partial_t (c_i c_j) B_{ij\ell}], \end{aligned} \quad (4.71)$$

$$\langle \dot{A}_2 \dot{\phi}_1, e_\ell \rangle = -2 \sum_{i=0}^{\infty} \sum_{j=0}^{\infty} \sum_{k=0}^{\infty} \dot{c}_k \dot{c}_j c_i X_{ijk\ell}, \quad (4.72)$$

$$\begin{aligned} \langle (A'_2 - \delta'_2) \phi'_1, e_\ell \rangle &= -2 \sum_{i=0}^{\infty} \sum_{\substack{j=0 \\ i \neq j}}^{\infty} \sum_{k=0}^{\infty} \frac{c_k (\dot{c}_i \dot{c}_j + \omega_j^2 c_i c_j)}{\omega_j^2 - \omega_i^2} H_{ijk\ell} - m^2 \sum_{i=0}^{\infty} \sum_{j=0}^{\infty} \sum_{k=0}^{\infty} c_i c_j c_k V_{ijk\ell} \\ &\quad - \sum_{i=0}^{\infty} \sum_{j=0}^{\infty} c_j [c_i^2 H_{iij\ell} + \mathbb{C}_i M_{j\ell i}], \end{aligned} \quad (4.73)$$

$$\begin{aligned} \langle A_2 \phi_1 \sec^2 x, e_\ell \rangle &= -2 \sum_{i=0}^{\infty} \sum_{\substack{j=0 \\ i \neq j}}^{\infty} \sum_{k=0}^{\infty} \frac{c_k (\dot{c}_i \dot{c}_j + \omega_j^2 c_i c_j)}{\omega_j^2 - \omega_i^2} V_{jk\ell i} \\ &\quad - \sum_{i=0}^{\infty} \sum_{j=0}^{\infty} c_j (c_i^2 V_{ji\ell i} + \mathbb{C}_i Q_{j\ell i}), \end{aligned} \quad (4.74)$$

where the forms of X, Y, V, H, B, M, P, and Q are given by

$$X_{ijkl} = \int_0^{\pi/2} dx \mu^2 \nu e'_i e'_j e'_k e'_\ell \quad (4.75)$$

$$Y_{ijkl} = \int_0^{\pi/2} dx \mu^2 \nu e'_i e'_j e'_k e'_\ell \quad (4.76)$$

$$V_{ijkl} = \int_0^{\pi/2} dx \mu^2 \nu e_i e_j e'_k e_\ell \sec^2 x \quad (4.77)$$

$$H_{ijkl} = \int_0^{\pi/2} dx \mu^2 \nu' e'_i e'_j e'_k e'_\ell \quad (4.78)$$

$$B_{ij\ell} = \int_0^{\pi/2} dx \mu \nu e'_i e'_j \int_0^x dy \mu e_\ell^2 \quad (4.79)$$

$$M_{ij\ell} = \int_0^{\pi/2} dx \mu \nu' e'_i e_j \int_0^x dy \mu e_\ell^2 \quad (4.80)$$

$$P_{ij\ell} = \int_0^{\pi/2} dx \mu \nu e_i e_j \int_0^x dy \mu e_\ell^2 \quad (4.81)$$

$$Q_{ij\ell} = \int_0^{\pi/2} dx \mu \nu e_i e_j \sec^2 x \int_0^x dy \mu e_\ell^2. \quad (4.82)$$

Note that, using integration by parts to remove the derivative from ν in the definitions of H_{ijkl} and $M_{ij\ell}$, we can show that

$$H_{ijkl} = \omega_i^2 X_{kij\ell} + \omega_k^2 X_{ijkl} - Y_{ij\ell k} - Y_{\ell k j i} - m^2 V_{k j i \ell} - m^2 V_{ijkl}, \quad (4.83)$$

$$M_{ij\ell} = \omega_i^2 P_{ij\ell} - B_{ij\ell} - m^2 Q_{ij\ell}. \quad (4.84)$$

Collecting (4.69) - (4.74) gives the expression for $S_\ell = \langle S, e_\ell \rangle$:

$$\begin{aligned} S_\ell &= \sum_{\substack{i,j,k \\ k \neq \ell}}^{\infty} \frac{1}{\omega_l^2 - \omega_k^2} \left[F_k(\dot{c}_i \dot{c}_j) (X_{k\ell ij} - X_{\ell k ij}) + F_k(c_i c_j) (Y_{ij\ell k} - Y_{ijk\ell}) \right] \\ &\quad + 2 \sum_{\substack{i,j,k \\ i \neq j}}^{\infty} \frac{c_k D_{ij}}{\omega_j^2 - \omega_i^2} \left[2\omega_k^2 X_{ijkl} - H_{ijkl} - m^2 V_{jkil} \right] - \sum_{i,j,k}^{\infty} c_i \left[2\dot{c}_j \dot{c}_k X_{ijkl} + m^2 c_j c_k V_{ijkl} \right] \\ &\quad + \sum_{i,j}^{\infty} \left[F_\ell(\dot{c}_i \dot{c}_j) P_{ij\ell} + F_\ell(c_i c_j) B_{ij\ell} + 2\omega_j^2 c_j (c_i^2 X_{iij\ell} + \mathbb{C}_i P_{j\ell i}) \right. \\ &\quad \left. - c_j (c_i^2 (H_{iij\ell} + m^2 V_{jiil}) + \mathbb{C}_i (M_{j\ell i} + m^2 Q_{j\ell i})) \right], \end{aligned} \quad (4.85)$$

where $F_k(z) = \dot{c}_k \dot{z} - 2\omega_k^2 c_k z$, $D_{ij} = \dot{c}_i \dot{c}_j + \omega_j^2 c_i c_j$, and $\mathbb{C}_i = \dot{c}_i^2 + \omega_i^2 c_i^2$. Additionally, we have combined some integrals into their own expressions, namely

$$Z_{ijkl}^\pm = \omega_i \omega_j (X_{k\ell ij} - X_{\ell k ij}) \pm (Y_{ij\ell k} - Y_{ijk\ell}) \quad \text{and} \quad \tilde{Z}_{ij\ell}^\pm = \omega_i \omega_j P_{ij\ell} \pm B_{ij\ell}. \quad (4.86)$$

Finally, using the solution for the time-dependent coefficients, $c_i(t) = a_i(t) \cos(\omega_i t + b_i(t)) \equiv a_i \cos \theta_i$, we arrive at (4.15).

4.B Two Non-normalizable Modes with Equal Frequencies

Let us return to the case of two, equal, non-normalizable modes with frequency $\bar{\omega}$. Within the space of resonant frequency values, there are frequencies that happen to satisfy $\bar{\omega} = \omega_l$ numerically and may produce extra resonances subject to restrictions on the normalizable frequency. These instances were excluded from the discussion in § 4.5.1, and we address them here. When considering special integer values of $\bar{\omega}$ each choice of $\bar{\omega}$ below will contribute a \bar{T} -type term to the total source:

$$\bar{T}_i^{(1)} : \quad \omega_i = \omega_l + 2\bar{\omega} \quad \forall \bar{\omega} \in \mathbb{Z}^+ \quad (4.87)$$

$$\bar{T}_i^{(2)} : \quad \omega_i = \omega_l - 2\bar{\omega} \quad \forall \bar{\omega} \in \mathbb{Z}^+ \text{ such that } \ell \geq \bar{\omega} \quad (4.88)$$

$$\bar{T}_i^{(3)} : \quad \omega_i = 2\bar{\omega} - \omega_l \quad \forall \bar{\omega} \in \mathbb{Z}^+ \text{ such that } \bar{\omega} \leq \ell + \Delta^+, \quad (4.89)$$

with $\omega_i \neq \omega_l$ in each case. These special values contribute to the case of two, equal non-normalizable modes via

$$S_\ell = \bar{A}_{\bar{\omega}}^2 \bar{T}_{(\ell+\bar{\omega})}^{(1)} a_{(\ell+\bar{\omega})} \cos(\theta_{(\ell+\bar{\omega})} - 2\bar{\omega}t) + \bar{A}_{\bar{\omega}}^2 \bar{T}_{(\ell-\bar{\omega})}^{(2)} a_{(\ell-\bar{\omega})} \cos(\theta_{(\ell-\bar{\omega})} + 2\bar{\omega}t) + \bar{A}_{\bar{\omega}}^2 \bar{T}_{(\bar{\omega}-\ell-\Delta^+)}^{(3)} a_{(\bar{\omega}-\ell-\Delta^+)} \cos(2\bar{\omega}t - \theta_{(\bar{\omega}-\ell-\Delta^+)}) \quad (4.90)$$

under their respective conditions on the value of $\bar{\omega}$. The total resonant contribution for all possible $\bar{\omega}$ values is the addition of (4.90) and (4.38). Evaluating (4.15) in each case of the cases described by (4.87) - (4.89), we find that

$$\begin{aligned} \bar{T}_i^{(1)} &= \frac{1}{2} \left[H_{i\bar{\omega}\omega\ell} \left(\frac{\bar{\omega}}{\omega_i - \bar{\omega}} \right) - H_{\bar{\omega}i\bar{\omega}\ell} \left(\frac{\omega_i}{\omega_i - \bar{\omega}} \right) + m^2 V_{\bar{\omega}\bar{\omega}\omega\ell} \left(\frac{\bar{\omega}}{\omega_i - \bar{\omega}} \right) \right. \\ &\quad \left. - m^2 V_{i\bar{\omega}\omega\ell} \left(\frac{\omega_i}{\omega_i - \bar{\omega}} \right) - 2\bar{\omega}^2 X_{i\bar{\omega}\omega\ell} \left(\frac{\bar{\omega}}{\omega_i - \bar{\omega}} \right) + 2\bar{\omega}^2 X_{\bar{\omega}i\bar{\omega}\ell} \left(\frac{\omega_i}{\omega_i - \bar{\omega}} \right) \right]_{\omega_i \neq \bar{\omega}} \\ &\quad - \frac{1}{2} \left[Z_{i\bar{\omega}\omega\ell}^+ \left(\frac{\bar{\omega}}{\omega_l + \bar{\omega}} \right) \right]_{\omega_l \neq \bar{\omega}} + \frac{1}{4} Z_{\bar{\omega}\bar{\omega}\omega\ell}^- \left(\frac{\omega_l + 2\bar{\omega}}{2\bar{\omega}} \right) + \frac{1}{2} \bar{\omega}^2 X_{i\bar{\omega}\omega\ell} - \frac{m^2}{4} V_{\bar{\omega}\bar{\omega}\omega\ell} \\ &\quad - \bar{\omega} \omega_i X_{\bar{\omega}\bar{\omega}\omega\ell} - \frac{m^2}{2} V_{i\bar{\omega}\omega\ell}, \end{aligned} \quad (4.91)$$

$$\begin{aligned} \bar{T}_i^{(2)} &= -\frac{1}{2} \left[H_{i\bar{\omega}\omega\ell} \left(\frac{\bar{\omega}}{\omega_i + \bar{\omega}} \right) + H_{\bar{\omega}i\bar{\omega}\ell} \left(\frac{\omega_i}{\omega_i + \bar{\omega}} \right) + m^2 V_{\bar{\omega}\bar{\omega}\omega\ell} \left(\frac{\bar{\omega}}{\omega_i + \bar{\omega}} \right) \right. \\ &\quad \left. + m^2 V_{i\bar{\omega}\omega\ell} \left(\frac{\omega_i}{\omega_i + \bar{\omega}} \right) - 2\bar{\omega}^2 X_{i\bar{\omega}\omega\ell} \left(\frac{\bar{\omega}}{\omega_i + \bar{\omega}} \right) - 2\bar{\omega}^2 X_{\bar{\omega}i\bar{\omega}\ell} \left(\frac{\omega_i}{\omega_i + \bar{\omega}} \right) \right]_{\omega_i \neq \bar{\omega}} \\ &\quad - \frac{1}{2} \left[Z_{i\bar{\omega}\omega\ell}^- \left(\frac{\bar{\omega}}{\omega_l - \bar{\omega}} \right) \right]_{\omega_l \neq \bar{\omega}} - \frac{1}{4} Z_{\bar{\omega}\bar{\omega}\omega\ell}^- \left(\frac{\omega_l - 2\bar{\omega}}{\bar{\omega}} \right) + \frac{1}{2} \bar{\omega}^2 X_{i\bar{\omega}\omega\ell} + \frac{m^2}{4} V_{\bar{\omega}\bar{\omega}\omega\ell} \\ &\quad + \bar{\omega} \omega_i X_{\bar{\omega}\bar{\omega}\omega\ell} + \frac{m^2}{2} V_{i\bar{\omega}\omega\ell}, \end{aligned} \quad (4.92)$$

and

$$\begin{aligned}
\overline{T}_i^{(3)} = & \frac{1}{2} \left[H_{i\bar{\omega}\bar{\omega}\ell} \left(\frac{\bar{\omega}}{\omega_i - \bar{\omega}} \right) - H_{\bar{\omega}i\bar{\omega}\ell} \left(\frac{\omega_i}{\omega_i - \bar{\omega}} \right) + m^2 V_{\bar{\omega}\bar{\omega}i\ell} \left(\frac{\bar{\omega}}{\omega_i - \bar{\omega}} \right) \right. \\
& - m^2 V_{i\bar{\omega}\bar{\omega}\ell} \left(\frac{\omega_i}{\omega_i - \bar{\omega}} \right) - 2\bar{\omega}^2 X_{i\bar{\omega}\bar{\omega}\ell} \left(\frac{\bar{\omega}}{\omega_i - \bar{\omega}} \right) + 2\omega_i^2 X_{\bar{\omega}\bar{\omega}i\ell} \left(\frac{\bar{\omega}}{\omega_i - \bar{\omega}} \right) \\
& \left. - Z_{i\bar{\omega}\bar{\omega}\ell}^+ \left(\frac{\bar{\omega}}{\omega_i - \bar{\omega}} \right) \right]_{\omega_i \neq \bar{\omega}} + \frac{1}{4} Z_{\bar{\omega}\bar{\omega}i\ell}^- \left(\frac{2\bar{\omega} - \omega_l}{2\bar{\omega}} \right) + \frac{1}{2} \bar{\omega}^2 X_{i\bar{\omega}\bar{\omega}\ell} - \frac{m^2}{4} V_{\bar{\omega}\bar{\omega}i\ell} \\
& - \bar{\omega} \omega_i X_{\bar{\omega}\bar{\omega}i\ell} - \frac{m^2}{2} V_{i\bar{\omega}\bar{\omega}\ell}.
\end{aligned} \tag{4.93}$$

These resonance channels can then be added into the right hand side of the equation for da_ℓ/dt in (4.40).

5 Conclusion

Conclusions go here.

Bibliography

- [1] P. Bizon and A. Rostworowski, *On weakly turbulent instability of anti-de Sitter space*, *Phys. Rev. Lett.* **107** (2011) 031102, [[1104.3702](#)].
- [2] D. Garfinkle and L. A. Pando Zayas, *Rapid Thermalization in Field Theory from Gravitational Collapse*, *Phys. Rev.* **D84** (2011) 066006, [[1106.2339](#)].
- [3] J. Jalmuzna, A. Rostworowski and P. Bizon, *A Comment on AdS collapse of a scalar field in higher dimensions*, *Phys. Rev.* **D84** (2011) 085021, [[1108.4539](#)].
- [4] D. Garfinkle, L. A. Pando Zayas and D. Reichmann, *On Field Theory Thermalization from Gravitational Collapse*, *JHEP* **02** (2012) 119, [[1110.5823](#)].
- [5] O. J. C. Dias, G. T. Horowitz and J. E. Santos, *Gravitational Turbulent Instability of Anti-de Sitter Space*, *Class. Quant. Grav.* **29** (2012) 194002, [[1109.1825](#)].
- [6] V. Balasubramanian, A. Buchel, S. R. Green, L. Lehner and S. L. Liebling, *Holographic Thermalization, Stability of Anti-de Sitter Space, and the Fermi-Pasta-Ulam Paradox*, *Phys. Rev. Lett.* **113** (2014) 071601, [[1403.6471](#)].
- [7] B. Craps, O. Evnin and J. Vanhoof, *Renormalization group, secular term resummation and AdS (in)stability*, *JHEP* **10** (2014) 048, [[1407.6273](#)].
- [8] P. Basu, C. Krishnan and A. Saurabh, *A stochasticity threshold in holography and the instability of AdS*, *Int. J. Mod. Phys.* **A30** (2015) 1550128, [[1408.0624](#)].
- [9] F. V. Dimitrakopoulos, B. Freivogel, M. Lippert and I.-S. Yang, *Position space analysis of the AdS (in)stability problem*, *JHEP* **08** (2015) 077, [[1410.1880](#)].
- [10] A. Buchel, S. R. Green, L. Lehner and S. L. Liebling, *Conserved quantities and dual turbulent cascades in anti-de Sitter spacetime*, *Phys. Rev.* **D91** (2015) 064026, [[1412.4761](#)].
- [11] B. Craps, O. Evnin and J. Vanhoof, *Renormalization, averaging, conservation laws and AdS (in)stability*, *JHEP* **01** (2015) 108, [[1412.3249](#)].
- [12] O. Evnin and C. Krishnan, *A Hidden Symmetry of AdS Resonances*, *Phys. Rev.* **D91** (2015) 126010, [[1502.03749](#)].
- [13] F. Dimitrakopoulos and I.-S. Yang, *Conditionally extended validity of perturbation theory: Persistence of AdS stability islands*, *Phys. Rev.* **D92** (2015) 083013, [[1507.02684](#)].
- [14] S. R. Green, A. Maillard, L. Lehner and S. L. Liebling, *Islands of stability and recurrence times in AdS*, *Phys. Rev.* **D92** (2015) 084001, [[1507.08261](#)].

- [15] B. Craps, O. Evnin and J. Vanhoof, *Ultraviolet asymptotics and singular dynamics of AdS perturbations*, *JHEP* **10** (2015) 079, [[1508.04943](#)].
- [16] B. Craps, O. Evnin, P. Jai-akson and J. Vanhoof, *Ultraviolet asymptotics for quasiperiodic AdS₄ perturbations*, *JHEP* **10** (2015) 080, [[1508.05474](#)].
- [17] B. Craps and O. Evnin, *AdS (in)stability: an analytic approach*, *Fortsch. Phys.* **64** (2016) 336–344, [[1510.07836](#)].
- [18] A. Buchel, S. L. Liebling and L. Lehner, *Boson stars in AdS spacetime*, *Phys. Rev.* **D87** (2013) 123006, [[1304.4166](#)].
- [19] M. Maliborski and A. Rostworowski, *A comment on "Boson stars in AdS"*, [1307.2875](#).
- [20] M. Maliborski and A. Rostworowski, *Lecture Notes on Turbulent Instability of Anti-de Sitter Spacetime*, *Int. J. Mod. Phys.* **A28** (2013) 1340020, [[1308.1235](#)].
- [21] P. Bizoń and A. Rostworowski, *Comment on "Holographic Thermalization, Stability of Anti-de Sitter Space, and the Fermi-Pasta-Ulam Paradox"*, *Phys. Rev. Lett.* **115** (2015) 049101, [[1410.2631](#)].
- [22] V. Balasubramanian, A. Buchel, S. R. Green, L. Lehner and S. L. Liebling, *Reply to Comment on "Holographic Thermalization, Stability of Anti-de Sitter Space, and the Fermi-Pasta-Ulam Paradox"*, *Phys. Rev. Lett.* **115** (2015) 049102, [[1506.07907](#)].
- [23] P. Bizoń, M. Maliborski and A. Rostworowski, *Resonant Dynamics and the Instability of Anti-de Sitter Spacetime*, *Phys. Rev. Lett.* **115** (2015) 081103, [[1506.03519](#)].
- [24] N. Deppe, *On the stability of anti-de Sitter spacetime*, [1606.02712](#).
- [25] F. V. Dimitrakopoulos, B. Freivogel, J. F. Pedraza and I.-S. Yang, *Gauge dependence of the AdS instability problem*, *Phys. Rev.* **D94** (2016) 124008, [[1607.08094](#)].
- [26] F. V. Dimitrakopoulos, B. Freivogel and J. F. Pedraza, *Fast and Slow Coherent Cascades in Anti-de Sitter Spacetime*, *Class. Quant. Grav.* **35** (2018) 125008, [[1612.04758](#)].
- [27] S. L. Liebling and G. Khanna, *Scalar collapse in AdS with an OpenCL open source code*, *Class. Quant. Grav.* **34** (2017) 205012, [[1706.07413](#)].
- [28] P. Bizoń and J. Jałmużna, *Globally regular instability of AdS₃*, *Phys. Rev. Lett.* **111** (2013) 041102, [[1306.0317](#)].
- [29] E. da Silva, E. Lopez, J. Mas and A. Serantes, *Collapse and Revival in Holographic Quenches*, *JHEP* **04** (2015) 038, [[1412.6002](#)].
- [30] N. Deppe, A. Kolly, A. R. Frey and G. Kunstatter, *Black Hole Formation in AdS Einstein-Gauss-Bonnet Gravity*, *JHEP* **10** (2016) 087, [[1608.05402](#)].
- [31] N. Deppe, A. Kolly, A. Frey and G. Kunstatter, *Stability of AdS in Einstein Gauss Bonnet Gravity*, *Phys. Rev. Lett.* **114** (2015) 071102, [[1410.1869](#)].
- [32] R. Arias, J. Mas and A. Serantes, *Stability of charged global AdS₄ spacetimes*, *JHEP* **09** (2016) 024, [[1606.00830](#)].

- [33] H. Okawa, J. C. Lopes and V. Cardoso, *Collapse of massive fields in anti-de Sitter spacetime*, [\[1504.05203\]](#).
- [34] N. Deppe and A. R. Frey, *Classes of Stable Initial Data for Massless and Massive Scalars in Anti-de Sitter Spacetime*, *JHEP* **12** (2015) 004, [\[1508.02709\]](#).
- [35] V. E. Hubeny and M. Rangamani, *Unstable horizons*, *JHEP* **05** (2002) 027, [\[hep-th/0202189\]](#).
- [36] A. Buchel and L. Lehner, *Small black holes in $AdS_5 \times S^5$* , *Class. Quant. Grav.* **32** (2015) 145003, [\[1502.01574\]](#).
- [37] A. Buchel, *Universality of small black hole instability in AdS/CFT* , *Int. J. Mod. Phys.* **D26** (2017) 1750140, [\[1509.07780\]](#).
- [38] A. Buchel and M. Buchel, *On stability of nonthermal states in strongly coupled gauge theories*, [\[1509.00774\]](#).
- [39] R. Brito, V. Cardoso and J. V. Rocha, *Interacting shells in AdS spacetime and chaos*, *Phys. Rev.* **D94** (2016) 024003, [\[1602.03535\]](#).
- [40] H. P. de Oliveira, L. A. Pando Zayas and C. A. Terrero-Escalante, *Turbulence and Chaos in Anti-de-Sitter Gravity*, *Int. J. Mod. Phys.* **D21** (2012) 1242013, [\[1205.3232\]](#).
- [41] O. Aharony, S. S. Gubser, J. M. Maldacena, H. Ooguri and Y. Oz, *Large N field theories, string theory and gravity*, *Phys. Rept.* **323** (2000) 183–386, [\[hep-th/9905111\]](#).
- [42] H. Nastase, *Introduction to the AdS/CFT Correspondence*. Cambridge University Press, 2015.
- [43] P. R. Brady, C. M. Chambers and S. M. C. V. Goncalves, *Phases of massive scalar field collapse*, *Phys. Rev.* **D56** (1997) 6057–6061, [\[gr-qc/9709014\]](#).
- [44] D. Santos-Oliván and C. F. Sopuerta, *Moving closer to the collapse of a massless scalar field in spherically symmetric anti-de Sitter spacetimes*, *Phys. Rev.* **D93** (2016) 104002, [\[1603.03613\]](#).
- [45] G. Martinon, *The instability of anti-de Sitter space-time*, [\[1708.05600\]](#).
- [46] A. Buchel, L. Lehner and S. L. Liebling, *Scalar Collapse in AdS* , *Phys. Rev.* **D86** (2012) 123011, [\[1210.0890\]](#).
- [47] J. Jałmużna, C. Gundlach and T. Chmaj, *Scalar field critical collapse in 2+1 dimensions*, *Phys. Rev.* **D92** (2015) 124044, [\[1510.02592\]](#).
- [48] P. Bizoń, *Is AdS stable?*, *Gen. Rel. Grav.* **46** (2014) 1724, [\[1312.5544\]](#).
- [49] M. Maliborski and A. Rostworowski, *Time-Periodic Solutions in an Einstein AdS -Massless-Scalar-Field System*, *Phys. Rev. Lett.* **111** (2013) 051102, [\[1303.3186\]](#).
- [50] M. Maliborski and A. Rostworowski, *What drives AdS spacetime unstable?*, *Phys. Rev.* **D89** (2014) 124006, [\[1403.5434\]](#).
- [51] G. Fodor, P. Forgàcs and P. Grandclément, *Self-gravitating scalar breathers with negative cosmological constant*, *Phys. Rev.* **D92** (2015) 025036, [\[1503.07746\]](#).

- [52] O. J. C. Dias, G. T. Horowitz, D. Marolf and J. E. Santos, *On the Nonlinear Stability of Asymptotically Anti-de Sitter Solutions*, *Class. Quant. Grav.* **29** (2012) 235019, [[1208.5772](#)].
- [53] B. Cownden, N. Deppe and A. R. Frey, *Phase Diagram of Stability for Massive Scalars in Anti-de Sitter Spacetime*, [1711.00454](#).
- [54] R. Brito, V. Cardoso and J. V. Rocha, *Interacting shells in AdS spacetime and chaos*, *Phys. Rev.* **D94** (2016) 024003, [[1602.03535](#)].
- [55] O. Dias and J. E. Santos, *AdS nonlinear instability: moving beyond spherical symmetry*, *Class. Quant. Grav.* **33** (2016) 23LT01, [[1602.03890](#)].
- [56] O. J. C. Dias and J. E. Santos, *AdS nonlinear instability: breaking spherical and axial symmetries*, [1705.03065](#).
- [57] M. W. Choptuik, O. J. C. Dias, J. E. Santos and B. Way, *Collapse and Nonlinear Instability of AdS Space with Angular Momentum*, *Phys. Rev. Lett.* **119** (2017) 191104, [[1706.06101](#)].
- [58] V. E. Hubeny, *The AdS/CFT Correspondence*, *Class. Quant. Grav.* **32** (2015) 124010, [[1501.00007](#)].
- [59] L.-Y. Chen, N. Goldenfeld and Y. Oono, *The Renormalization group and singular perturbations: Multiple scales, boundary layers and reductive perturbation theory*, *Phys. Rev.* **E54** (1996) 376–394, [[hep-th/9506161](#)].
- [60] Y. Nakayama, *Holographic interpretation of renormalization group approach to singular perturbations in nonlinear differential equations*, *Phys. Rev.* **D88** (2013) 105006, [[1305.4117](#)].
- [61] M. Choptuik, J. E. Santos and B. Way, *Charting Islands of Stability with Multioscillators in anti-de Sitter space*, *Phys. Rev. Lett.* **121** (2018) 021103, [[1803.02830](#)].
- [62] S. L. Liebling and G. Khanna, *Scalar collapse in AdS with an OpenCL open source code*, *Class. Quant. Grav.* **34** (2017) 205012, [[1706.07413](#)].
- [63] F. V. Dimitrakopoulos, B. Freivogel and J. F. Pedraza, *Fast and Slow Coherent Cascades in Anti-de Sitter Spacetime*, [1612.04758](#).
- [64] O. Evnin and P. Jai-akson, *Detailed ultraviolet asymptotics for AdS scalar field perturbations*, *JHEP* **04** (2016) 054, [[1602.05859](#)].
- [65] A. Buchel, R. C. Myers and A. van Niekerk, *Nonlocal probes of thermalization in holographic quenches with spectral methods*, *JHEP* **02** (2015) 017, [[1410.6201](#)].
- [66] A. Biasi, P. Carracedo, J. Mas, D. Musso and A. Serantes, *Floquet Scalar Dynamics in Global AdS*, *JHEP* **04** (2018) 137, [[1712.07637](#)].
- [67] P. Carracedo, J. Mas, D. Musso and A. Serantes, *Adiabatic pumping solutions in global AdS*, *JHEP* **05** (2017) 141, [[1612.07701](#)].
- [68] M. Rangamani, M. Rozali and A. Wong, *Driven Holographic CFTs*, *JHEP* **04** (2015) 093, [[1502.05726](#)].
- [69] R. C. Myers, M. Rozali and B. Way, *Holographic Quenches in a Confined Phase*, *J. Phys.* **A50** (2017) 494002, [[1706.02438](#)].

- [70] P. Breitenlohner and D. Z. Freedman, *Positive Energy in Anti-de Sitter Backgrounds and Gauged Extended Supergravity*, *Phys. Lett.* **B115** (1982) 197–201.
- [71] H. Năstase, *Introduction to the ADS/CFT Correspondence*. Cambridge University Press, 2015.
- [72] A. Biasi, B. Craps and O. Evnin, *Energy returns in global AdS_4* , [1810.04753](https://arxiv.org/abs/1810.04753).
- [73] B. Cownden, N. Deppe and A. R. Frey, In preparation, (2020) .